Multi-Structural and Multi-Path Variational Transtition Sate Thoery. Application to Kinetics Studies of Hydrogen Transfer Reaction in Gas Phase

A DISSERTATION
SUBMITTED TO THE FACULTY OF THE GRADUATE SCHOOL
OF THE UNIVERSITY OF MINNESOTA
BY

Tao Yu

IN PARTIAL FULFILLMENT OF THE REQUIREMENTS
FOR THE DEGREE OF
DOCTOR OF PHILOSOPHY

Adviser: Donald G Truhlar

June 2012

Acknowledgements

I sincerely appreciate all the help and support from my advisor professor Donald G. Truhlar and my colleagues Dr. Jingjing Zheng, Dr. Osanna Tishchenko, and all the other group members in Truhlar's group. I also appreciate all the computing time provided from Minnesota Supercomputing institute (MSI), and Pacific Northwest National Lab (PNNL).

Dedication

This dissertation is dedicated to my parents.

Abstract

To use computational methods to study the kinetics of combustion reaction of either alkanes or biofuels, two great challenge issues need to be addressed. The first one is the multi-structure effect, which makes the reactive potential energy surface complex, and requires considering multiple stationary states and multiple reaction paths to calculate the thermal rate. The second issue oringinates from torsional anharmonicity, which causes the harmonic oscillator approximation and normal mode analysis to fail and requires treating the torsions using different models in different temperature regimes. To treat the multi-structural and torsional anharmonicity correctly, we developed the internal-coordinate multi-structural approximation to calculate the partition functions for large molecules. This new method can predict more accurate partition functions for complex molecules in both the low and high temperature ranges. We also developed two new formulations of variational transtition state theory (VTST): multi-structure and multi-path VTST with multi-dimensional tunneling to calculate the thermal rates of hydrogen-transfer reactions in a broad temperature range. These formulations include both multi-structure and torsional anharmonicity effects and a more accurate means to evaluate vairational and tunneling effects using multiple reaction paths in the calculation. The thesis work is presented as four chapters, as follows:

Chapter one discusses the theory of the internal-coordinate multi-structural approximation, also called the multi-structure torsional (MS-T) approximation and its application to various molecules. Although this work was mainly contributed by J.

Zheng and S. Mielke in our group, the author still would like to present this part in the thesis because this part is one of the fundamentals for the following chapters.

Chapter two investigates the thermodynamics properties of two complex molecules, *n*-hepane and isoheptane, using the MS-T method. The results were compared with experimental data from the API Tables and TRC data sets and with the empirical group additivity method, to further demonstrate the success of the MS-T approximation in calculating the partition functions of large molecules.

Chapter three focuses on presenting multi-structure variational transion state theory (MS-VTST) with torsional anhormicity, which includes both multi-structure and torsional anharmonicity effects for reactants, products, and transition states, but uses only the reaction path with the lowest vibrationally adiabatic ground-state potential energy barrier to calculate the variational and tunneling effects. To apply this theory, we studied the thermal rate of the 1,4-hydrogen shift reaction of 1-pentyl radical, and by comparing with experimental data, demonstrated that the MS-VTST rate is more accurate than that obtained by conventional single-structure VTST (SS-VTST).

The last chapter, chapter four, extends the MS-VTST method to multi-path VTST (MP-VTST), which includes not only the multi-structure effect, but also the contribution of the variational and tunneling effects of all reaction paths. We applied this formulation to calculate the thermal rate of 1,4-hydrogen shift isomerization of the 2-cyclohexylethyl radical using two reaction paths.

Table of Contents

List of Tables

List of Figures

Chapter 1.* Practical methods for including torsional anharmonicity in thermochemical calculations on complex molecules: The internal-coordinate multi-structural approximation

* This work is done by the team: J. Zheng, T. Yu, E. Papajak, I. M. Alecu, S. L. Mielke and D. G. Truhlar. Most of the work is contributed by J. Zheng and S. L. Meilke.

1. Introduction

Torsional motion constitutes an especially challenging form of vibrational anharmonicity for which the harmonic approximation is often highly inaccurate. Furthermore, the presence of multiple torsional degrees of freedom often results in many low-energy conformers that contribute significantly to the partition function. Feynman path integral methods[1, 2] provide an accurate and straightforward way to include torsional effects in quantum mechanical partition functions, and while they have already provided important benchmark results for small systems,[3-5] more affordable methods are needed for many applications involving complex molecules.

A variety of separable approximations are available[6-20] that replace the harmonic contribution of specific normal modes by solutions of one-dimensional (1-D) torsional treatments, and nonseparable treatments have also been advanced.[9, 14, 16, 21-25] In many instances torsions are strongly mixed with other torsions and/or with other low-frequency motions such as bending, and in such cases one cannot identify them with specific normal modes. We divide the nonseparable treatments into two classes, those that do not assume a one-to-one correspondence between torsions and individual normal modes, and those that do; we call these mixed torsion models and normal mode

substitution models. The only widely discussed model that allows mixed torsions is the Pitzer–Gwinn approximation.[21] This requires evaluating the full-dimensional classical configuration integral,[26] which—although less expensive than a path integral—is still too expensive for routine use on large molecules because it requires either extensive Monte Carlo sampling by direct dynamics (electronic structure calculations on the fly) or the careful fitting of an analytic nonseparable potential function. Reduced-dimensional path integrals[23, 27-29] and classical configuration integrals covering only torsional degrees of freedom[9, 16] have also been considered but are more expensive than the methods to be proposed here. On the other hand, methods employing normal mode substitution[7-10, 12-14, 22] are not general enough for our purpose.

In this article we will consider a family of new torsional approximations that employ internal coordinate correction factors to the harmonic treatment that avoid not only the separability assumption but also the restriction associated with assigning torsions to specific normal modes.

In many cases, the thermochemical properties of a chemical substance can be reasonably estimated by using the group additivity method with the assumption that the thermodynamic properties of a given species can be obtained by summing the contributions from each group comprising that species. The most widely employed version of group additivity was formulated by Benson,[30] and established general group additivity values through a two-step process involving first compartmentalizing similar molecules with known thermodynamic properties into their constituent groups where a group is defined as a polyvalent atom and all of its ligands and then deriving the contribution to various thermodynamic properties due to each group through

multivariable linear regression fits to the available experimental data.[30] The original group additivity values established by Benson for stable molecules were later adapted to several classes of free radical species by O'Neal and Benson,[31, 32] and were subsequently updated by Cohen[33] to account for new experimental and theoretical findings. More recently, Lay et al.[34] developed an alternative technique for estimating bulk thermodynamic properties, often with improved accuracy, from a single group called the H atom bond increment (HBI) group. We used these various group additivity techniques to estimate the entropies of the species studied in this work and compare them to our methods.

2. Theory

2.1. Overview

The most direct consequence of internal rotation is the occurrence of multiple conformational minima. A conventional approach[35, 36] to calculating partition functions in such cases is to use the harmonic approximation for the minimum-energy structure and to replace contributions from certain normal modes with a hindered rotor treatment by using the tables of Pitzer and Gwinn[21] or an analytic hindered rotor[7, 10], or free rotor approximation. A somewhat more complicated case occurs when a torsion is unsymmetrical (or isotopically substituted) so that the minima encountered along the torsion are distinguishable. Then, if one assumes that the vibrational modes are separable, the partition function for each of the unsymmetrical torsional motions has contributions from each distinguishable conformer. However the treatment of torsions as separable can be very unrealistic.[12, 37-41] A better approach is to start with a list of

distinguishable structures (i.e., distinguishable conformers) and to sum their contributions, including at least torsional anharmonicity. We call such methods multi-structural (MS) approximations, and these are the subjects of the present paper.

2.2. MS-AS method with nearly separable torsions

2.2. 1. Theory. Let *Q* denote a multidimensional partition function and *q* denote the partition function for a single degree of freedom. In the convention used in this article, all partition functions have their zero of energy at their local minimum (rather than being normalized to unity at 0 K). We will consider *J* distinguishable structures, i.e., conformational minima, $j = 1, 2, \ldots, J$, and we will include anharmonicity in several torsions labeled $\tau = 1, 2, \ldots, t$; we note that *t* has the same value for all structures. Let the energies of the minima be U_j where U_1 has a value of zero, and all other U_j are positive. We divide the *t* torsions into two types: nearly separable (NS) and strong coupled (SC). For NS torsions, we may define a parameter $M_{j,\tau}$ to be the total number of minima, whether distinguishable or not, along torsional coordinate τ of structure *j* (each of these minima correspond to another structure).

In our initial presentation we shall restrict attention to the special case that all the torsions are nearly separable and we will further assume that the $M_{j,\tau}$ minima may be reasonably approximated as being evenly distributed along the torsional coordinate τ. In Section II.B.2 we will present an alternative derivation of the MS-AS approximation based on a different rationale for assigning the $M_{j,\tau}$ parameters and that may be useful in more general contexts, including some cases of strong coupling between the torsions.

The alternative derivation explicitly accounts for cases where the minima are not approximately evenly distributed along a given torsional coordinate. In section II.C we will present a variation of the multi-structural method that utilizes explicit barrier information instead of the $M_{j,\tau}$ parameters, and in section II.D we will consider a variation of the method designed to treat the most challenging cases of strong coupling wherein parameters are obtained by Voronoi tessellation.[42-44] In general we can use a hybrid scheme for obtaining $M_{j,\tau}$; for example, we use the notation NS:SC = *n*:*m* to denote that *n* torsions are treated as nearly separable and *m* torsions are treated as strong coupled. In this language, the present section (II.B.1) is devoted to the case *t*:0.

We will denote the torsional symmetry numbers as σ_τ and the number of distinguishable minima for torsional coordinate τ of structure *j* as $P_{j,\tau}$ where

$$P_{j,\tau} = M_{j,\tau} / \sigma_\tau . \qquad (1)$$

The symmetry numbers σ_τ can be determined by treating the least symmetric of the two rotating fragments as a fixed frame and counting the number of identical structures obtained when the more symmetrical top is rotated from 0 to 360 degrees and relaxed (for example, the symmetry numbers for methanol, nitromethane, and 1,2 dichloroethane are 3, 3, and 1, respectively). Once all the structures are found, the number, $P_{j,\tau}$, of unique structures connected to structure *j* (including itself) by internal rotation τ may often be identified by counting the structures that have similar torsion angles for all other internal rotations; when strong torsional coupling exists additional considerations may be necessary as will be discussed further below. Attempts have been

made[12, 45] to fully automate the assignment of the $P_{j,\tau}$ (or equivalently the $M_{j,\tau}$), but such approaches are beyond the scope of the present study.

In general, the internal moment of inertia, $I_{j,\tau}$, associated with rotation about a specific axis τ is a continuous function of geometry, but we will approximate it as a constant within the domain of each specific structure and will assign values $I_{j,\tau}$ that are calculated for rotation about the bond axis associated with torsion τ at the minimum-energy geometry of structure *j* using the method of Pitzer.[46] (In previous articles,[13, 14] we denoted Pitzer's method for calculating the internal moment of inertia for an internal rotation as the curvilinear method, abbreviated C.) Pitzer[46] has pointed out that the geometry dependence of the moments of inertia approximately compensates for the change in the product of the vibrational frequencies as a function of the internal rotation angle. This justifies holding the internal moments of inertia fixed at their values at the minimum-energy geometry when the vibrational motions are approximated by a classical harmonic treatment; however, we include quantum effects, and we use this approximation even when the classical harmonic approximation is not valid.

Pitzer's method[46] for calculating internal moments of inertia assumes that all molecular fragments that undergo internal rotation are attached to a unique fixed frame; for cases with more than one torsion the scheme is approximate unless a determinant-based approach is used to fully account for intermode coupling. A more-general treatment is available in the work of Kilpatrick and Pitzer[47] that accounts for the coupling between torsional motions and removes the requirement of a unique fixed frame. In the following, when we refer to Pitzer moments we are referring to moments

calculated in the absence of intermode coupling; approaches that include intermode coupling have only rarely been employed in earlier work, but here, in addition to the uncoupled Pitzer moments, we also employ the general treatment of Kilpatrick and Pitzer.[47] The Kilpatrick and Pitzer[47] treatment leads to the calculation of a kinetic energy matrix for internal rotation denoted as **D** (alternatively one may work with the kinetic energy matrix **S** associated with overall rotation and internal rotation) which may be diagonalized to yield moments associated with linear combinations of coupled torsions. The moments of Pitzer[46] are the diagonal elements of the **D** matrix and in the limit of weak torsional coupling (where **D** is strongly diagonally dominant) torsional motion is well represented by rotation about a single bond. Our torsional approximation scheme begins by approximating torsional motions as being uncoupled within the domain of a specific structure so we begin by employing the approximate Pitzer moments. However, in the high-temperature limit the partition function scales as the square root of the determinant of **D**, and we gradually switch to the Kilpatrick–Pitzer coupled moments as the temperature is increased.

The torsional coordinate associated with the Pitzer internal moments of inertia describes the rotation of a rigid top against a fixed frame, and various considerations have been used to define physical torsion coordinates for flexible systems.[48-50] In our internal-coordinate treatment, we approximate the torsional coordinate by a single dihedral angle. Thus, our torsional force constants and other results have a small dependence on the choice of coordinate system, i.e., on which dihedral angle we choose. One consequence of using internal coordinate torsion angles is that subtle deviations from expected symmetries may be observed; for example, methyl groups

may deviate very slightly from the expected three-fold symmetry. In such cases we use values of $M_{j,\tau}$, $P_{j,\tau}$, and σ_τ that would have been obtained from the more symmetrical structures. All of the methods presented here assume that the domains of different conformers do not significantly overlap; in cases where slight symmetry lowering leads to strongly overlapping structures it may be best to include only one of the strongly overlapping structures and treat this conformer using a symmetry number that would have been appropriate in the absence of symmetry lowering.

If there is only one conformer and we neglect coupling between electronic, vibrational, and rotational degrees of freedom, the total partition function of a system can be written as

$$Q_{\text{total}} = Q_{\text{trans}} Q_{\text{elec}} Q_{\text{rot}} \prod_{m=1}^{F} q_{\text{vib},m} \tag{2a}$$

where Q_{trans} is the translational partition function, Q_{elec} is the electronic partition function, Q_{rot} is the rotational partition function, $F = 3N - 6$ for a nonlinear molecule (where N is number of atoms in the system), and $q_{\text{vib},m}$ is the vibrational partition function of mode m. However, we do not use that simplification; instead, we write

$$Q_{\text{total}} = Q_{\text{trans}} Q_{\text{elec}} Q_{\text{con-rovib}} \tag{2b}$$

where $Q_{\text{con-rovib}}$ is the conformational-rovibrational partition function. In this article, the translational and electronic partition functions are not discussed. We mainly focus on the vibrational partition function, but eqn (2b) also allows for a conformational average and for the change of rotational partition function from structure to structure. Thus, we do not assume that rotation is separable in an overall sense because the rotational partition function depends on the structure.

Special consideration is needed with considering symmetry numbers for systems with internal rotations. The overall torsional symmetry number associated with the torsion-only degrees of freedom is

$$\sigma_{\text{torsion}} = \prod_{\tau=1}^{t} \sigma_{\tau} \tag{3}$$

and is the same for all structures. However, the structures can include cases both with and without rotational symmetry so that rotational symmetry number $\sigma_{\text{rot},j}$ depends on *j*. It should be realized that the rotational symmetry elements that transform symmetrical structures into themselves transform unsymmetrical structures into *other* unsymmetrical structures that appear in the list of the *J* structures that are distinguishable when only considering torsional symmetry, and therefore $\sigma_{\text{rot},j}$ depends on how these structures are treated. We can make this clear by an example. Consider pentane,[51] which has 11 torsional conformers if we do not consider the two methyl groups; eight of these structures have no rotational symmetry and thus have $\sigma_{\text{rot},j}$ equal to 1, whereas three of them have $\sigma_{\text{rot},j}$=2. Of the eight structures with $\sigma_{\text{rot},j}$ = 1, only four are distinguishable when rotation is considered because each structure may be transformed into one other structure by an overall rotation. Thus, if all eleven structures are included in the MS-AS partition function calculations each of the rotational partition functions should use a symmetry number of 2. Alternatively, one could include only the seven structures that are distinguishable after considering both rotational and torsional symmetries, in which case the rotational partition functions would use the structure-dependent $\sigma_{\text{rot},j}$ values.

We propose a new family of approximations to be called multi-structural methods. The first member of the family is the MS-AS method in which we include all structures. The conformational-rovibrational partition function is given in the MS-AS method by

$$Q_{\text{con-rovib}}^{\text{MS-AS}} = \sum_{j=1}^{J} Q_{\text{rot},j} \exp\left(-\beta U_j\right) Q_j^{\text{HO}} Z_j \prod_{\tau=1}^{t} f_{j,\tau} \qquad (4)$$

where $Q_{\text{rot},j}$ is the rotational partition function of structure *j* (here we use the classical approximation for rotational partition functions, see eqn (B4)), β is $1/k_B T$ where k_B is Boltzmann's constant and *T* is temperature, Q_j^{HO} is the usual normal-mode harmonic oscillator vibrational partition function calculated at structure *j*, Z_j is a factor (specified below) designed to ensure that the MS-AS scheme reaches the correct high-*T* limit (within the parameters of the model), and $f_{j,\tau}$ is an internal-coordinate torsional anharmonicity function that, in conjunction with Z_j, adjusts the harmonic result of structure *j* for the presence of the torsional motion associated with coordinate τ.

We use MS-HO to denote the partition function calculated without Z_j and $f_{j,\tau}$, that is, with all Z_j and all $f_{j,\tau}$ equal to unity. One can use normal-mode analysis to obtain frequencies to calculate Q_j^{HO}. A key advantage of eqn (4) over the MS-HO approximation is that it includes torsional anharmonicity, but it is not necessary to assign each torsional motion to a specific normal mode. The MS-HO approximation is already an improvement over treatments that include only the lowest-energy conformation, and the importance of including a conformational average when computing enthalpies has recently been emphasized.[36, 52]

We define the torsional correction functions $f_{j,\tau}$ as the ratio of a partition function for some accurate method to treat a given torsion divided by a harmonic partition function for a frequency $\overline{\omega}_{j,\tau}$, where the frequency $\overline{\omega}_{j,\tau}$ is defined as the harmonic frequency obtained using internal coordinates rather than a normal-coordinate frequency. This scheme avoids identifying each torsional mode with a specific normal mode. The internal-coordinate torsional frequency is obtained by

$$\overline{\omega}_{j,\tau} = \sqrt{\frac{k_{j,\tau}}{I_{j,\tau}}} \tag{5}$$

$$k_{j,\tau} \equiv \left.\frac{\partial^2 V}{\partial \phi_\tau^2}\right|_{\phi_\tau = \phi_{\tau,\mathrm{eq.j}}} \tag{6}$$

where $k_{j,\tau}$ is the force constant of a specific torsion τ at structure *j*, *V* is the potential energy, and the torsion τ is represented by a dihedral angle ϕ_τ whose equilibrium value is $\phi_{\tau,\mathrm{eq.}j}$.

The internal-coordinate force constants can be calculated either by numerical finite differences or by transforming force constant matrices expressed in Cartesian coordinates into force constant matrices in non-redundant internal coordinates.[53-58] In the numerical finite difference method, one rotates one of the two tops with respect to the other by a small amount and uses central differences to calculate the second derivative from the equilibrium energy and single-point energies of the two slightly distorted geometries. In the transformation method, one has to be careful to select an appropriate set of $3N - 6$ independent internal coordinates. The strategy we employ to select the $3N - 6$ independent internal coordinates is that (i) all bond stretching coordinates are included, (ii) only one dihedral angle is selected for each torsional

mode, and (iii) the rest of the coordinates are bond angles and other dihedral angles not related to torsions (e.g., dihedral angles for out-of-plane motion in a ring structure) that are selected while avoiding redundant choices. By using such a set of $3N - 6$ independent internal coordinates, the second partial derivative of V with respect to the dihedral angle is the force constant for this torsion. In this paper, all the torsional force constants are calculated by the transformation method.

The reference Pitzer–Gwinn (RPG) method[14, 21] denotes the use of a one-dimensional Pitzer–Gwinn approximation applied to a reference potential (rather than the true potential as in the Pitzer–Gwinn method) where the reference potential is obtained from limited information. The reference potential was previously taken as[7, 14, 21, 46]

$$V_m = \frac{W_m}{2}\left[1 - \cos(M_m \phi_m)\right] \tag{7}$$

where V_m is the potential of normal mode m, ϕ_m is a torsion coordinate, M_m is the number of minima in mode m, and W_m is a torsional barrier height. If all the torsional barriers do not have the same height, W_m would be an effective or average height. Here we instead use

$$V_{j,\tau} = U_j + \frac{W_{j,\tau}}{2}\left[1 - \cos M_{j,\tau}(\phi_\tau - \phi_{\tau,\mathrm{eq}.j})\right]; \quad \frac{-\pi}{M_{j,\tau}} \le \phi_\tau - \phi_{\tau,\mathrm{eq}.j} \le \frac{\pi}{M_{j,\tau}} \tag{8}$$

where $W_{j,\tau}$ is an effective barrier height associated with structure j. When the RPG method is applied to eqn (8), $f_{j,\tau}$ can be written as

$$f_{j,\tau} = \sigma_\tau \left\lfloor \frac{q_{j,\tau}^{\mathrm{RC}}}{q_{j,\tau}^{\mathrm{CHO}}} \right\rfloor \tag{9}$$

where $q_{j,\tau}^{\mathrm{CHO}}$ and $q_{j,\tau}^{\mathrm{RC}}$ are the classical harmonic oscillator and reference classical partition functions of the torsion τ for structure *j*, respectively, given by

$$q_{j,\tau}^{\mathrm{CHO}} = \frac{1}{\mathrm{h}\beta\overline{\omega}_{j,\tau}} \tag{10}$$

and[14]

$$q_{j,\tau}^{\mathrm{RC}} = \frac{1}{M_{j,\tau}} q_{j,\tau}^{\mathrm{FR}} \exp(-\beta W_{j,\tau}/2) I_0(\beta W_{j,\tau}/2) \tag{11}$$

where h is Planck's constant divided by 2π, I_0 is a modified Bessel function, and the free rotor (FR) partition function is given by

$$q_{j,\tau}^{\mathrm{FR}} = \frac{\sqrt{2\pi I_{j,\tau}/\beta}}{\mathrm{h}\sigma_\tau} \tag{12}$$

Equation (7) assumes that all barriers along a torsional coordinate have the same height W_m or at least may be represented by a single average barrier, and that all of the minima have the same energy, whereas eqn (8) provides the flexibility for each structure to have an independent minimum and barrier height. The $W_{j,\tau}$ can be chosen as the average of the barrier heights on either side of this minimum. However, we next make a simplification so that we do not need to know these barriers. The simplification takes advantage of the fact that for a potential of the form of eqn (8) and a geometry-independent internal moment of inertia, the barrier heights, internal moment of inertia, and the torsional frequency are interrelated by[7, 14]

$$W_{j,\tau} = \frac{2I_{j,\tau}\overline{\omega}_{j,\tau}^2}{M_{j,\tau}^2} \tag{13}$$

Using this relation, eqns (11) and (9) are rewritten as

$$q_{j,\tau}^{\mathrm{RC}} = \frac{1}{M_{j,\tau}} q_{j,\tau}^{\mathrm{FR}} \exp(-\beta I_{j,\tau} \overline{\omega}_{j,\tau}^2 / M_{j,\tau}^2) I_0(\beta I_{j,\tau} \overline{\omega}_{j,\tau}^2 / M_{j,\tau}^2) \tag{14}$$

and

$$f_{j,\tau} = \frac{\overline{\omega}_{j,\tau} \sqrt{2\pi\beta I_{j,\tau}}}{M_{j,\tau}} \exp(-\beta I_{j,\tau} \overline{\omega}_{j,\tau}^2 / M_{j,\tau}^2) I_0(\beta I_{j,\tau} \overline{\omega}_{j,\tau}^2 / M_{j,\tau}^2) \tag{15a}$$

Notice that eqn (15a) can be rearranged to

$$f_{j,\tau} = \frac{\sqrt{2\pi\beta k_{j,\tau}}}{M_{j,\tau}} \exp(-\beta k_{j,\tau} / M_{j,\tau}^2) I_0(\beta k_{j,\tau} / M_{j,\tau}^2) \tag{15b}$$

which shows that $f_{j,\tau}$ is independent of $I_{j,\tau}$. This situation results because both the numerator and denominator of eqn (9) have the same functional dependence on $I_{j,\tau}$. The inclusion of the Z_j factor (discussed next) restores the expected dependence of the partition function on the moments of inertia as the high-*T* limit is approached. Note also that the modified Bessel function $I_0(x)$ approaches $\frac{\exp(x)}{\sqrt{2\pi x}}$ as *x* approaches infinity; therefore, when the temperature approaches zero, i.e., β approaches infinity, all the $f_{j,\tau}$ become 1, and the MS-AS partition function reduces to the MS-HO partition function. Consequently, the MS-AS and MS-HO methods yield the same zero-point energy (ZPE).

Next we consider two corrections, both introduced via the factor Z_j, which ensure that we reach a correct high-temperature limit. One is to replace the normal-mode partition function in the high-*T* limit by an internal-coordinate (local-mode[59, 60])

one, and the other is to correct for kinetic energy coupling of the torsions to one another. The factor Z_j is written for this purpose as

$$Z_j = \frac{g_j Q_{\mathrm{rot},j} Q_j^{\mathrm{HO}} + (1-g_j) Q_j^{\mathrm{imp}}}{Q_{\mathrm{rot},j} Q_j^{\mathrm{HO}}} \tag{16}$$

where Q_j^{imp} is an improved approximation, $g_j \to 1$ at low *T* where the effects of rotational-vibrational coupling are minimal, and $g_j \to 0$ at high *T*. We will approximate Q_j^{imp} as

$$Q_j^{\mathrm{imp}} = Q_{\mathrm{rot},j} Q_j^{\mathrm{HO}} Z_j^{\mathrm{int}} Z_j^{\mathrm{coup}} \tag{17}$$

where the Z_j^{int} replace the normal-mode vibrational partition functions in the high-*T* limit by internal-coordinate ones, and Z_j^{coup} replaces the uncoupled moments of inertia for individual torsions by values that account for their coupling.

Before considering the approximations used for g_j, Z_j^{int}, and Z_j^{coup} we need to consider the high-*T* limit of the denominator of eqn (16):

$$\lim_{T\to\infty} Q_{\mathrm{rot},j} Q_j^{\mathrm{HO}} = \frac{\sqrt{\pi}}{\sigma_{\mathrm{rot},j}} \left(\frac{2}{\mathsf{h}^2\beta}\right)^{3/2} \left|\det \mathbf{I}_j^{\mathrm{rot}}\right|^{1/2} \left(\frac{1}{\mathsf{h}\beta}\right)^{F} \prod_{m=1}^{F} \omega_{j,m}^{-1} \tag{18}$$

where $\mathbf{I}_j^{\mathrm{rot}}$ is the 3×3 moment of inertia matrix for overall rotation of structure *j* and $\omega_{m,j}$ is a normal-mode frequency. We do not factor the vibrational part of eqn (18) into a stretch-bend factor and a torsion factor because we avoid assigning torsions to specific normal modes.

At high-temperature the torsions become more separable from the other vibrations and it is reasonable to replace the product of normal-mode frequencies in eqn

(18) by the product of the $\overline{\omega}_{j,\tau}$ torsional frequencies and $F-t$ stretch-bend frequencies $\overline{\overline{\omega}}_{j,\overline{\overline{m}}}$ in the space orthogonal to the torsions. Note that $\overline{\overline{m}}$ is a generalized normal-mode label that is not based on normal modes. In particular we take

$$Z_j^{\text{int}} = \frac{\prod_{\overline{\overline{m}}=1}^{F-t} \overline{\overline{\omega}}_{j,\overline{\overline{m}}}^{-1} \prod_{\tau=1}^{t} \overline{\omega}_{j,\tau}^{-1}}{\prod_{m=1}^{F} \omega_{j,m}^{-1}} \tag{19}$$

where the $\overline{\overline{\omega}}_{j,\overline{\overline{m}}}$ are obtained from the Wilson GF matrix method[53-58]

$$\mathbf{GFL} = \mathbf{L}\Lambda \tag{20}$$

where the dimensions of the **G** and **F** matrices are reduced to $(F-t)\times(F-t)$, **L** is the matrix of the generalized normal mode eigenvectors, Λ is the eigenvalue matrix and its diagonal elements are the square of the vibrational frequencies. The **F** matrix in internal coordinates is obtained by

$$\mathbf{F} = \mathbf{A}^{\mathsf{T}}\mathbf{F}^{\text{Cart}}\mathbf{A} \tag{21}$$

where **A** is the generalized inverse of the Wilson **B** matrix, $\mathbf{F}^{\text{Cart}}$ is the force constant matrix in Cartesian coordinates, and T denotes a transpose. The Wilson **B** matrix constructed here only contains the non-torsional internal coordinates and the rows for torsional internal coordinates are removed; therefore its dimension is $(F-t)\times 3N$. The G matrix is given by

$$\mathbf{G} = \mathbf{BuB}^{\mathsf{T}} \tag{22}$$

where **u** is a diagonal matrix with the reciprocals of the atomic masses on the diagonal. We note that whereas the $f_{j,\tau}$ do not depend on the moments of inertia, as shown in

eqn (15b), the product $Q_j^{\mathrm{HO}} Z_j^{\mathrm{int}} \prod_{\tau=1}^{t} f_{j,\tau}$ approaches the uncoupled-torsion high-T limit given by $\prod_{\overline{\overline{m}}=1}^{F-t} \mathsf{h}\beta\overline{\overline{\omega}}_{j,\overline{\overline{m}}}^{-1} \prod_{\tau=1}^{t} q_{j,\tau}^{\mathrm{FR}} / P_{j,\tau}$.

Next, we consider Z_j^{coup}. In eqns (5) and (12)–(15), we employ the torsional moment-of-inertia approximation of Pitzer,[46] which is the best one can do for a torsion uncoupled to other torsions; however, we can obtain a more accurate result by allowing the torsions to be coupled to one another. To account for this coupling in the free-rotor high-T limit we need a correction factor equal to

$$Z_j^{\mathrm{coup}} = \left(\frac{\left|\det \mathbf{D}_j\right|}{\prod_{\tau=1}^{t} I_{j,\tau}} \right)^{1/2} \tag{23}$$

where **D** is the kinetic energy matrix for internal rotation of Kilpatrick and Pitzer.[47]

Finally we consider g_j. A simple expression having the correct limits and the approximately correct functional form[7] is

$$g_j = \left(\prod_{\tau=1}^{t} \tanh \frac{q_{j,\tau}^{\mathrm{FR}}}{P_{j,\tau} q_{j,\tau}^{\mathrm{CHO}}} \right)^{1/t} \tag{24a}$$

and eqn (24a) can be rearranged to

$$g_j = \left(\prod_{\tau=1}^{t} \tanh \frac{\sqrt{2\pi k_{j,\tau}\beta}}{M_{j,\tau}} \right)^{1/t} \tag{24b}$$

From a computational point of view we note that the partition function is independent of $\left|\det \mathbf{D}_j\right|$ and $\overline{\omega}_{j,\tau}$ when $g_j \to 1$.

Equations (4), (15b), (16), and (24b) constitute our final result for the MS-AS method. Therefore, the MS-AS method does not require any saddle point optimization or scanning to determine torsional barriers, and one only needs information for each minimum.

2.2.2 Alternative derivation. In Sect. II.B.1 the MS-AS method was introduced via an ansatz in which we assumed that the spacing between structures along a particular torsional coordinate τ was approximately uniform. We now present a derivation of the MS-AS approximation from an alternative point of view.

If we assume that the torsional motion is uncoupled to the remaining degrees of freedom the partition function would factor as

$$Q \approx Q_{\perp} Q^{\text{torsions}} \tag{25}$$

where $Q_{\perp}$ denotes the contribution to the total partition function from all non-torsional degrees of freedom. The quantum mechanical torsional partition function could be approximated by a classical mechanical (CM) configuration integral scaled by a Pitzer–Gwinn quantum mechanical (QM) correction factor, F^{PG},

$$Q^{\text{torsions}} \approx F^{\text{PG}} Q^{\text{torsions,CM}} \tag{26}$$

and the classical mechanical torsional partition function could be approximated as[47]

$$Q^{\text{torsions, CM}} = \left(\frac{1}{2\pi\beta h^2} \right)^{t/2} \left(\det\{\mathbf{D}\} \right)^{1/2} \int_0^{2\pi/\sigma_1} \cdots \int_0^{2\pi/\sigma_t} d\phi_1 \cdots d\phi_t \exp\left[-\beta V(\phi_1, \ldots, \phi_t) \right] \tag{27}$$

where the torsional kinetic energy matrix, **D**, is evaluated at the global minimum and its coordinate dependence has been neglected. We now assume that the topography of the torsional subspace is characterized by *J* distinct basins each characterized by a (local-)minimum-energy structure. We further assume that we can subdivide the torsional space into a set of disjoint subdomains Ω_j. If we relax the requirement of eqn (25) so that the torsional motion is only uncoupled from the remaining degrees of freedom within a particular subdomain we obtain the approximation

$$Q = \sum_{j=1}^{J} Q_{j\perp} \left(\frac{1}{2\pi\beta\hbar^2} \right)^{t/2} \left(\det\{\mathbf{D}_j\} \right)^{1/2} F_j^{\mathrm{PG}} \int_{\Omega_j} d\phi_1 \cdots d\phi_t \exp\left[-\beta V(\phi_1, \ldots, \phi_t) \right] \qquad (28)$$

We proceed by approximating the subdomains Ω_j as

$$\frac{-\pi}{\overline{M}_{j,\tau}} \le \phi_\tau - \overline{\phi}_{j,\tau} \le \frac{\pi}{\overline{M}_{j,\tau}}; \; \tau = 1, \ldots, t \qquad (29)$$

where $\overline{M}_j$ can be integer or non-integer, and $\overline{\phi}_{j,\tau}$ denotes the center of the subdomain *j*. The requirement that the subdomains span the entire torsional subspace leads to the result that

$$\sum_{j=1}^{J} \prod_{\tau=1}^{t} \frac{\sigma_\tau}{\overline{M}_{\tau,j}} = 1 \qquad (30)$$

We further assume that the potential is separable in the torsional coordinates within a subdomain, i.e., that

$$V(\phi_1, \ldots, \phi_t) \approx \sum_{\tau=1}^{t} V_{j,\tau}(\phi_\tau) \qquad (31)$$

and that the separable 1-D potentials may be approximated as

$$V_{j,\tau} = U_j + \frac{W_{j,\tau}}{2} \left[1 - \cos \tilde{M}_{j,\tau} (\phi_\tau - \phi_{\tau,\mathrm{eq.}\,j}) \right] \qquad (32)$$

where the $\phi_{\tau,\mathrm{eq.}\,j}$ denote, as before, the equilibrium torsion angles of structure *j*, the $\tilde{M}$ are periodicity parameters, and the remaining parameters are the same as discussed in Sect. II B.1. We define

$$\overline{P}_j = \frac{\overline{M}_j}{\sigma_\tau} \tag{33}$$

and

$$\tilde{P}_{j,\tau} = \frac{\tilde{M}_{j,\tau}}{\sigma_\tau}. \tag{34}$$

The expression in eqn (28) reduces to the MS-AS approximation if we take

$$Q_{j\perp} = Q_{\mathrm{rot},j} \exp\left(-\beta U_j\right) Q_j^{\mathrm{HO}} \frac{Z_j}{Z_j^{\mathrm{coup}}} \prod_{\tau=1}^{t} \frac{1}{q^{\mathrm{QHO}}(\overline{\omega}_{j,\tau})}, \tag{35}$$

where $q^{\mathrm{QHO}}(\overline{\omega}_{j,\tau})$ is a quantum mechanical harmonic oscillator partition function for an oscillator with a frequency $\overline{\omega}_{j,\tau}$ given by eqn (5), the Pitzer–Gwinn correction factors are calculated via

$$F_j^{\mathrm{PG}} = \prod_{\tau=1}^{t} \frac{q^{\mathrm{QHO}}(\overline{\omega}_{j,\tau})}{q^{\mathrm{CHO}}(\overline{\omega}_{j,\tau})}, \tag{36}$$

and if we take

$$\overline{M}_{j,\tau} = \tilde{M}_{j,\tau} = M_{j,\tau}, \tag{37}$$

From the above derivation we can see that the parameter $M_{j,\tau}$ plays three roles in the MS-AS method. Firstly, it controls the local periodicity by means of eqns (8) and (32). Secondly, it determines the implicit barrier height by eqn (13). Thirdly, it determines the volume of the torsional subspace spanned by a particular structure.

2.3. MS-ASCB method

In this section we present a higher-level MS method that explicitly includes the conformational barrier (CB) heights and barrier positions in the $f_{j,\tau}$ by using the segmented reference Pitzer–Gwinn[14, 61] (SRPG) approximation; this is called the MS-ASCB method, where ASCB denotes "based on all structures and conformational barriers". In the SRPG approximation, a more realistic reference potential is obtained by interpolating the region between each barrier and well with its own reference potential. This yields a continuous torsional potential given by

$$V_{j,\tau} = \begin{cases} U_j + \dfrac{W_{j,\tau}^{L}}{2}\left[1-\cos\left(\dfrac{(\phi_\tau - \phi_{\tau,\mathrm{eq}.j})\pi}{(\phi_{\tau,\mathrm{eq}.j} - \phi_{j,\tau}^{\mathrm{L}})}\right)\right]; & \phi_{j,\tau}^{\mathrm{L}} \le \phi_\tau \le \phi_{\tau,\mathrm{eq}.j} \\ U_j + \dfrac{W_{j,\tau}^{R}}{2}\left[1-\cos\left(\dfrac{(\phi_\tau - \phi_{\tau,\mathrm{eq}.j})\pi}{(\phi_{j,\tau}^{\mathrm{R}} - \phi_{\tau,\mathrm{eq}.j})}\right)\right]; & \phi_{\tau,\mathrm{eq}.j} \le \phi_\tau \le \phi_{j,\tau}^{\mathrm{R}} \end{cases} \tag{38}$$

This scheme yields

$$f_{j,\tau}^{\text{MS-ASCB}} = \sigma_\tau \left[\frac{q_{j,\tau}^{\mathrm{SRC}}}{q_{j,\tau}^{\mathrm{CHO}}}\right] \tag{39}$$

where

$$\begin{aligned} q_{j,\tau}^{\mathrm{SRC}} = q_{j,\tau}^{\mathrm{FR}}\Bigg[& \frac{(\phi_{\tau,\mathrm{eq}.j} - \phi_{j,\tau}^{\mathrm{L}})}{2\pi}\exp(-\beta W_{j,\tau}^{\mathrm{L}}/2) I_0(\beta W_{j,\tau}^{\mathrm{L}}/2) \\ & + \frac{(\phi_{j,\tau}^{\mathrm{R}} - \phi_{\tau,\mathrm{eq}.j})}{2\pi}\exp(-\beta W_{j,\tau}^{\mathrm{R}}/2) I_0(\beta W_{j,\tau}^{\mathrm{R}}/2)\Bigg], \end{aligned} \tag{40}$$

the zero of energy is taken as U_j, $W_{j,\tau}^{\mathrm{L}}$ and $W_{j,\tau}^{\mathrm{R}}$ are the left and right barrier heights, respectively, for torsion mode τ of structure j, and $\phi_{j,\tau}^{\mathrm{L}}$ and $\phi_{j,\tau}^{\mathrm{R}}$ are the locations of

these barriers. In contrast to the MS-AS scheme, the barrier heights in the SRPG method have to be calculated by scans or by optimizing all saddle points connecting all the structures, which adds significant computational cost and human effort.

2.4. MS-AS method for strongly coupled torsions

Occasionally a subset of the torsional coordinates may be so strongly coupled that it is difficult or impossible to assign a set of $M_{j,\tau}$ parameters in the MS-AS method, even when allowing for non-integer values as suggested in II.B.2. For such cases we present a strongly coupled option for the MS-AS method that is parameterized by Voronoi tessellation.[42-44]

In the strongly coupled MS-AS scheme we partition the torsional space into a set of nearly separable (NS) coordinates and a set of strongly coupled (SC) coordinates. In general, the strongly coupled coordinates may be further partitioned into two or more subspaces, with each subspace involving only those coordinates that are strongly coupled to each other. However, for simplicity in the following discussion, we will outline only the case for a single subspace of SC coordinates; the generalization to treat multiple subspaces of SC coordinates is straightforward. We will denote the number of NS coordinates as t_{NS} and the number of SC coordinates as t_{SC}, where $t_{NS} + t_{SC} = t$, and we will label particular coordinates in these subspaces by subscripts τ_{NS} and τ_{SC}, respectively.

Voronoi tessellation divides a space into cells around a discrete set of points. In our application, the space to be tessellated is described by the dihedral angles

$\phi_1,\phi_2,...,\phi_{t_{SC}}$ and the points correspond to structures. Each cell corresponds to a specific structure and consists of all torsional configurations closer to this structure than to any other structure when only the t_{SC} strongly coupled degrees of freedom are considered. We used the Euclidean norm for our distance metric. In principle, we could work with only the symmetry unique portion of the torsional space; however, because we choose to work with ordinary dihedral angles rather than symmetrized coordinates, and (as discussed earlier) these coordinates can display slight deviations from the true symmetry of the system, we do not exploit symmetry in this portion of the calculation. Thus, in order to tessellate the space we include two kinds of points. The first kind is the coordinates (sets of t_{SC} dihedral angles) of the distinguishable structures; the second kind is the coordinates of minima of the potential energy function that correspond to indistinguishable structures but where the angles are determined by adding $2\pi/\sigma_{\tau_{SC}}$ to selected angles of the associated distinguishable structure. We label the points $\tilde{j}$ = 1, 2, …, $\tilde{J}$, where $\tilde{J}$ is greater than or equal to *J*. For example, if we were treat the torsions of propane as strongly coupled (actually they are nearly separable), we would have *J* = 1 and $\tilde{J}$ = 9. We label the points as $\tilde{j}$ = 1, 2, …, *J* for distinguishable structures and $\tilde{j}$ = *J* + 1, *J* + 2, …, $\tilde{J}$ for indistinguishable structures. One may then calculate the volume $\Omega_{\tilde{j}}^{SC}$ of each cell and associate that volume with that point. We calculate the cell volumes using the convex hull code *hull* of Clarkson.[62, 63] In order to properly handle the periodic nature of the coordinates, we include periodic replicas in the tessellation calculation.

By definition, the volume of the SC torsional subspace neglecting indistinguishability of identical particles is

$$\Omega^{\mathrm{SC,tot}} = \sum_{\tilde{j}=1}^{\tilde{J}} \Omega_{\tilde{j}}^{\mathrm{SC}} = (2\pi)^{t_{\mathrm{SC}}} \tag{41}$$

After accounting for indistinguishability, the total volume of the SC torsional subspace may be calculated by

$$\Omega^{\mathrm{SC}} = \sum_{\tilde{j}=1}^{J} \Omega_{\tilde{j}}^{\mathrm{SC}} \tag{42}$$

we should find that

$$\frac{\Omega^{\mathrm{SC}}}{\Omega^{\mathrm{SC,tot}}} = \frac{1}{\sigma_1 \sigma_2 \ldots \sigma_{t_{\mathrm{SC}}}} \tag{43}$$

but slight deviations may occur due to symmetry distortions resulting from the limitations of working in a coordinate system of ordinary dihedral angles. In such cases it may be desirable to rescale the distinguishable volumes so that this equality holds exactly or to work with volumes that are averages of selected distinguishable and indistinguishable structures that are related by additional symmetries (see the later discussion of mirror image structures of pentyl radical for an example).

When the torsional subspace is so strongly coupled that we cannot assign $M_{j,\tau_{\mathrm{SC}}}$ by considerations based on considering each torsion separately, then we replace all $M_{j,\tau_{\mathrm{SC}}}$ for strongly coupled torsions of a given *j* by a single M_j^{SC} equal to

$$M_j^{\mathrm{SC}} = \frac{2\pi}{\left(\Omega_j^{\mathrm{SC}}\right)^{1/t_{\mathrm{SC}}}} \tag{44}$$

When this is done, eqn (30) with $\overline{M}_{j,\tau}$ replaced by $M_{j,\tau}$ is automatically satisfied if eqn (43) holds.

When the SC method is used, the intrinsically separable effective potentials of eqn (8) are no longer defined. The strongly coupled MS-AS scheme is not a classical partition function, augmented by a Pitzer–Gwinn quantum correction, for a particular effective torsional potential. Instead, it is an interpolation scheme that yields correct values in the low- and high-temperature limits and gives reasonable values between these limits.

If one treats all the coordinates as if they constitute a single set of strongly coupled coordinates, then the Voronoi tessellation, together with the equations above, provides a fully automatable way of assigning the *M* parameters. However, grouping nearly separable degrees of freedom together with strongly coupled ones results in an approximation in which the contribution to the partition function of the nearly separable torsions is not expected to be as accurate as when one uses the method of Section II.B.1 for these torsions. Thus, we recommend keeping the dimensions of the SC subspaces as small as is feasible. That is, we recommend assigning torsions to SC subspaces only when they are coupled so strongly that we cannot assign $M_{j,\tau_{\mathrm{SC}}}$ values based on considering each torsion separately.

2.5. MS-RS method

Although wherever feasible we strongly recommend the inclusion of all structures in the partition function calculation, as is done in the MS-AS scheme, we recognize that a lower level of treatment is needed in some circumstances where the

harmonic approximation is qualitatively incorrect and where finding and optimizing all structures requires too much work. In such instances, we propose a reference-structure treatment involving the generation of structures by independent torsions. To apply this method, one chooses one structure as a reference structure, and one considers only the other structures that can be generated by independently rotating the torsions, one at a time. One can start from any reasonable reference structure. If any structure among the generated structures is found to have a lower energy than the starting structure, one can optionally start over taking this lower-energy structure as the new reference structure. The number of structures that needs to be optimized for this approach scales linearly with the number of torsions, *t*, so for large molecules it can be much more affordable than the MS-AS scheme where the number of structures scales exponentially with *t*.

Label the reference structure as $j = 1$, and number the distinguishable structures, which are denoted $j[\tau, i(\tau)]$, generated by rotating about torsional coordinate τ in the reference structure as $i(\tau) = 1, \ldots, P_{1,\tau}$. We adopt the convention that $i(\tau) = 1$ corresponds to a null rotation, which leads to the reference structure for every τ. We define the multi-structure reference-structure (MS-RS) approximation to the conformational-rovibrational partition function as

$$Q_{\text{con-rovib}}^{\text{MS-RS}} = Q^{\text{ref}} \prod_{\tau=1}^{t} \sum_{i(\tau)=1}^{P_{1,\tau}} \frac{Q_{j[\tau, i(\tau)]}^{\text{IT}}}{Q_{j=1}^{\text{IT}}} \tag{45}$$

where

$$Q^{\text{ref}} = Q_{\text{rot},1} \exp(-\beta U_1) Q_1^{\text{HO}} Z_1 \prod_{\tau'=1}^{t} f_{1,\tau'} \tag{46}$$

$$Q_j^{\mathrm{IT}} = Q_{\mathrm{rot},j} \exp\left(-\beta U_j\right) Q_j^{\mathrm{HO}} Z_j \prod_{\tau'=1}^{t} P_{j,\tau'} f_{j,\tau'} \qquad (47)$$

and the remaining quantities are the same as those discussed for the MS-AS method. Notice that in eqn (46) we set $j = 1$, which denotes the reference structure. If the reference structure is not the lowest-energy structure included, then U_1 need not be zero (as it was in the MS-AS and MS-ASCB methods); in general, U_j is 0 for the lowest-energy structure included in eqn (45), and for all the other structures, U_j is the equilibrium potential energy relative to the lowest-energy structure included. The inclusion of the $P_{j,\tau'}$ factor in eqn (47) results in the Q_j^{IT} being scaled by a quantity proportional to the volume of the torsional subspace spanned by this structure; thus, the ratio of factors in eqn (45) properly accounts for the differences in the domain sizes of the various structures. Notice $P_{j,\tau}$ used in MS-RS method is obtained from $M_{j,\tau}$ and σ_τ by eqn (1).

Notice that the $P_{j,\tau}$ and σ_τ are not directly needed for the MS-AS method (unlike $M_{j,\tau}$, they cancel out in the final equations, although their knowledge is useful for ascertaining whether or not all the structures are accounted for); however, the MS-RS method explicitly requires the $P_{j,\tau}$ (or the σ_τ from which they may be calculated by eqn (1)) as well as $M_{j,\tau}$. Except for the $P_{j,\tau}$, the MS-RS method requires no information that is not needed for MS-AS calculations, and it requires information for only a subset of the structures. In cases where a subset of torsional motions are strongly coupled the MS-RS scheme may not perform as well as when the coupling is small; in such instances one may seek extensions of the MS-RS scheme that, for instance, treat

the NS torsions independently but which include additional structures obtained by modifying the reference structure by two or more simultaneous rotations from within the SC torsional subspace. Such extensions may provide additional accuracy while retaining the desirable computational scaling of the MS-RS approach, but they are beyond the scope of the present study.

3. Results

To illustrate the MS methods, we apply the MS-HO, MS-AS, and MS-ASCB methods to two one-dimensional (1-D) model potentials and to ethanol. Note that the MS-AS and MS-RS methods are identical for some simple cases such as ethanol and 1-D potentials. However, we will compare the MS-HO, MS-AS, and MS-RS methods for 1-butanol and 1-pentyl radical in the present study.

The M06-2X[64] density functional was used for calculating the geometries and energetics of ethanol and the 1-pentyl radical, and the MPW1K[65] density functional was used for 1-butanol. The 6-311+G(2df,2p) basis set[66, 67] was used for all the calculations. All density functional calculations were performed using the *Gaussian 09* program.[68]

Because meta-GGA density functionals are sensitive to integration grids, we performed a grid-convergence analysis on the frequencies of ethanol and 1-pentyl radical using the M06-2X/6-311+G(2df,2p) method. As shown in Table 1.1, the frequencies calculated by M06-2X/6-311+G(2df,2p) are well converged when one uses the density functional integration grid that has 99 radial shells around each atom and 974 angular points in each shell. Therefore this grid (99, 974) was used for all M06-2X calculations in this article. The pruned (99, 590) grid, which is called *ultrafine* in

Gaussian09, was used for calculations with the MPW1K functional, which are less sensitive to the fineness of the integration grids.

All the minima of ethanol, 1-pentyl radical, and 1-butanol are fully optimized and confirmed by normal-mode analysis. The saddle points of ethanol that connect the minima are also optimized and are confirmed to have one imaginary frequency.

Table 1.2 shows the notation that is used for torsion angles in this paper. This notation is based on standard notation but is also specialized to the needs of the present study.

Partition functions are calculated from 100 K to 50000 K. The 50000 K result is tabulated not because this is an accessible temperature, but rather to illustrate the high-temperature limit for formal purposes.

The frequencies ($\omega_{j,m}$, $\overline{\omega}_{j,\tau}$, and $\overline{\overline{\omega}}_{j,\overline{\overline{m}}}$) used in the calculations are all scaled and the scaling factors designed to give accurate ZPEs are used.[69]

We also employed Benson's group additivity (GA) method[30, 31, 70] to calculate entropies of ethanol, 1-pentyl radical, and 1-butanol for comparison. For this purpose we use not only Benson's[30] group parameters but also those of Cohen[31] and Lay et al.[34]

3.1. 1-D models

In order to better understand the proposed methods, we first apply them to two 1-D torsion models. One is an artificial 1-D model potential designed to show the effect of a shallow minimum, and the other is the 1-D torsion potential of H_2O_2 from the work of Koput *et al.*[71] that has been used in a prior study[14] of torsional methods.

The first 1-D model potential is given by

$$V/\mathrm{cm}^{-1} = 121.352549 + 90.0\cos(2\phi) + 60.0\cos(3\phi) \qquad (48)$$

where ϕ is the torsion angle. This potential has three minima in the range of $[0, 2\pi)$ and we assume they are all distinguishable, i.e., $M = P = 3$. This potential is plotted in Figure 1.1, and the rotational barrier heights and the locations of minima are also given in the figure. The internal moment of inertia is assumed to be 1.53618 amu Å^2 and to be independent of ϕ. The harmonic frequencies calculated using eqn (5) are 126.41 and 62.85 cm^{-1} for the deep and shallow minima, respectively.

The small barriers and the presence of a very shallow minimum for this potential make it an interesting model to test the proposed methods. The accurate partition functions were calculated by the torsional eigenvalue summation (TES) method.[14] The calculated partition functions and the percentage errors of the approximate schemes relative to the TES values are listed in Table 1.3.

Table 1.4 shows the errors of the multi-structural methods when the shallow minimum is ignored (because the MS-ASCB method requires information for all the barriers, it is not included in Table 1.4.). When ignoring this shallow well, we set $M = P = 2$ which alters the effective barrier heights of the reference potential.

The 1-D torsional potential for H_2O_2 is given by[71]

$$V/\mathrm{cm}^{-1} = 811.3053546 + 1037.4\cos(\phi) + 674.2\cos(2\phi) + 46.9\cos(3\phi) + 2.7\cos(4\phi) \qquad (49)$$

This potential energy curve is plotted together with the heights and locations of the barriers in Figure 1.2. The minima are mirror-image structures and are therefore distinguishable ($J = P = M = 2$). The internal moment of inertia is 0.423202 amu Å^2 and the harmonic frequency of each minimum is 382.6 cm^{-1}. This 1-D potential has

been studied in a previous paper[14] in which the effective barrier height used in the RPG scheme was chosen as the average of the two barrier heights. In the MS-AS method (which also uses the RPG scheme for torsions), the effective barrier height is calculated by eqn (13).

Table 1.5 lists the calculated partition functions and the percentage errors of the approximate schemes relative to the TES values for the 1-D potential of H_2O_2.

3.2. Ethanol

The ethanol molecule has two torsions. One involves internal rotation about the C–C bond, and the other involves internal rotation about the C–O bond. If the torsions are considered separately, they each have 3 minima along their torsion coordinates. The torsion around the C–C bond only has one distinguishable minimum because the three hydrogen atoms of the methyl group are identical whereas the torsion around the C–O bond leads to 3 distinguishable minima. Although two of these structures are isoenergetic, they are mirror images and thus distinguishable. Therefore, as shown in Figure 1.3, the ethanol molecule, with two torsions, has three distinguishable structures that contribute to the total partition function.

Table 1.6 lists the information used in the MS-AS and MS-ASCB calculations for ethanol. Table 1.7 lists the partition function calculated using the MS-HO, MS-AS, and MS-ASCB methods.

Figure 1.4 shows the percentage difference of the partition functions of structure E-t from that of E-g^+ or E-g^- using the harmonic approximation. Note that the each harmonic partition function used here takes its own minimum as the zero of energy.

Figure 1.5 shows the ratio of the partition function of ethanol calculated by the multi-structural method to that calculated by the single-structure HO (SS-HO) approximation (J, Z_j, and $f_{j,\tau}$ are equal to 1) at the global minimum (E–t).

3.3. 1-pentyl radical

The 1-pentyl radical has four torsions that are associated with internal rotation about each of the four C–C bonds. We label the five carbon atoms as: $H_2C^{(1)}$–$H_2C^{(2)}$–$H_2C^{(3)}$–$H_2C^{(4)}$–$H_3C^{(5)}$, and the four torsions are around the 1–2, 2–3, 3–4, and 4–5 C–C bonds, respectively. The 1-pentyl radical constitutes an example of a system displaying significant torsional coupling, in particular involving the $\tau = 1$ ($C^{(1)}$–$C^{(2)}$) and $\tau = 2$ ($C^{(2)}$–$C^{(3)}$) internal rotations; assigning $M_{j,\tau}$ parameters in such circumstances merits special care. In the absence of steric hindrance effects,[37-39] torsion involving a $–CH_2$ radical group is expected to have 6-fold periodicity and low barrier heights yielding three distinguishable minima. The 4–5 torsion is expected to have three total minima, only one of which is a distinguishable minimum, and the other two torsions are expected to have three total minima, all distinguishable. Thus, an uncoupled model would lead one to expect a total of 27 distinguishable structures. However, the total number of distinguishable structures of 1-pentyl radical is found to be only 15 as shown in Figure 1.6. The 15 structures include seven pairs of mirror-image structures (which of course have the same energy and vibrational frequencies); therefore we only need to perform electronic structure calculations on eight of the 15 structures. In larger

systems steric effects can lead to either a larger or smaller number of structures than would be expected based on a separable approximation.[40, 51]

In the absence of strong coupling the structures should correspond closely to minima encountered when the system is rotated about a single torsional coordinate. In this limit, $P_{j,\tau}$ assignments (and thus $M_{j,\tau}$ assignment after taking account of the torsional symmetry) may be made by starting with a particular structure, choosing a τ, and counting all structures (including the starting structure) that have similar torsional angles to the starting structure for every torsion except the τ torsion. This approach confirms the expected results of $P_{j,\tau=3} = 3$ and $P_{j,\tau=4} = 1$ for all values of *j*. A similar exercise for the τ = 1 torsion leads to 9 structures with expected values of $P_{j,\tau=1} = 3$ and six structures (P–a$^-$g$^+$t**,** P–a$^+$g$^-$t, P–a$^-$g$^+$g$^+$**,** P–a$^+$g$^-$g$^-$, P–a$^-$g$^+$g$^-$**,** P–a$^+$g$^-$g$^+$) with $P_{j,\tau=1} = 1$.

Relaxed scans starting from each of these six latter structures reveal a single broad structure spanning the entire 180 degrees of the symmetry-unique τ = 1 torsional degree of freedom each with a relatively large barrier—the effective barriers estimated by eqn (13) range from 451 to 654 cm^{-1} (using $M = 2$) as compared to values of 29 to 44 cm^{-1} (using $M = 6$) for the other 9 structures. The occurrence of these broad minima may be considered to arise from steric hindrance effects that outweigh the small barriers that one would anticipate existing between 3 expected structures in the absence of such steric effects. Thus, each of the 3 structures with broad features along the τ = 1 coordinate may be thought of as aggregations of 3 expected structures and therefore

these structures span a torsional subspace with a volume that is approximately 3 times as large as that spanned by the remaining 9 structures having assignments of $P_{j,\tau=1} = 3$.

In the absence of steric effects we would anticipate assignments of $P_{j,\tau=2} = 3$ for each of the structures, and such assignments would be consistent with the sum of the torsional subspace volumes of each of the structures totaling to the total volume (see eqn (30)), which serves as a convenient consistency check of possible assignments. Rigid scans along the $\tau = 2$ torsional coordinate reveal 3 distinct minima, but due to strong coupling with the $\tau = 1$ torsional degree of freedom, not all of these minima correspond closely with other structures. In particular, if we select a particular structure and look for all other structures having similar torsional angles for all torsional coordinates other than $\tau = 2$ we find either 0 or 1 additional structures and this suggests that the simple scheme for assigning $P_{j,\tau}$ values breaks down in the presence of strong torsional coupling. For example, if we start by considering the P–a^{-}g^{+}t structure we find only the P–a^{-}tt structure corresponds closely to the starting structure via a rotation about the $\tau = 2$ coordinate. In the presence of strong torsional coupling we need to generalize our criteria for assigning $P_{j,\tau}$ so that instead of looking only for structures having similar torsional angles to that of the structure undergoing assignment along $t - 1$ coordinates we look for structures for which the spans of the torsional minima strongly overlap with each of the spans of the torsional minima of the starting structure along $t - 1$ coordinates. Under this relaxed set of criteria we see that the P–a^{+}g^{-}t structure, which is one of the structures having a single broad minima along $\tau = 1$, overlaps with the torsional spans of P–a^{-}g^{+}t along the required $t - 1$ coordinates even

though the τ = 1 torsional angles of these two structures differ by about 54 degrees. Under this relaxed set of search criteria we are easily able to identify two other structures that are sufficiently similar to each structure undergoing assignment to yield assignments of $P_{j,\tau=2} = 3$ for all structures.

When employing the MS-RS method we need to identify all structures obtained by independent rotations from a reference structure. In this context, if we consider the reference structure to be P–a^{-}g^{+}t, the structures most consistent with independent rotation about the τ = 2 coordinate are the P–a^{-}tt and P–a^{+}g^{-}t structures. One of these is the mirror image structure of the reference structure, which shows that the concept of an independent internal rotation about a single torsional coordinate must be considered as highly approximate in the presence of strong torsional coupling. As we will see in the following, the results for the MS-RS and MS-AS methods show some consistency suggesting that both methods can, at least sometimes, yield reasonable partition functions even for cases where we have strong torsional coupling.

We also consider two variants of the strongly coupled option of the MS-AS scheme, one (denoted NS:SC = 2:2) which treats the 1–2 and 2–3 torsions as strongly coupled and one (denoted NS:SC = 1:3) which treats the 1–2, 2–3, and 3–4 torsions as strongly coupled. These methods not only take account of the strong coupling, but they eliminate the need for much of the analysis presented in the proceeding four paragraphs.

In the NS:SC = 2:2 scheme, the 15 structures are divided into 3 groups with the structures in each group have the same torsional conformation for the 3–4 torsion. In particular, the group with the 3–4 torsion in a trans conformation includes the structures P–a^{-}g^{+}t, P–a^{+}g^{-}t, P–a^{+}tt, P–a^{-}tt, and P–stt; the group with the 3–4 torsion in a g^{+}

conformation includes the structures P–a^{-}g^{+}g^{+}, P–a^{+}g^{-}g^{+}, P–a^{+}tg^{+}, P–a^{-}tg^{+}, and P–stg^{+}; and the group for with the 3–4 torsion in a g^{-} conformation includes the structures P–a^{+}g^{-}g^{-}, P–a^{-}g^{+}g^{-}, P–a^{-}tg^{-}, P–a^{+}tg^{-}, and P–stg^{-}. The Voronoi tessellation is performed considering each group separately.

In the Voronoi tessellation calculations, some indistinguishable structures are generated by symmetry. For example, if the P–a^{+}tt struture is denoted by its first three torsional angles as (159.7, 178.8, 179.9) and its corresponding indistinguishable structure is (–20.3, 178.8, 179.9) due to the 2-fold symmetry of the –CH_2 radical group. The angles 159.7 degrees and –20.3 degrees refer to the dihedral angle H_a–$C^{(1)}$–$C^{(2)}$-$C^{(3)}$ and H_b–$C^{(1)}$–$C^{(2)}C^{(3)}$. However, the optimized structure has the H_b–$C^{(1)}$–$C^{(2)}C^{(3)}$ angle as -30.4 degrees. This discrepancy is caused by using a dihedral angle to represent the torsion, which also has the effect that some mirror images have slightly different volumes (e.g. the volumes of P–a^{+}tt and P–a^{+}tt have about a 1% difference). If the two mirror images have different volumes, we used the averaged volume to calculate *M* values.

The structure P–a^{-}g^{+}t (the global minimum) is chosen as the reference structure in the MS-RS calculations. Independent rotations starting from this reference structure generate the structures P–a^{-}g^{+}g+, P–a^{-}g^{+}g^{-}, P–a^{-}tt, and P–a^{+}g^{-}t. These five structures are used in the MS-RS calculations.

Table 1.8 lists information for each structure of 1-pentyl radical that is used for the partition function calculations using various schemes for *M* values. Table 1.9 lists

the partition functions of 1-pentyl radical calculated by the MS-HO, MS-AS, and MS-RS methods.

Figure 1.7 shows the percentage differences of the harmonic oscillator partition functions of three structures relative to that of structure P–$a^{-}g^{+}t$ or P–$a^{+}g^{-}t$ (each harmonic oscillator partition function takes its own minimum as the zero of energy). Figure 1.8 shows the ratios of the partition function of 1-pentyl radical calculated by multi-structural methods to those calculated by the SS-HO approximation at the global minimum (P–$a^{-}g^{+}t$ or P–$a^{+}g^{-}t$).

3.4. 1-Butanol

We label the carbon atoms in 1-butanol as HO–$H_2C^{(1)}$–$H_2C^{(2)}$–$H_2C^{(3)}$–$H_3C^{(4)}$. The four torsions in 1-butanol are associated with internal rotation around each of the three C–C bonds and one C–O bond. Each torsion, with the exception of the methyl torsion, is expected to generate 3 distinguishable structures, and a total of 27 distinguishable structures is expected to be generated. However, due to steric hindrance between the terminal hydroxyl and methyl groups, the expected structures $g^{+}g^{-}g^{+}$ and $g^{-}g^{+}g^{-}$ are saddle points that connects $g^{+}x^{-}g^{+}$/$g^{+}g^{-}x^{+}$ and $g^{-}x^{+}g^{-}$/$g^{-}g^{+}x^{-}$ structures, respectively. A similar effect has also been observed in alkanes.[17, 51] Therefore, 1-butanol has a total of 29 structures. The 29 structures include 14 pairs of mirror-image structures; therefore, electronic structure calculations only needed to be performed for 15 structures. Two previous conformational studies[72, 73] of 1-butanol only observed 27 structures with the structures assigned as $g^{+}g^{-}g^{+}$ and $g^{-}g^{+}g^{-}$ being similar to our

$g^+x^-g^+$ and $g^-x^+g^-$ structures. The $g^+x^-g^+$ structure has torsional angles (for torsions 1–2, 2–3, and 3–4, respectively) of 60.0, 82.3, and 59.8, the $g^-g^+x^-$ structure has torsional angles of 73.4, –63.3, and 88.2, and the intervening transition state has torsional angles of 73.2, –68.9, and 81.9 degrees. The $g^+x^-g^+$ and $g^-g^+x^-$ structures lie 149 and 8 cm^{-1} below the intervening transition state, respectively.

The structure B–tg^+t is chosen as the reference structure in the MS-RS calculations. Starting from this reference structure, one can generate the structures B–g^+g^+t, B–g^-g^+t, B–ttt, B–tg^-t, B–tg^+g^-, and B–tg^+g^+ by independent rotation of each C–C bond or C–O bond. These seven structures are used in the MS-RS calculations.

If there were no steric hindrance effect in 1-butanol such that the torsions only generated 27 structures, the parameter $M_{j,\tau}$ would be 3 for each torsion. However, it is not trivial to set reasonable integer values of $M_{j,\tau}$ for the 29 structures that satisfy eqn (30). Therefore, we use the MS-AS method with NS:SC = 1:3 to determine the $M_{j,\tau}$ values by treating only the methyl group torsion as NS.

Given that the $g^+x^-g^+/g^+g^-x^+$ ($g^-x^+g^-/g^-g^+x^-$) structures overlap very strongly and the $g^+g^-x^+$ ($g^-g^+x^-$) structure is extremely shallow (being bound by only 7.9 cm^{-1}) it is reasonable to only include the lower energy structure of each pair in an MS-AS calculation involving 27 structures.

Table 1.10 lists the information for each structure of 1-butanol that is needed for the partition function calculations. Table 1.11 gives the calculated conformational-rovibrational partition functions of 1-butanol.

Table 1.12 lists the standard state entropy of ethanol, 1-pentyl radical, and 1-butanol calculated from SS-HO, MS-HO, and MS-AS partition functions including contributions from electronic and translational degrees of freedom, and also calculated using Benson's group additivity method; the global minimum structure is used for the SS-HO method. Table 1.12 also contains experimentally derived values[74, 75] for comparison.

Table 1.13 lists the calculated correction factors Z^{int} and Z^{coup} for structures of ethanol, 1-butanol, and 1-pentyl radical.

Figure 1.9 shows the two cases with the largest percentage difference of structure-specific harmonic oscillator partition functions relative to that of the global minimum (each harmonic oscillator partition function takes its own minimum as the zero of energy). Figure 1.10 plots the temperature dependence of the ratio of the partition function of 1-butanol calculated by the multi-structural methods to that calculated by the SS-HO approximation at the global minimum.

4. Discussion

We will begin by comparing the new MS-AS methods to accurate results of 1-D models so that we can demonstrate their accuracy for treating intra-mode anharmonicity without complications from mode-mode coupling and anharmonicities of other vibrational modes. We have already extensively studied[14] methods to treat the intra-mode anharmonicity; herein we will only compare to the accurate values from torsional eigenvalue summation. Expansion of a torsional potential in terms of a Fourier series, along with the assumption of a constant moment of inertia, leads to a banded symmetric

matrix that may be diagonalized with negligible computational expense. This technique has a long history[14, 19, 20, 76-81] and it might seem tempting to apply it whenever the additional energy evaluations needed for fitting the Fourier potential are affordable. However, there is little benefit to treating the intramode anharmonicity to a much higher degree of accuracy than we can treat the intermode anharmonicity; this is especially true in applications[19, 20] where multiple torsional modes are so treated because coupling between torsional degrees of freedom is often very important. Treatment of the inter-mode anharmonicity, which we achieve primarily by including multiple structures, is a much harder task and the primary goal of the new methods presented herein, but we begin by demonstrating that the methods also treat intramode anharmonicity well.

Table 1.3 clearly shows that the MS-HO approximation significantly overestimates the torsional partition function at high temperature and modestly underestimates the torsional partition function at low temperatures for the 1-D model of eqn (48). For this model torsion and most typical torsional potentials where the barriers are not very low, the MS-HO approximation is adequate for practical work at low temperatures. Due to cancellation of error, the MS-HO approximation may have quite small errors at some temperatures (e.g., 300 K for this 1-D model potential).

The MS-AS and MS-ASCB methods both use the Pitzer–Gwinn approximation based on a reference classical partition function, but they require different information about the torsional potential. They both need the energies, frequencies, and geometries of all structures that are local minima of the potential energy surface, and the MS-ASCB method also needs the locations and magnitudes of the torsional barriers. For this 1-D potential, the barriers of the deep wells are 271 cm^{-1} and 1678 cm^{-1} for each side,

respectively; the shallow well has a symmetric barrier of 16 cm^{-1}. Equation (13) gives effective barriers of 1612 cm^{-1} and 40 cm^{-1} for the deep and shallow wells, respectively. Although the MS-AS and MS-ASCB methods use different effective barriers, they both have errors of less than 3% for the potential of eqn (48) at temperatures above 100 K. The predominant source of errors of both methods at low temperatures (e.g., 60 K) is the Pitzer–Gwinn approximation, which only puts the quantum effects in at a harmonic level.

For the 1-D model potential of eqn (48), there is a very shallow minimum as shown in Figure 1.1. On the potential energy surface of a real molecule, the geometry of such a shallow minimum may be hard to find and optimize. Also for complex molecules, finding all possible shallow minima may prove difficult, so we consider the consequences of neglecting them for this model problem. When the shallow minimum is ignored, the calculated effective barrier using eqn (13) is 364 cm^{-1} with $M = P = 2$. Table 1.4 shows that for $T \leq 1000$ K the two multi-structural methods (MS-HO and MS-AS) both underestimate the partition function when using two minima compared to that calculated by using three minima. At higher temperatures the MS-AS method has errors smaller than 7% when the shallow minimum is ignored. In the high-temperature limit (illustrated by 50000 K), the error of the MS-AS method is negligible even without explicitly accounting for the shallow minimum because the torsional partition function approaches a free rotor partition function, which is independent of the potential. These results suggest that accounting for shallow minima can be important if their energies are low (151.36 cm^{-1} in the 1-D model potential of eqn (48)) especially at temperatures of 400 K and lower.

The exact barrier heights on the two sides of each minimum for the 1-D torsional potential of H_2O_2 (eqn (49)) are 2545 cm^{-1} and 377 cm^{-1}, and this large difference presents a significant challenge for the MS-AS method as it assumes a single barrier height. The effective mean barrier height calculated by eqn (13) and used in the MS-AS method is 919 cm^{-1}. Although this value is quite different from the exact ones, Table 1.5 shows that the MS-AS method has errors no larger than 13% from 200 to 3000 K, with the largest error at 1500 K, where the error corresponds to an error of only 0.36 kcal/mol in the free energy. This 1-D case shows that accurate barrier height information does improve the accuracy of the calculated partition function through the use of the MS-ASCB method, but that the calculated partition function is not too sensitive to the barrier heights. Because one of the two barriers on this potential energy surface is very high, the MS-HO approximation gives adequate results from 300 to 2400 K.

Ethanol is a simple molecule that has two torsions. As shown in Table 1.3, the two torsions around the C–O and C–C bonds have very close frequencies when modeled using internal coordinates. In the normal mode analysis, the two torsional motions are strongly coupled, and consequently the two lowest-frequency modes are mixtures of two torsional motions. The normal mode with the lowest frequency is the antisymmetric combination of two torsions, and the mode with the second lowest frequency is the symmetric combination. Therefore, even such a simple molecule as ethanol provides a case where it is impossible to assign the torsions to specific normal modes. The barrier heights calculated by eqn (13) are 1109, 329, 1206, and 379 cm^{-1}

and agree very well with the normal modes optimized by the M06-2X/6-311+G(2df,2p) method, which are1109, 386, 1195, and 359 cm^{-1}.

To apply the MS-ASCB method to ethanol, one needs to calculate the torsion angle difference $\phi_{\tau,\text{eq}.j} - \phi^{\text{L}}_{j,\tau}$ or $\phi^{\text{R}}_{j,\tau} - \phi_{\tau,\text{eq}.j}$. For the ethanol calculations, we use a single dihedral angle to represent a torsion angle although one could also construct a torsion coordinate involving a top rotating about a fixed frame from a combination of several related dihedral angles.[48-50] The $\Delta\phi^{\text{R}}$ and $\Delta\phi^{\text{L}}$ of the C–C torsion are set to 60 degrees due to the symmetry. The $\Delta\phi^{\text{R}}$ and $\Delta\phi^{\text{L}}$ of C–O is measured by the dihedral angle H-O-C-C; they are both 61.8 and degrees for structure E-t and are both 59.1 degrees for structures E-g^+ and E-g^-.

When conformational structures change by internal rotations, the other vibrational frequencies (e.g. stretching and bending modes) also change correspondingly. One of advantages of the multi-structural methods is that anharmonicities and couplings due to conformational changes are partially accounted for by the use of a different harmonic analysis at each structure. To illustrate the effect of conformational changes on partition functions, Figure 1.4 shows the percentage difference of the ethanol E-g^+ or E-g^- HO partition function from that of the global minimum E-t. Although the E-t and E-g^+ (or E-g^-) structures have quite similar conformations, this difference can be as large as 12%. The differences are larger for 1-pentyl radical and 1-butanol. Because many conformational structures of 1-pentyl radical are quite different from the global minimum, the effects of conformational changes on partition functions are very large as shown in Figure 1.7. Even larger effects

are observed for 1-butanol as shown in Figure 1.9. Therefore, treating torsions as separable with the frequencies of the other modes fixed at their values for the global minimum structures can introduce large errors.

When the harmonic approximation is applied to calculate partition functions in the literature, often only one structure (the global minimum) is considered. Therefore we compared the ratio of partition functions calculated by multi-structural methods to those calculated by the harmonic approximation for the global minimum. Because ethanol has three conformational structures, the partition functions calculated by multi-structural methods are larger than those calculated by the HO approximation using one structure, and the factors are between 1.9 and 3.4 in the temperature range 200–3000 K as shown in Figure 1.5. Because the 1-pentyl radical and 1-butanol have many more conformational structures, the partition functions calculated by the multi-structural methods are *much* larger than the harmonic ones obtained using only the global minimum structure as shown in Figure 1.8 and Figure 1.10, respectively. For example, at T = 1000 K, the MS-AS partition function of 1-butanol is larger than that of the SS-HO approximation by a factor of 31.

Standard state entropies calculated from the SS-HO, MS-HO, and MS-AS partition functions for ethanol, 1-pentyl radical, and 1-butanol are compared to each other and to the GA method and reference data in Table 1.12. The reference data for ethanol is based on spectroscopic data and a reference structure treatment of anharmonicity; the reference data for 1-butanol is based on experimental heat capacities and heats of fusion and vaporization; and there is no available reference data for the 1-pentyl radical. The entropies calculated by the MS-HO method are in much better

agreement with the reference data than is the single-structure HO data, and the entropies calculated by the MS-AS method give even better agreement for both ethanol and 1-butanol at the temperature studied. The entropies calculated by various parametrizations of the GA method are also listed in Table 1.12 for comparison. For ethanol and 1-butanol we only calculate entropies up to 1000 K because the heat capacities C_p are available only up to 1000 K for an OH group, and extrapolation may not be reliable. All the GA calculations use the parameters from the Benson's tables[30] except some calculations for 1-pentyl radical also use the parameters from Cohen's[33] and Lay et al.'s[34] work. Benson has estimated[30] that "Values of C_p^o and S^o estimated from these groups are on the average within ±0.3 cal mol^{-1} K^{-1} of the measured values..." and "for heavily substituted species, deviations in C_p^o and S^o may go as high as ±1.5 cal mol^{-1} K^{-1}..." We find that the difference of the GA data from the MS-AS data and the reference data sometimes exceed these estimated uncertainties. The GA calculations for 1-pentyl radical obtained using Cohen's parameters agree better with the MS-AS values than those obtained using Benson's or Lay et al.'s parameters.

In the intermediate-temperature region, the values of the MS-AS partition functions of ethanol, 1-pentyl (using the 2:2 scheme), and 1-butanol (using the 1:3 scheme) are larger than those of the MS-HO partition functions. However, the MS-AS partition functions of 1-pentyl radical with all four torsions treated as nearly separable are almost the same as or lower than the MS-HO partition functions. This is because the torsion around the C$^{(1)}$–C$^{(2)}$ bond in the 1-pentyl radical has a very low barrier predicted by M = 6, and its torsional correction factor $f_{j,\tau}$ is already smaller than 1 in

the intermediate temperature region. Figure 1.11 shows the temperature dependence of $f_{j,\tau}$ for several relevant cases. In the low-temperature limit the correction factors $f_{j,\tau}$ are 1, and they initially rise above 1 as temperature increases. Eventually the correction factors achieve a relative maximum and then subsequently monotonically decrease. This behavior is quite different from that predicted by the switching functions advocated in earlier work.[7]

The three sets of $M_{j,\tau}$ values (or equivalently the domain volumes) for 1-pentyl radical all have larger volumes (smaller $M_{j,\tau}$ values) for the first three pairs of structures in Table 1.8 than for the others, and the three sets of MS-AS partition functions have similar magnitudes. While it is difficult to judge which set of $M_{j,\tau}$ values is more accurate, this indicates that the $M_{j,\tau}$ values determined by Voronoi tessellation lead to reasonable results. The ratio of the largest to the smallest of the three sets of MS-AS partition functions at 400 K is only 1.30. It is interesting to compare the effective barrier heights calculated from the three sets of $M_{j,\tau}$ values. The radical – CH_2 group rotation barrier is around 250 cm^{-1} for the global minimum P–a$^-$g$^+$t obtained by a relaxed scan. The effective barrier heights calculated by M = 2.67 (254 cm^{-1}) and M = 2.53 (281 cm^{-1}) have better agreement with the barrier height obtained by a relaxed scan than that calculated by M = 2 (451 cm^{-1}). However, for the structure P–stt, the effective barrier height obtained by a relaxed scan (around 30–40 cm^{-1}) is much lower than that calculated with M = 3.39 (100 cm^{-1}) and M = 3.56 (90 cm^{-1}), but it agrees very well with the barrier height calculated with M = 6 (32 cm^{-1}). Despite these differences between the effective barrier heights calculated by the three different

sets of $M_{j,\tau}$ values, all of the calculated effective barrier heights fall into reasonable ranges for all the torsions considered here. The three sets of MS-AS partition functions of 1-pentyl radical have the same high–*T* limit because the torsional partition function is independent of the $M_{j,\tau}$ values in the high–*T* limit as long as eqn (30) is satisfied.

For 1-butanol the 27-structures partition functions and 29-structures partition functions have differences of less than 3% because the two addtitional structures have high energies and small subdomain volumes. This result shows that missing some structures with high energies need not lead to large errors in applying the MS-AS method.

For 1-butanol, the MS-AS partition functions and MS-RS partition functions agree with each other within about 3% for 600 K and above, but the deviation rises to 6% and 8% at 300 K and 200 K, respectively. For the 1-pentyl radical, the deviations between the MS-AS and MS-RS partition functions are larger than those for 1-butanol but are still within 10% for temperatures above 200 K when both are calculated with integer $M_{j,\tau}$. The differences between the 1-pentyl MS-RS and MS-AS partition functions when one uses the $M_{j,\tau}$ schemes designed for strong coupling are larger. With the (2:2) and (1:3) schemes, the ratios of the MS-AS to the MS-RS partition functions are 1.33 – 1.41 from 400 K to 600 K. The deviations are a consequence of the MS-RS scheme being designed as an affordable approximation to the nearly separable MS-AS method. The levels of agreement and disagreement between the results of the methods confirm the principle behind design of the reference-structure method.

Because the MS-ASCB method uses the most information about the potential energy surface, it is expected—in the absence of cancellation of errors—to be the most

accurate of the methods presented here. The good agreement observed between the results of the MS-AS and MS-ASCB methods suggests that the simpler MS-AS method is capable of providing reliable results. Finally, the comparable accuracy and reduced cost of the MS-RS method make it particularly well suited for accounting for the torsional anharmonicity of systems with a large numbers of torsions.

5. Conclusion

In this article, we proposed a new family of approximations called multi-structural methods for including torsional anharmonicity in thermodynamics calculations. These methods can be applied to molecules with multiple torsions coupled with each other or with other low-frequency vibrational modes. A key feature of the methods is the use of internal coordinates to correct for torsional anharmonicity so that assigning a torsion to a specific normal mode is not required in the multi-structural methods. These methods only require geometry optimizations and frequency calculations (i.e., no scans) and are easily implemented. The MS-AS method is designed to be as accurate as possible without requiring any information about the conformational barriers or the paths connecting the structures. We recommend the MS-AS method based on its good balance between computational cost, simplicity, and accuracy. The simpler MS-RS method, which is an approximation to the MS-AS method for the cases of nearly separable torsions, is also found to perform well in our tests and is recommended for large systems when the cost and effort of the MS-AS method are not affordable or not justified.

Table 1.1 Normal-mode frequencies (cm^{-1}) calculated by M06-2X/6-311+G(2df,2p) accompanied various integration grids

Grids					
	Ethanol (structure: E–t), 3 lowest frequencies				
Ultrafine[a]	224	269	423		
(99,590)[b]	224	268	423		
(99,770)[b]	247	292	423		
(99,974)[b]	238	278	422		
(96,32,64)[c]	236	275	423		
	1-Pentyl radical (structure: P–stt), 5 lowest frequencies				
Ultrafine[a]	53*i*	84	126	225	287
(99,590)[b]	75	85	127	225	287
(99,770)[b]	64	85	128	228	287
(99,974)[b]	76	87	129	228	287
(120,974)[b]	75	87	129	228	287
(150,974)[b]	75	87	129	229	287
(96,32,64)[c]	71	87	128	228	287

[a] Ultrafine denotes the pruned (99,590) grid provided in the *Gaussian09* package.

[b] The first number indicates the number of radial quadrature nodes, and the second denotes the number of Lebedev angular quadrature nodes.

[c] A spherical product grid with the first number specifying the number of radial quadrature nodes and the next two specifying the numbers of angular quadrature nodes

Table 1.2 Notation for torsion angles[a]

	Abbreviation	dihedral angle range (deg)
antiperiplanar	a^+	[140, 163]
	a^-	[−163, −140]
gauche for 1-pentyl	g^+	[55, 80]
	g^-	[−80, −55]
or		
gauche for 1-butanol	g^+	[57, 76]
	g^-	[−76, −57]
cross for 1-butanol only	x^+	[80, 90]
	x^-	[-90, -80]
syn for 1-pentyl only	s	[80, 100] or [−100, −80]
trans	t	[−173, −180] and [180, 173]

[a]The dihedral angles used for torsions are H–O–$C^{(1)}$–$C^{(2)}$, O–$C^{(1)}$–$C^{(2)}$–$C^{(3)}$, and $C^{(1)}$–$C^{(2)}$–$C^{(3)}$–$C^{(4)}$ for 1-butanol, H–$C^{(1)}$–$C^{(2)}$–$C^{(3)}$, $C^{(1)}$–$C^{(2)}$–$C^{(3)}$–$C^{(4)}$, and $C^{(2)}$–$C^{(3)}$–$C^{(4)}$–$C^{(5)}$ for 1-pentyl, and H–O–C–C and O–C–C–H for ethanol.

Table 1.3 Calculated partition functions and their percentage errors compared to TES values for the 1-D model potential of eqn (48)

T (K)	MS-HO		MS-AS		MS-ASCB		TES
	q	% error	q	% error	q	% error	q
60	0.4776	−17	0.5247	−9	0.5356	−7	0.5751
100	1.083	−14	1.236	−2	1.229	−3	1.266
150	1.935	−10	2.174	1	2.132	−1	2.159
200	2.863	−5	3.078	2	3.006	−1	3.025
300	4.848	5	4.703	2	4.596	−0	4.600
400	6.922	16	6.106	2	5.983	0	5.979
600	11.18	35	8.447	2	8.315	0	8.303
1000	19.87	67	12.06	1	11.93	0	11.92
1500	30.83	100	15.55	1	15.44	0	15.42
2000	41.82	128	18.43	1	18.33	0	18.31
2400	50.62	149	20.46	1	20.36	0	20.34
3000	63.83	177	23.17	0	23.08	0	23.07
4000	85.87	218	27.11	0	27.03	0	27.02
7000	152.0	318	36.48	0	36.42	0	36.41
50000	1100	1007	99.43	0	99.40	0	99.40

Table 1.4 Percentage errors of various methods compared to TES values for the torsion potential of eqn (48) when the shallow minimum on the model potential is ignored

T (K)	MS-HO	MS-AS
60	–20	–17
100	–24	–19
150	–28	–20
200	–30	–20
300	–29	–17
400	–27	–15
600	–21	–11
1000	–8	–7
1500	7	–5
2000	20	–4
2400	30	–3
3000	43	–3
4000	63	–2
7000	111	–1
50000	453	–0

Table 1.5 Calculated partition functions and their percentage errors compared to TES values for the 1-D model potential of H_2O_2

T (K)	MS-HO		MS-AS		MS-ASCB		TES
	q	% error	q	% error	q	% error	q
60	0.02036	–34	0.02061	–33	0.01999	–35	0.03071
100	0.1281	–23	0.1308	–21	0.1281	–23	0.1654
150	0.3276	–18	0.3386	–15	0.3364	–16	0.3990
200	0.5395	–16	0.5656	–12	0.5655	–12	0.6442
300	0.9509	–15	1.03	–8	1.018	–9	1.116
400	1.345	–14	1.501	–3	1.443	–7	1.555
600	2.105	–11	2.443	4	2.223	–6	2.359
1000	3.588	–5	4.199	11	3.616	–5	3.787
1500	5.419	1	6.089	13	5.187	–4	5.383
2000	7.244	6	7.707	13	6.621	–3	6.827
2400	8.701	10	8.856	12	7.684	–3	7.893
3000	10.88	16	10.4	11	9.158	–2	9.366
4000	14.52	26	12.63	9	11.35	–2	11.56
7000	25.43	51	17.86	6	16.65	–1	16.83
50000	181.7	255	51.67	1	51.08	–0	51.17

Table 1.6 Information used for the ethanol partition function calculations using the MS-AS and MS-ASCB methods[a]

Torsion	$\overline{\omega}$	W^b	W^{L}	W^{R}	I	M	P
Structure E–t ($U_1 = 0$)							
C–O	258.7	328.9	385.7	385.7	0.7456	3	3
C–C	253.9	1108.6	1108.7	1108.7	2.610	3	1
Structure E–g$^+$ & E–g$^-$ ($U_2 = U_3 = 27.4$ cm^{-1})							
C–O	278.5	379.0	358.6	372.0	0.7416	3	3
C–C	264.5	1206.2	1194.9	1194.9	2.616	3	1

[a] The units are cm^{-1} for the barrier heights and frequencies and amu Å^2 for the internal moments of inertia.

[b] W is used in the MS-AS method and is calculated by eqn (13).

Table 1.7 Calculated conformational-rovibrational partition function of ethanol using multi-structural methods

T (K)	MS-HO	MS-AS	MS-ASCB
100	4.12E-104	4.47E-104	4.37E-104
150	5.45E-68	6.21E-68	6.08E-68
200	8.13E-50	9.64E-50	9.46E-50
300	1.95E-31	2.43E-31	2.39E-31
400	4.77E-22	6.06E-22	6.00E-22
600	2.94E-12	3.73E-12	3.70E-12
1000	1.62E-03	1.90E-03	1.89E-03
1500	3.60E+02	3.65E+02	3.65E+02
2000	7.76E+05	6.84E+05	6.83E+05
2400	7.65E+07	6.06E+07	6.06E+07
3000	1.74E+10	1.19E+10	1.19E+10
4000	1.56E+13	8.67E+12	8.67E+12
7000	6.07E+18	2.15E+18	2.15E+18
50000	1.13E+38	6.34E+36	6.34E+36

Table 1.8 Information used for the 1-pentyl radical partition function using the multi-structural method[a]

Torsion	$\overline{\omega}$	I	W^b	M	P	W^b	M	P	W^b	M	P
			NS:SC=2:2			NS:SC=1:3			NS:SC=4:0		
Structure P–a$^-$g$^+$t & P–a$^+$g$^-$t (U = 0)											
C$^{(1)}$–C$^{(2)}$	133	1.714	281	2.53	1.27	254	2.67	1.33	451	2	1
C$^{(2)}$–C$^{(3)}$	142	10.91	2047	2.53	2.53	1846	2.67	2.67	1458	3	3
C$^{(3)}$–C$^{(4)}$	99	15.98	1040	3	3	1316	2.67	2.67	1040	3	3
C$^{(4)}$–C$^{(5)}$	228	2.917	998	3	1	998	3	1	998	3	1
Structure P–a$^-$g$^+$g$^+$ & P–a$^+$g$^-$g$^-$ (U = 27.0 cm^{-1})											
C(1)–C(2)	161	1.713	426	2.48	1.24	380	2.63	1.31	654	2	1
C(2)–C(3)	131	17.09	2819	2.48	2.48	2512	2.63	2.63	1924	3	3
C(3)–C(4)	108	18.38	1418	3	3	1852	2.63	2.63	1418	3	3
C(4)–C(5)	247	3.054	1228	3	1	1228	3	1	1228	3	1
Structure P-a$^-$g$^+$g$^-$ & P–a$^+$g$^-$g$^+$ (U = 349.4 cm^{-1})											
C(1)–C(2)	157	1.713	382	2.56	1.28	336	2.73	1.36	625	2	1
C(2)–C(3)	132	15.88	2521	2.56	2.56	2216	2.73	2.73	1831	3	3
C(3)–C(4)	110	14.79	1188	3	3	1437	2.73	2.73	1188	3	3
C(4)–C(5)	254	3.057	1297	3	1	1297	3	1	1297	3	1
Structure P–a$^+$tg$^+$ & P–a$^-$tg$^-$ (U = 229.8 cm^{-1})											
C(1)–C(2)	126	1.670	81	4.40	2.20	107	3.84	1.92	44	6	3
C(2)–C(3)	110	14.45	533	4.40	4.40	698	3.84	3.84	1146	3	3
C(3)–C(4)	125	11.48	1177	3	3	717	3.84	3.84	1177	3	3
C(4)–C(5)	229	3.039	1049	3	1	1048	3	1	1049	3	1

Structure P–a^{+}tt & P–a^{-}tt (U = 73.8 cm^{-1})											
C(1)–C(2)	118	1.661	76	4.28	2.14	94	3.82	1.91	38	6	3
C(2)–C(3)	119	11.40	523	4.28	4.28	655	3.82	3.82	1063	3	3
C(3)–C(4)	117	11.91	1079	3	3	664	3.82	3.82	1079	3	3
C(4)–C(5)	227	2.871	976	3	1	976	3	1	976	3	1
Structure P–a^{+}tg^{-} & P–a^{-}tg^{+} (U = 257.4 cm^{-1})											
C(1)–C(2)	109	1.668	64	4.30	2.15	81	3.82	1.91	33	6	3
C(2)–C(3)	107	14.518	536	4.30	4.30	679	3.82	3.82	1098	3	3
C(3)–C(4)	123	11.34	1135	3	3	701	3.82	3.82	1135	3	3
C(4)–C(5)	228	3.040	1041	3	1	1041	3	1	1041	3	1
Structure P–stg^{+} & P–stg^{-} (U = 294.9 cm^{-1})											
C(1)–C(2)	103	1.670	82	3.57	1.79	92	3.36	1.68	29	6	3
C(2)–C(3)	109	15.34	845	3.57	3.57	954	3.36	3.36	1196	3	3
C(3)–C(4)	124	11.53	1161	3	3	925	3.36	3.36	1161	3	3
C(4)–C(5)	229	3.039	1051	3	1	1051	3	1	1051	3	1
Structure P–stt (U = 124.6 cm^{-1})											
C(1)–C(2)	108	1.650	90	3.56	1.78	100	3.39	1.69	32	6	3
C(2)–C(3)	121	11.88	816	3.56	3.56	901	3.39	3.39	1150	3	3
C(3)–C(4)	116	11.96	1068	3	3	837	3.39	3.39	1068	3	3
C(4)–C(5)	232	2.878	1024	3	1	1024	3	1	1024	3	1

---

^{a}The units are cm^{-1} for barrier heights and frequencies and amu Å^{2} for internal moments of inertia.

^{b} W is used in the MS-AS method and is calculated by eqn (13).

Table 1.9 Calculated conformational-rovibrational partition function of 1-pentyl radical using multi-structural methods

T (K)	MS-HO	MS-AS			MS-RS
		$2{:}2^a$	$1{:}3^a$	$4{:}0^a$	
100	5.11E-190	6.02E-190	6.10E-190	5.53E-190	6.32E-190
150	1.83E-124	2.22E-124	2.27E-124	1.93E-124	2.09E-124
200	2.04E-91	2.50E-91	2.59E-91	2.11E-91	2.16E-91
300	6.69E-58	8.22E-58	8.61E-58	6.72E-58	6.45E-58
400	1.05E-40	1.28E-40	1.35E-40	1.04E-40	9.66E-41
600	1.14E-22	1.34E-22	1.42E-22	1.12E-22	1.01E-22
1000	2.20E-06	2.21E-06	2.31E-06	1.97E-06	1.78E-06
1500	2.74E+04	2.13E+04	2.20E+04	1.99E+04	1.82E+04
2000	6.18E+10	3.71E+10	3.81E+10	3.56E+10	3.29E+10
2400	4.06E+14	2.01E+14	2.05E+14	1.95E+14	1.82E+14
3000	1.37E+19	5.17E+18	5.27E+18	5.07E+18	4.78E+18
4000	6.57E+24	1.69E+24	1.71E+24	1.67E+24	1.59E+24
7000	4.08E+35	4.37E+34	4.40E+34	4.35E+34	4.22E+34
50000	7.38E+72	1.98E+70	1.98E+70	1.97E+70	1.96E+70

^{a}NS:SC

Table 1.10 Information used for the 1-butanol conformational-rovibrational partition function using multi-structural methods[a]

Torsion	$\overline{\omega}$	I	W^b	M	P	W^b	M	P
			NS:SC=1:3			27-structures, NS:SC=4:0		
Structure B–ttt (U = 16.6 cm^{-1})								
$O^{(1)}$–$C^{(1)}$	244	0.763	281	3.10	3.10	300	3	3
$C^{(1)}$–$C^{(2)}$	122	10.800	989	3.10	3.10	1057	3	3
$C^{(2)}$–$C^{(3)}$	112	11.391	881	3.10	3.10	942	3	3
$C^{(4)}$–$C^{(5)}$	231	2.832	995	3	1	995	3	1
Structure B–ttg$^+$ & B–ttg$^-$ (U = 329.5 cm^{-1})								
$O^{(1)}$–$C^{(1)}$	250	0.755	307	3.02	3.02	310	3	3
$C^{(1)}$–$C^{(2)}$	107	13.624	1012	3.02	3.02	1023	3	3
$C^{(2)}$–$C^{(3)}$	119	10.829	1000	3.02	3.02	1010	3	3
$C^{(4)}$–$C^{(5)}$	218	3.001	944	3	1	944	3	1
Structure B–tg$^+$t & B–tg$^-$t (U = 0.0 cm^{-1})								
$O^{(1)}$–$C^{(1)}$	243	0.759	273	3.12	3.12	296	3	3
$C^{(1)}$–$C^{(2)}$	143	10.368	1284	3.12	3.12	1391	3	3
$C^{(2)}$–$C^{(3)}$	98	15.608	914	3.12	3.12	990	3	3
$C^{(4)}$–$C^{(5)}$	229	2.879	994	3	1	994	3	3
Structure B–tg$^+$g$^+$ & B–tg$^-$g$^-$ (U = 229.9 cm^{-1})								
$O^{(1)}$–$C^{(1)}$	247	0.766	320	2.94	2.94	308	3	3
$C^{(1)}$–$C^{(2)}$	114	16.178	1433	2.94	2.94	1378	3	3
$C^{(2)}$–$C^{(3)}$	91	17.732	1008	2.94	2.94	970	3	3
$C^{(4)}$–$C^{(5)}$	220	3.007	960	3	1	960	3	1

Structure B–tg^{+}g^{-} & B–tg^{-}g^{+} (U = 605.4cm^{-1})								
O$^{(1)}$–C$^{(1)}$	259	0.757	326	3.04	3.04	335	3	3
C$^{(1)}$–C$^{(2)}$	124	13.514	1345	3.04	3.04	1379	3	3
C$^{(2)}$–C$^{(3)}$	105	15.789	1116	3.04	3.04	1145	3	3
C$^{(4)}$–C$^{(5)}$	223	3.030	989	3	1	989	3	1
Structure B–g^{+}tt & B–g^{-}tt (U = 16.1cm^{-1})								
O$^{(1)}$–C$^{(1)}$	261	0.757	320	3.09	3.09	340	3	3
C$^{(1)}$–C$^{(2)}$	128	10.938	1105	3.09	3.09	1176	3	3
C$^{(2)}$–C$^{(3)}$	112	11.538	889	3.09	3.09	946	3	3
C$^{(4)}$–C$^{(5)}$	231	2.833	1000	3	1	1000	3	1
Structure B–g^{+}tg^{+} & B–g^{-}tg^{-} (U = 359.0 cm^{-1})								
O$^{(1)}$–C$^{(1)}$	252	0.760	301	3.08	3.08	318	3	3
C$^{(1)}$–C$^{(2)}$	110	13.915	1040	3.08	3.08	1100	3	3
C$^{(2)}$–C$^{(3)}$	118	10.981	949	3.08	3.08	1004	3	3
C$^{(4)}$–C$^{(5)}$	217	3.001	933	3	1	933	3	1
Structure B–g^{+}tg^{-} & B–g^{-}tg^{+} (U = 314.4 cm^{-1})								
O$^{(1)}$–C$^{(1)}$	265	0.770	356	3.00	3.00	357	3	3
C$^{(1)}$–C$^{(2)}$	112	13.886	1146	3.00	3.00	1149	3	3
C$^{(2)}$–C$^{(3)}$	119	11.012	1019	3.00	3.00	1022	3	3
C$^{(4)}$–C$^{(5)}$	217	3.003	934	3	1	934	3	1
Structure B–g^{+}g^{+}t & B–g^{-}g^{-}t (U = 40.6 cm^{-1})								
O$^{(1)}$–C$^{(1)}$	261	0.786	345	3.03	3.03	354	3	3
C$^{(1)}$–C$^{(2)}$	146	10.378	1415	3.03	3.03	1448	3	3
C$^{(2)}$–C$^{(3)}$	96	15.648	924	3.03	3.03	946	3	3
C$^{(4)}$–C$^{(5)}$	230	2.882	1000	3	1	1000	3	1

Structure B–$g^+g^+g^+$ & B-$g^-g^-g^-$ (U = 251.2 cm^{-1})								
$O^{(1)}$–$C^{(1)}$	264	0.783	382	2.91	2.91	359	3	3
$C^{(1)}$–$C^{(2)}$	114	16.244	1471	2.91	2.91	1381	3	3
$C^{(2)}$–$C^{(3)}$	89	17.861	991	2.91	2.91	930	3	3
$C^{(4)}$–$C^{(5)}$	220	3.008	961	3	1	961	3	1
Structure B–$g^+g^+g^-$ & B-$g^-g^-g^+$ (U = 598.4 cm^{-1})								
$O^{(1)}$–$C^{(1)}$	259	0.790	355	3.00	3.00	349	3	3
$C^{(1)}$–$C^{(2)}$	128	13.858	1514	3.00	3.00	1491	3	3
$C^{(2)}$–$C^{(3)}$	105	15.615	1154	3.00	3.00	1136	3	3
$C^{(4)}$–$C^{(5)}$	236	3.031	1113	3	1	1113	3	1
Structure B–$g^+x^-g^+$ & B-$g^-x^+g^-$ (U = 770.4 cm^{-1})								
$O^{(1)}$–$C^{(1)}$	260	0.770	272	3.37	3.37	343	3	3
$C^{(1)}$–$C^{(2)}$	149	15.428	1785	3.37	3.37	2253	3	3
$C^{(2)}$–$C^{(3)}$	112	13.917	904	3.37	3.37	1141	3	3
$C^{(4)}$–$C^{(5)}$	284	3.021	1603	3	1	1603	3	1
Structure B–g^+g^-t & B–g^-g^+t (U = 70.6 cm^{-1})								
$O^{(1)}$–$C^{(1)}$	254	0.767	301	3.12	3.12	326	3	3
$C^{(1)}$–$C^{(2)}$	140	10.435	1253	3.12	3.12	1355	3	3
$C^{(2)}$–$C^{(3)}$	101	15.489	966	3.12	3.12	1045	3	3
$C^{(4)}$–$C^{(5)}$	230	2.876	999	3	1	999	3	1
Structure B–$g^+g^-g^-$ & B–$g^-g^+g^+$ (U = 343.7 cm^{-1})								
$O^{(1)}$–$C^{(1)}$	237	0.766	293	2.96	2.96	285	3	3
$C^{(1)}$–$C^{(2)}$	112	16.267	1379	2.96	2.96	1342	3	3
$C^{(2)}$–$C^{(3)}$	95	17.744	1094	2.96	2.96	1065	3	3
$C^{(4)}$–$C^{(5)}$	219	3.006	947	3	1	947	3	1

Structure B–g^{+}g^{-}x^{+} & B–g^{-}g^{+}x^{-} (U = 911.5 cm^{-1})

O$^{(1)}$–C$^{(1)}$	272	0.783	271	3.55	3.55
C$^{(1)}$–C$^{(2)}$	115	12.330	761	3.55	3.55
C$^{(2)}$–C$^{(3)}$	117	17.289	1110	3.55	3.55
C$^{(4)}$–C$^{(5)}$	202	3.012	810	3	1

---

[a] The units are cm^{-1} for barrier heights and frequencies and amu Å^{2} for internal moments of inertia.

[b] W is used in the MS-AS method and is calculated by eqn (13).

Table 1.11 Calculated conformational-rovibrational partition function of 1-butanol using multi-structural methods

	MS-HO	MS-AS		MS-RS[a]
		NS:SC=4:0[b]	NS:SC=1:3	
T (K)				
100	1.09E-179	1.24E-179	1.25E-179	1.10E-179
150	1.28E-117	1.57E-117	1.58E-117	1.43E-117
200	2.44E-86	3.17E-86	3.20E-86	2.95E-86
300	1.25E-54	1.79E-54	1.80E-54	1.69E-54
400	2.24E-38	3.44E-38	3.48E-38	3.31E-38
600	2.39E-21	3.91E-21	3.98E-21	3.85E-21
1000	5.18E-06	7.99E-06	8.20E-06	8.12E-06
1500	1.55E+04	1.94E+04	1.99E+04	2.01E+04
2000	1.38E+10	1.35E+10	1.39E+10	1.41E+10
2400	5.11E+13	4.15E+13	4.27E+13	4.35E+13
3000	8.66E+17	5.39E+17	5.53E+17	5.65E+17
4000	1.74E+23	7.32E+22	7.49E+22	7.68E+22
7000	2.01E+33	3.49E+32	3.55E+32	3.65E+32
50000	1.00E+68	4.29E+65	4.31E+65	4.42E+65

[a]The reference structure is taken as B–tg$^+$t.

[b]Using only 27 structures, see text for further details.

Table 1.12 Standard state entropy (in cal mol^{-1} K^{-1}) calculated using SS-HO, MS-HO, and MS-AS partition functions and group additivity method[a]

T (K)	SS-HO	MS-HO	MS-AS	GA	Ref. data
ethanol					
298.15	64.79	66.85	67.47	67.10	67.31[b]
400	69.96	72.02	72.59	72.17	
600	79.26	81.33	81.68	81.16	
1000	94.99	97.06	96.85	96.28	
1-butanol					
298.15	80.04	85.97	87.17[c]	85.94	86.8[d]
400	88.54	94.78	96.07[c]	94.65	
600	104.25	110.77	111.86[c]	110.22	
1000	131.29	138.00	138.14[c]	136.48	
1-pentyl radical					
298.15	83.75	89.08	89.48[e]	86.32	
				88.48[f]	
				88.13[g]	
400	93.04	98.54	98.87[e]	95.86	
				97.87[f]	
				97.40[g]	
600	110.09	115.71	115.71[e]	112.64	
				114.55[f]	
				114.02[g]	
1000	139.20	144.88	143.95[e]	141.08	
				143.06[f]	
				142.21[g]	
1500	167.96	173.64	171.62[e]	169.22	
				171.50[f]	

[a]The SS-HO calculations only account the contribution from the global minimum and all the vibrational modes (including torsional modes) are approximated as harmonic oscillator (*J*, Z_j, and $f_{j,\tau}$ are all equal to 1). All the calculated entropies include electronic and translational contributions. Frequencies used in the calculations are all scaled (see text for details). The calculations by GA method use the parameters in ref.[30] except those in footnote *f* and *g*.

[b]From Ref. [74]

[c]The data are calculated using NS:SC = 3:1.

[d]Experimental data from ref.[75]

[e]The data are calculated using NS:SC = 2:2.

[f]The parameters used in the calculations were taken from Cohen[33].

[g]The parameters used in the GA calculations were taken from Lay et al[34].

Table 1.13 The calculated correction factors Z^{int} and Z^{coup} for structures of ethanol, 1-butanol, and 1-pentyl radical

Structure	Z^{int}	Z^{coup}	Structure	Z^{int}	Z^{coup}
ethanol			1-butanol		
E–t	0.954	1.000	B–ttt	0.920	0.937
E–g$^+$/E–g$^-$	0.974	0.993	B–ttg$^+$/B–ttg$^-$	0.790	0.962
			B–tg$^+$t/B–tg$^-$t	0.886	0.941
1-pentyl radical			B–tg$^+$g$^+$/B–tg$^-$g$^-$	1.024	0.758
P–a$^-$g$^+$t$^-$/P–a$^+$g$^-$t$^+$	0.834	0.935	B–tg$^+$g$^-$/B–tg$^-$g$^+$	0.642	0.948
P–a$^-$g$^+$g$^+$/P–a$^+$g$^-$g$^-$	1.115	0.737	B–g$^+$tt/B–g$^-$tt	0.912	0.938
P–a$^-$g$^+$g$^-$/P–a$^+$g$^-$g$^+$	0.721	0.928	B–g$^+$tg$^+$/B–g$^-$tg$^-$	0.789	0.954
P–a$^+$g$^+$g$^+$/P–a$^-$g$^-$g$^-$	0.785	0.944	B–g$^+$tg$^-$/B–g$^-$tg$^+$	0.818	0.946
P–a$^+$tt/P–a$^-$tt	0.866	0.935	B–g$^+$g$^+$t/B–g$^-$g$^-$t	0.922	0.909
P–a$^+$tg$^-$/P–a$^-$tg$^+$	0.700	0.945	B–g$^+$g$^+$g$^+$/B–g$^-$g$^-$g$^-$	1.027	0.744
P–stg$^+$/P–stg$^-$	0.608	0.938	B–g$^+$g$^+$g$^-$/B–g$^-$g$^-$g$^+$	0.770	0.908
P–stt	0.783	0.933	B–g$^+$x$^-$g$^+$/B–g$^-$x$^+$g$^-$	0.716	0.917
			B–g$^+$g$^-$t/B–g$^-$g$^+$t	0.868	0.936
			B–g$^+$g$^-$g$^-$/B–g$^-$g$^+$g$^+$	1.020	0.759
			B- g$^+$g$^-$x$^+$/B–g$^-$g$^+$x$^-$	0.554	0.934

Table 1.14 Partition function of ethanol calculated by various approximations[a]

T (K)	CO	SRPG	RPG	TES
100	4.30E-104	5.77E-104	6.80E-104	7.03E-104
150	5.64E-68	7.79E-68	8.74E-68	8.54E-68
200	8.38E-50	1.16E-49	1.29E-49	1.25E-49
300	1.99E-31	2.77E-31	3.02E-31	2.95E-31
400	4.78E-22	6.71E-22	7.25E-22	7.13E-22
600	2.82E-12	3.96E-12	4.21E-12	4.22E-12
1000	1.40E-03	1.94E-03	2.02E-03	2.05E-03
1500	2.74E+02	3.66E+02	3.77E+02	3.84E+02
2000	5.26E+05	6.76E+05	6.93E+05	7.07E+05
2400	4.72E+07	5.97E+07	6.08E+07	6.18E+07
3000	9.56E+09	1.17E+10	1.19E+10	1.21E+10
4000	7.14E+12	8.46E+12	8.54E+12	8.67E+12
7000	1.87E+18	2.09E+18	2.09E+18	2.12E+18
50000	6.04E+36	6.14E+36	6.14E+36	6.17E+36

[a]All the frequencies in the CO, SRPG, RPG calculations are scaled by a factor λ = 0.970 for M06-2X/6-311+G(2df,2p) method,[69] and λ^2 is used to scale the 1-D potentials used in TES calculations.

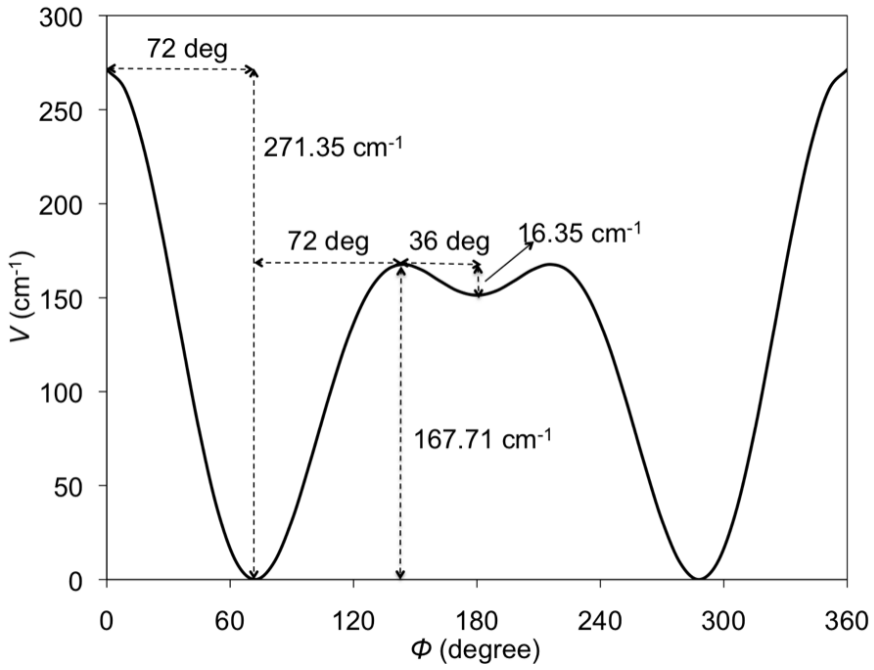

Figure 1.1 A model potential (eqn (48)) representing a torsional motion.

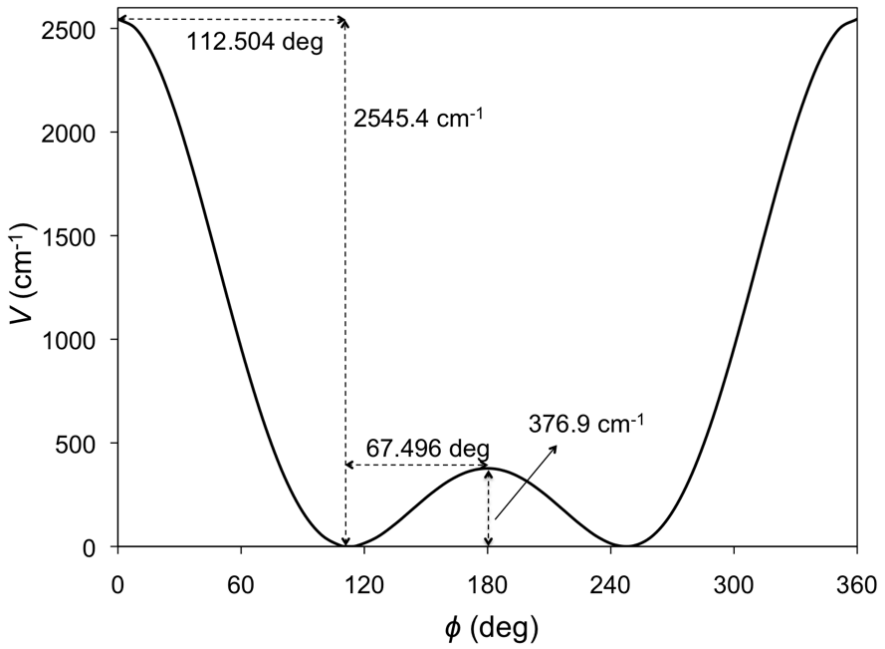

Figure 1.2 The potential energy curve (eqn (49)) of the 1-D torsional motion in H_2O_2.

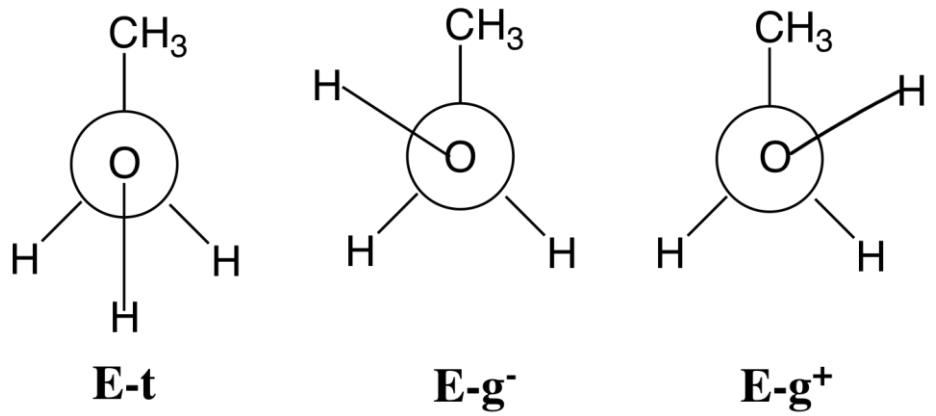

Figure 1.3 Newman projections of the three structures of ethanol. Structure E–t is the global minimum and structures E–g^- and E–g^+ are isoenergetic but distinguishable. Note that E denotes ethanol, t denotes trans, and g denotes gauche.

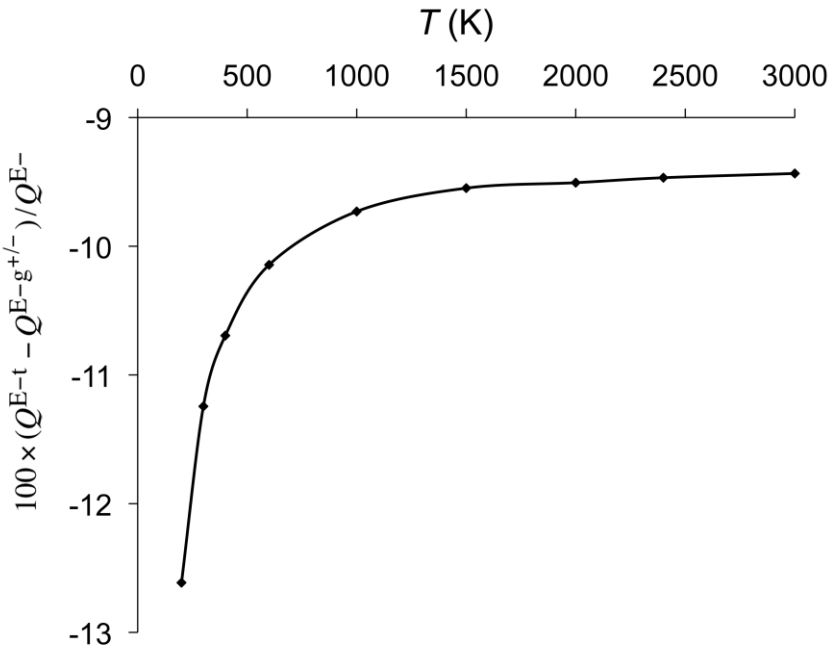

Figure 1.4 Percentage difference between partition functions of structures E–t and E–g^- (or E–g^+) using the harmonic approximation. The zero of energy is at each structure's local minimum.

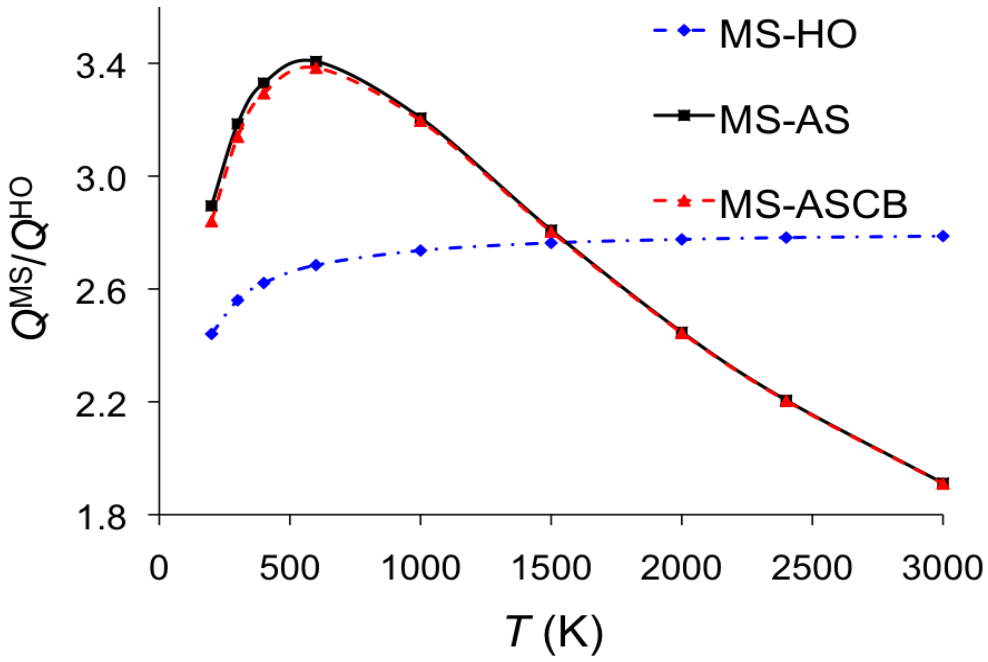

Figure 1.5 Ratio of the rovibrational partition function of ethanol calculated by multi-structural methods to that calculated by the single-structure HO approximation at the global minimum.

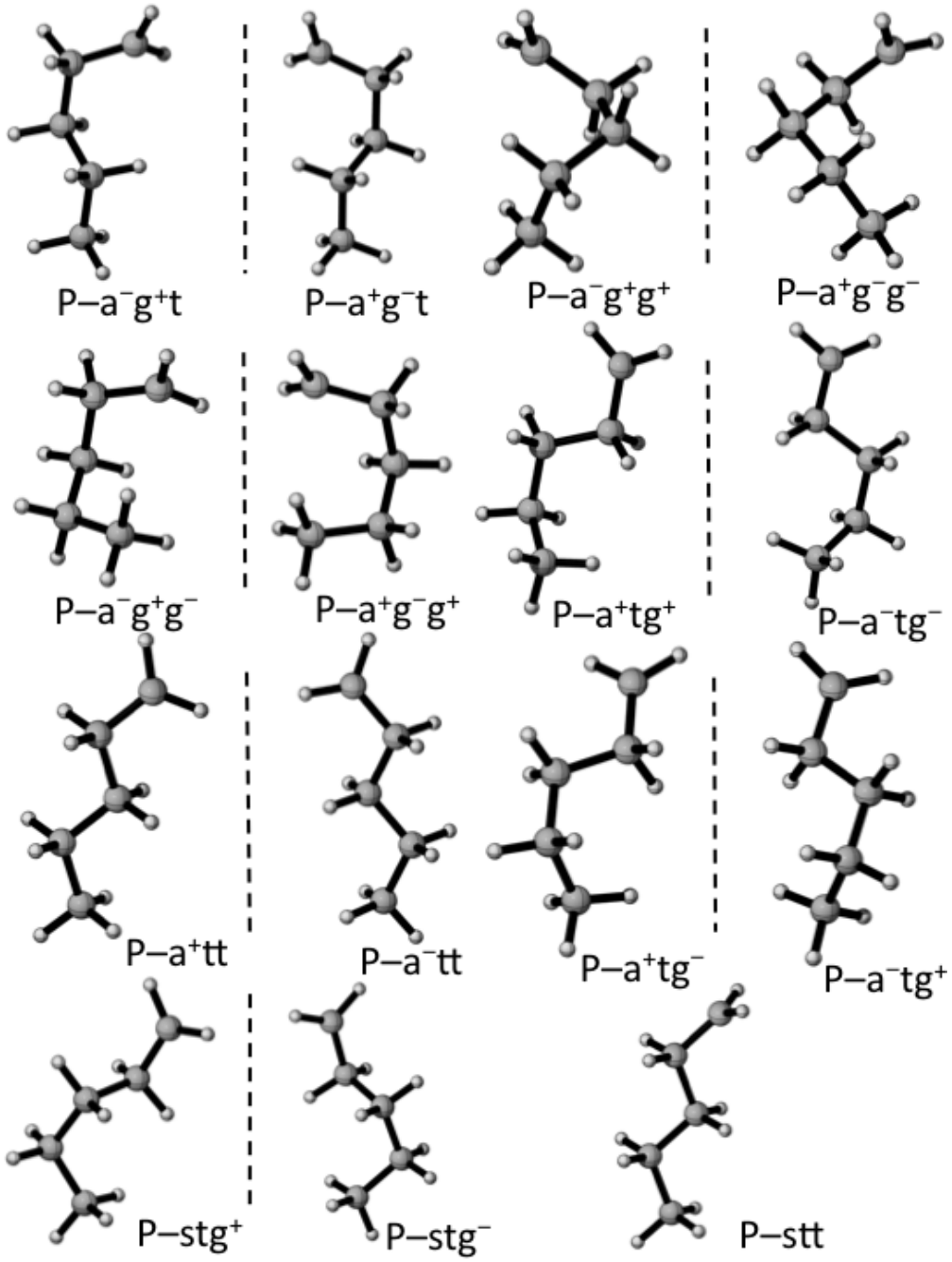

Figure 1.6 Fifteen structures of the 1-pentyl radical. Structures separated by a dashed vertical line are mirror images, e.g., P–a⁻g⁺t and P–a⁺g⁻t.

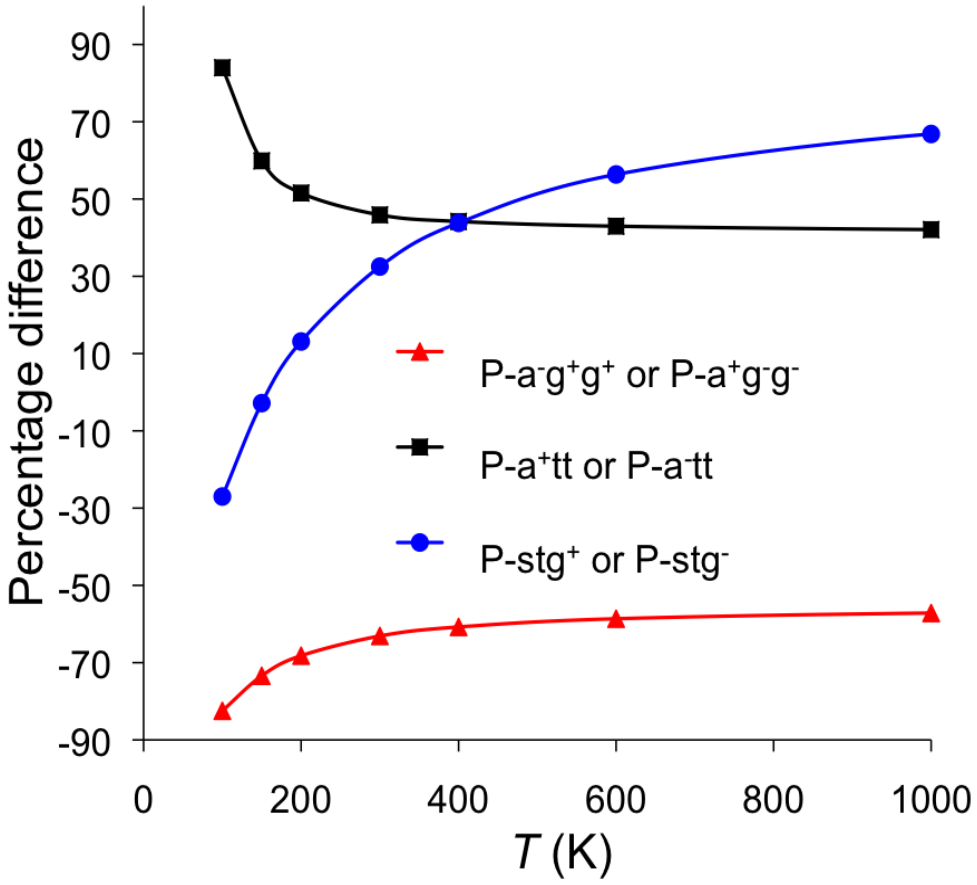

Figure 1.7 Percentage difference between harmonic oscillator partition functions of the global minimum structure and selected other structures of the 1-pentyl radical. The zero of energy is at each structure's local minimum. The three cases with the largest difference are presented in this figure.

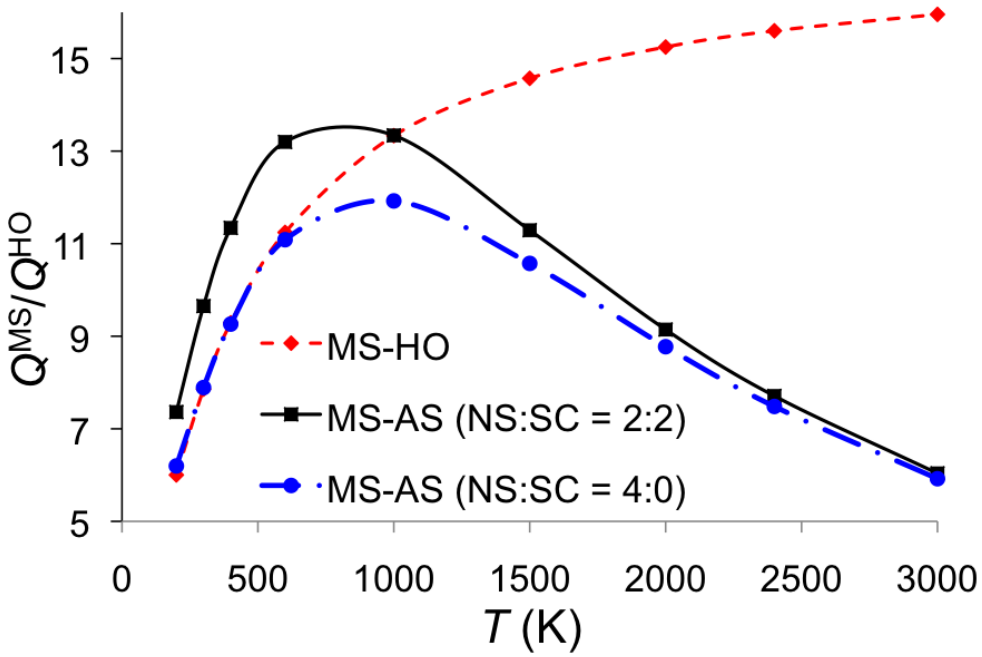

Figure 1.8 Ratio of the partition function of the 1-pentyl radical calculated by multi-structural methods to that calculated by the single-structure HO approximation using the global minimum structure.

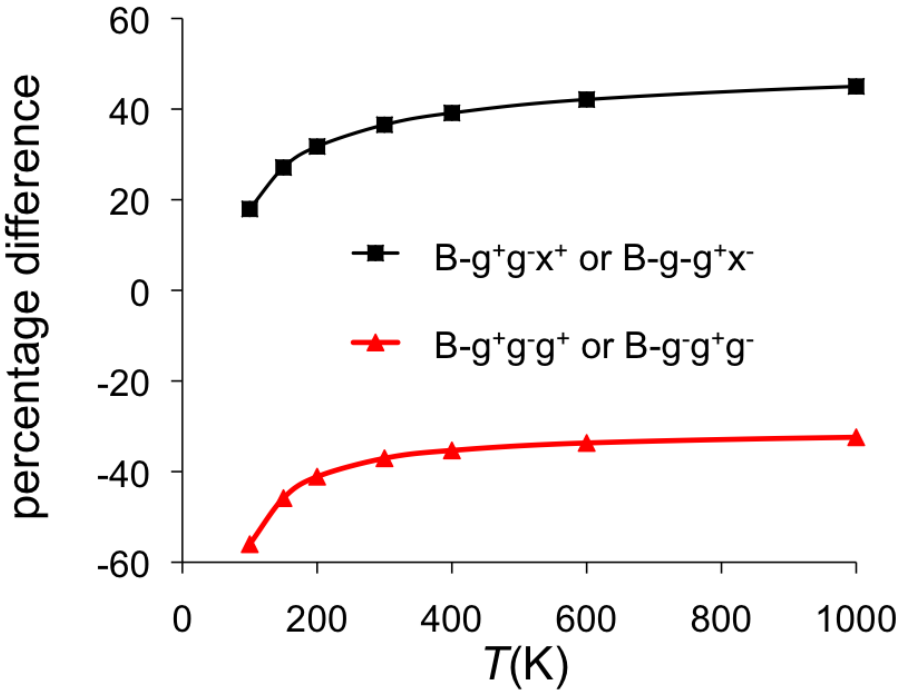

Figure 1.9 Percentage difference between harmonic oscillator partition functions of selected 1- butanol structures and the harmonic oscillator partition functions of the global minimum. The zero of energy is at each structure's local minimum. The two cases with the largest differences are presented in this figure.

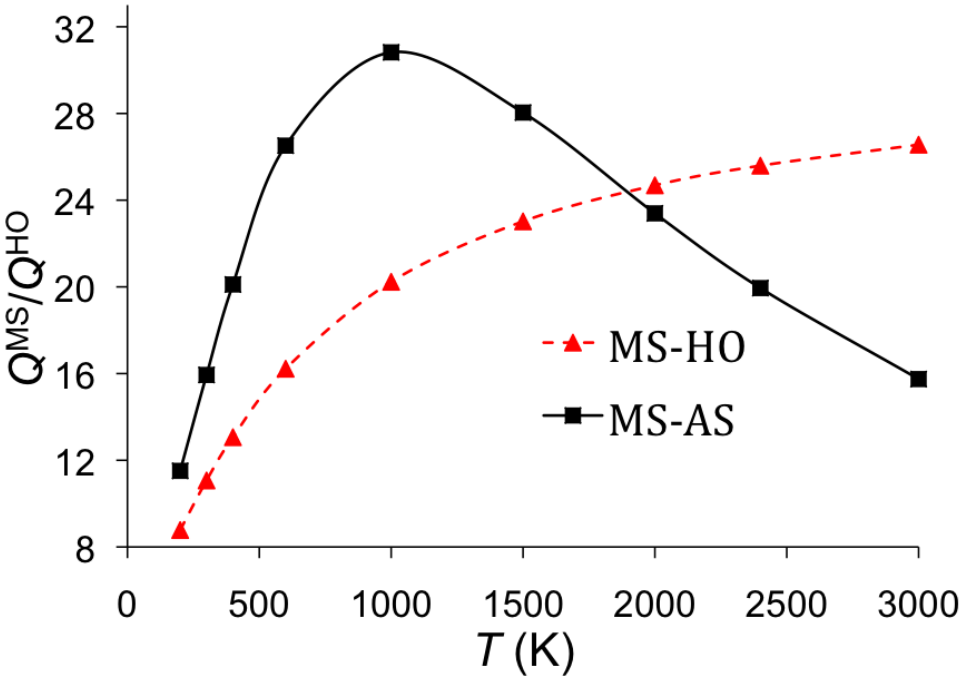

Figure 1.10 Ratio of the partition function of 1-butanol calculated by multi-structural methods with NS:SC=1:3 to that calculated by the single-structure HO approximation at the global minimum.

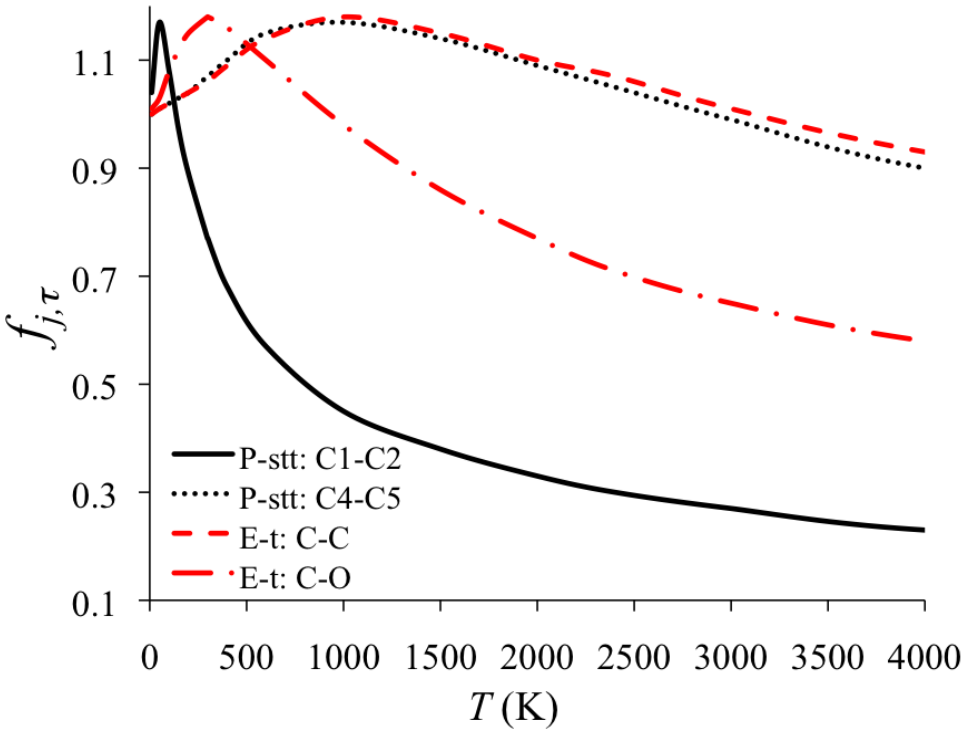

Figure 1.11 Temperature dependence for the $f_{j,\tau}$ for several relevant cases.

Chapter 2. Statistical thermodynamics of the isomerization reaction between *n*-heptane and isoheptane

1. Introduction

The thermodynamic properties of molecules are important in almost all branches of chemistry and chemical engineering. Thermodynamic data (or, for transition states, quasi-thermodynamic data), such as entropy, enthalpy, and Gibbs free energy, are required to calculate heats of reaction, chemical equilibrium constants, and thermal reaction rate constants. This kind of data can be determined by either experimental measurements or statistical mechanical computations. The example to be considered here is the determination of the thermodynamic properties of alkanes; such data are needed for, among other uses, understanding combustion and pyrolysis mechanisms.

Thermodynamic properties of alkanes in the gas phase can be obtained by three approaches, namely (i) direct experimental measurements, (ii) empirical estimations based on experiments on related systems, possibly combined with experiments on the same system under different conditions, and (iii) electronic structure calculations combined with statistical mechanics. In approaches (i) and (ii) one can distinguish approaches involving direct measurements of thermodynamic properties such as heats of reaction and heat capacities (methods of type i-a and ii-a) and approaches based on measurement of spectroscopic properties from which thermodynamic variables may be inferred by statistical mechanics (methods of type i-b and ii-b); thermodynamic tables are often constructed using a combination of methods of all four types. Many measurements of the thermodynamic properties of C_3−to−C_8 hydrocarbons were carried

out by Pitzer,[82,83] Finke,[84-87] Scott,[88] Rossini,[89] and Huffman[90-93] prior to 1970. Building on this data, Benson[31,94-96] developed empirical group additivity tables that became popular for estimating the thermodynamic properties of alkanes at various temperatures. A variety of statistical mechanical approximations[7,13,14,21,22,25] have been used to estimate partition functions for *n*-butane, *n*-pentane, and other larger alkanes.[17]

The new results in the present paper are based on the nonempirical approach iii. We can distinguish two kinds of anharmonicity in alkane molecules that make it challenging to calculate the partition functions without using empirical data:[97-99] (1) Multiple-structure anharmonicity is caused by the multiple minima of the potential energy surface that are encountered when one carries out internal rotation of the C−C bonds; in particular, the internal rotations generate many conformers of the alkane molecules, and the number becomes very large for longer alkanes. Even if high barriers separated these conformers, and even if the accessible configurations were locally harmonic, the existence of more than one minimum is a manifestation of the fact the potential energy surface is not globally quadratic, as required for the validity of the global harmonic approximation. (2) The torsional character of certain vibrations makes even the local application of the quadratic approximation quantitatively inaccurate, especially in the intermediate- and high-temperature range. Although hindered-rotor approximations[7,13,14,21,22,25] using normal-mode-substitution models and mixed torsional Pitzer–Gwinn methods[21] are available for statistical mechanical treatments of anharmonic molecules, it is still challenging to include multiple-structure anharmonicity and torsional anharmonicity when the torsions are not separable from each other and from other degrees of freedom. In addition, the internal rotation could couple with the

overall rotation of the molecules; Wong and Raman addressed this issue in the study of the thermodynamic properties of 1,3-butadiene[100] and 1,2-dihaloethane[101] using an internal coordinate path Hamiltonian formalism.[102]

Recently, we provided a new method, called the internal-coordinate multi-structural (MS) approximation[97] to calculate the partition functions of complex molecules that contain several torsional modes and applied it to study the kinetics and thermodynamics of large molecules.[98,99] This new method provides a practical approach to compute the partition functions of large molecules including both multiple-structure anharmonicity and torsional anharmonicity. The MS method with torsional anharmonicity (MS-T) includes both effects, and it reduces to the multi-structural local harmonic (MS-LH) approximation in the low-temperature limit, where only the multiple-structure anharmonicity effect is important; but it reaches the correct free-rotor result in the high-temperature limit, thereby including the torsional anharmonicity effect.

In the present work, we studied the thermal entropies, enthalpies, and free energies of the isomerization reaction between two alkanes: *n*-heptane and isoheptane. The *n*-heptane molecule contains six torsions, and four of them can generate distinguishable conformers; isoheptane also includes six torsions but only three of them produce distinguishable structures. Both multiple-structure and torsional anharmonicity play significant roles in both molecules and must be considered when calculating their partition functions and thermodynamic properties. In the present work we include all structures for each molecule, and we employ the MS method[97] with both local harmonic and torsional anharmonicity approximations to calculate the

conformational−vibrational−rotational partition functions, absolute entropies, and heat capacities of the two molecules and the changes of entropy, enthalpy, and free energy in the isomerization reaction that inter-converts the two molecules at various temperatures. We also utilized Benson's empirical group additivity method to estimate the thermodynamic quantities of the two molecules. We will show that our calculated results agree well with experimental data from the American Petroleum Institute (API) tables,[103] with the Thermodynamics Research Center (TRC) data series,[104] and with the empirical estimates in the temperature range 298−1500 K, and extend our method to calculate thermodynamic properties at even higher temperatures. Note that temperature of 3000 K and higher are not of practical interest for most purposes but are interesting to illustrate the approach to the high-temperature limiting form and therefore are included in two of the tables.

We note that the present work includes anharmonicity in three ways. First of all, calculated harmonic frequencies are scaled by an empirical factor of 0.981 that has been determined[69] to reduce the average error in zero point energies calculated by the local harmonic approximation. This factor includes all kinds of anharmonicity, both principal (i.e., intra-mode) anharmonicity and mode-mode coupling.[105] To be precise, then, because our zero point energies are based on these effective frequencies, our low temperature results should be called quasiharmonic, although we often omit the "quasi" since the method is general enough to include either true harmonic frequencies or effective frequencies. The second way in which we include anharmonicity is the multiple-structure effect. The existence of multiple local minima on a potential energy surface is an anharmonic effect since a harmonic oscillator has only one local minimum

in its potential energy surface. Including all minima but treating each local minimum by the harmonic or quasiharmonic approximation is called the MS-LH approximation. (Notice, though, a possible semantic ambiguity since, from another point of view, the existence of multiple structures often (although not always) results from torsions, so the MS-LH treatment is the first step in taking account of torsions.) Finally we include explicit torsional anharmonicity, resulting in the MS-T approximation, which is designed to go to the correct high-temperature limit as far as torsions and overall rotations are concerned. But we should emphasize that we do not include other kinds of anharmonicity that become significant at high temperature. For example, principal bend anharmonicity[106,107] could increase the partition function at high temperature (thereby partly cancelling the effect of torsional anharmonicity), but this is beyond the scope of the present treatment.

Finally we note that all calculations in the present paper refer to the vapor phase, and in particular for temperatures below the boiling point they refer to the saturated vapor phase in the standard state of an ideal gas at a partial pressure of one bar. To consider thermodynamics in the condensed phase would require considerations of intermolecular forces and packing. That is beyond our scope. In addition, note that some of our temperatures are above the auto-ignition temperatures of *n*-heptane and isoheptane, but this is not a concern because we study the pure hydrocarbon systems without any air or oxygen.

2. Computational methods

2.1. Electronic structure calculations

The M06-2X density functional[64] with the 6-311+G(2df,2p) basis set[66,67,108] was applied to optimize the geometry and obtain the frequency for all the conformers of *n*-heptane and isoheptane. The 6-311+G(2df,2p) basis set is the same as the MG3S basis set[109] for H and C, and we will use the short name for brevity. The multilevel BMC-CCSD[110] method and the ab initio CCSD(T)-F12a[111,112] method with the jul-cc-pVTZ basis set[113] were used to calculate single-point energies at the M06-2X optimized geometries.

M06-2X density functional calculations were performed by using the *Gaussian 09* program;[68] the BMC-CCSD calculations were carried out using *MLGAUSS2.0*;[114] and CCSD(T)-F12a calculations were performed using *Molpro*.[115] The integration grid employed for density functional calculations of frequencies had 99 radial shells and 974 angular points per shell.

The frequencies used for the partition function calculations in the next section are obtained by using M06-2X/MG3S density functional calculations and multiplying the directly calculated values by a quasiharmonic frequency scaling factor[69] specific for hydrocarbons; this factor is 0.981. This frequency factor is calibrated[69] to—on average—correct the zero point energy calculated from the frequencies by the harmonic formula; since the zero point energy is dominated by high-frequency modes, this factor applies mainly to high-frequency modes, and it may be considered to be part of the electronic structure methodology. In practice the factor is applied by multiplying all Cartesian and internal-coordinate Hessian element by square of 0.981.[69]

2.2. Conformational−vibrational−rotational partition functions

Including multiple structures and making the harmonic approximation in the vicinity of each local minimum of the potential energy surface is called the local harmonic (LH) approximation, and calculations including torsional anharmonicity have a suffix –T. If one uses all structures (AS), one may call the resulting multi-structural methods MS-AS-T and MS-AS-LH. However, in the rest of this paper (and in future work, except when we need to emphasize that all structures are included), we will shorten MS-AS-T and MS-AS-LH to MS-T and MS-LH, respectively; this will not cause confusion in the present paper because we always employ all structures in the present article. (MS-AS-T and MS-AS-LH were called MS-AS and MS-HO, respectively, in the original[22] reference, but we now abandon that notation as being too easily misunderstood.)

The complete conformational−vibrational−rotational partition functions of *n*-heptane and isoheptane were calculated by the MS method[22] using the *MSTor* program;[116] in the MS-LH and MS-T versions of this method we respectively have

$$Q_{\text{con-rovib}}^{\text{MS-LH}} = \sum_{j=1}^{J} Q_{\text{rot},j} \exp\left(-\beta U_j\right) Q_j^{\text{HO}} \tag{1}$$

and

$$Q_{\text{con-rovib}}^{\text{MS-T}} = \sum_{j=1}^{J} Q_{\text{rot},j} \exp\left(-\beta U_j\right) Q_j^{\text{HO}} Z_j \prod_{\tau=1}^{t} f_{j,\tau} \tag{2}$$

where “con” denotes conformational, “rovib” denotes rotational-vibrational; $Q_{\text{rot},j}$ is the rotational partition function (including the rotational symmetry number in the

denominator) of structure *j*, Q_j^{HO} is the normal-mode local-harmonic-oscillator vibrational partition function calculated at structure *j*, Z_j is a factor designed to ensure that the MS-T scheme reaches the correct high-*T* limit (within the parameters of the model), and $f_{j,\tau}$ is an internal-coordinate torsional anharmonicity function that, in conjunction with Z_j, adjusts the harmonic partition function of structure *j* for the presence of the torsional motion τ.

Note that it is not necessary to assign each torsional motion to a specific normal mode. The MS-T approximation reduces to the MS-LH approximation in the low-temperature limit, and it approaches the free-rotor result in the high-temperature limit. The Z_j and $f_{j,\tau}$ factors, based in part on internal-coordinate Hessians, are designed to interpolate the partition function between these limits in the intermediate temperature range. In principle, more accurate interpolations could be carried out[22] if one calculated the barrier heights for torsional motions that interconvert the reactant structures with one another and the transition state structures with one another, but an advantage of the method employed here is that it does not require the expensive and labor-intensive step of finding and characterizing saddle points.

2.3. Thermodynamic function calculations

The energy and entropy functions can be calculated using the complete partition functions (including translational, electronic, and conformational−vibrational−rotational contributions) by the following:

$$E = -\frac{\partial \ln(Q)}{\partial \beta} \tag{3}$$

$$S^\circ = k_B + k_B \ln Q - \frac{1}{T}\left(\frac{\partial \ln Q}{\partial \beta}\right)_V \quad (4)$$

where $Q = Q_{\text{el}} Q_{\text{t}} Q_{\text{con-rovib}}$, in which Q_{el} and Q_{t} are electronic and translational partition functions, respectively. The translational partition function is evaluated for one mole of an ideal gas at a standard state pressure of one bar (0.986923 standard atmospheres).

Then the enthalpy and free energy can be obtained by

$$H = E + k_B T \quad (5)$$

$$G^\circ = H - TS^\circ \quad (6)$$

The heat capacity C_{p} can be determined using

$$C_{\text{p}} = \left(\frac{\partial H}{\partial T}\right)_p \quad (7)$$

3. Results and Discussion

3.1. Structures, energies, and rotational symmetry number of *n*-heptane

We label the carbons of *n*-heptane as shown in Figure 2.1.There are six internal rotation coordinates in the molecule, which describe torsions around the $C^{(1)}$–$C^{(2)}$, $C^{(2)}$–$C^{(3)}$, $C^{(3)}$–$C^{(4)}$, $C^{(4)}$–$C^{(5)}$, $C^{(5)}$–$C^{(6)}$, and $C^{(6)}$–$C^{(7)}$ bonds. Note that the torsional motions of the methyl groups, $-C^{(1)}H_3$ and $-C^{(7)}H_3$, in the molecule do not generate distinct structures due to the symmetry. Therefore, only the $C^{(2)}$–$C^{(3)}$, $C^{(3)}$–$C^{(4)}$, $C^{(4)}$–$C^{(5)}$, and $C^{(5)}$–$C^{(6)}$ torsional motions produce distinguishable conformers. Based on calculations using the M06-2X density functional with the MG3S basis set, 58 distinguishable structures (conformers) of *n*-heptane have been obtained in the present

work, and 56 of them consist of 28 pairs of mirror images. The remaining structures, due to symmetry (it has a mirror plane) does not have a distinguishable mirror image. Figure 2.2 shows 30 structures of *n*-heptane. Except for the first structure, all the others have corresponding mirror-image structures. Tables 2.1 and 2.2 show the naming convention and structural numbering that is used for labeling the structures. For instance, "**ap**$^{+}$**sc**$^{+}$**ac**$^{+}$**ap**$^{+}$" (structure 25) means the conformer of *n*-heptane with the first, second, third, and fourth dihedral angles in the ranges of 150 to 180, 30 to 60 and 90 to 120, and 150 to 180 degrees, respectively. Note that the structure **apapapap** has no mirror image pair due to its C_{2v} symmetry. The relative conformational energetic information and rotational symmetry numbers of these 58 structures are specified in Table 2.2. It is found that the BMC-CCSD and M06-2X energies agree very well with each other, but, for each of the structures, they are consistently lower than the energies calculated by CCSD(T)-F12a. The deviations between the M06-2X energy and the CCSD(T)-F12a energy range from 0.19 to 1.39 kcal/mol. Note that there are 11 structures (including the global minimum structure, and the highest-energy local-minimum structure), that contain a C_2 rotational axis, and the corresponding rotational symmetry number of these structures is 2. This symmetry number reduces the contributions of these structures to the conformational−vibrational−rotational partition functions.

3.2. Structures, energies, and rotational symmetry number of isoheptane

Isoheptane also contains six internal rotations, and the labeling of the carbon backbone is also displayed in Figure 2.1. The torsional motions are around the $C^{(1)}$–

$C^{(2)}$, $C^{(2)}$–$C^{(3)}$, $C^{(3)}$–$C^{(4)}$, $C^{(4)}$–$C^{(5)}$, $C^{(5)}$–$C^{(6)}$, and $C^{(2)}$–$C^{(7)}$ bonds. The internal rotation of the three methyl groups –$C^{(1)}H_3$, –$C^{(6)}H_3$, and –$C^{(7)}H_3$ generates identical conformers; thus they do not contribute to the multiple-structure effect., whereas the torsional motions around the $C^{(2)}$–$C^{(3)}$ and $C^{(3)}$–$C^{(4)}$, and $C^{(4)}$–$C^{(5)}$ bonds do produce distinguishable conformers. In total, 37 structures were obtained for isoheptane using the M06-2X density functional in the present work, and they are shown in Figure 2.3. Tables 2.1 and 2.3 show the naming and numbering convention that is used for labeling of the structures, and the relative conformational energy and rotational symmetry number of each structure are given in the Table 2.3. As for *n*-heptane, the relative conformational energies calculated using CCSD(T)-F12a are larger than those calculated with either BMC-CCSD or M06-2X. The deviations between the M06-2X and CCSD(T)-F12a results are smaller than those for *n*-heptane; they range from 0.12 to 1.09 kcal/mol. None of the structures has a rotational symmetry axis; thus the overall rotational symmetry numbers of all structures are one.

3.3. Conformational−vibrational−rotational partition functions of *n*-heptane and isoheptane in various approximations

The number of structures of each isomer provides the first indication that the torsions are strongly coupled. For *n*-heptane, excluding the two methyl torsions, because methyl torsions do not generate more than one distinguishable structure, gives four torsions, and four independent torsions generate n^4 structures where n is the number of structures generated by an independent torsion. For ideal torsions, n would be 3 (two gauche and one trans conformer) and n^4 would equal 81, but we find only 58

distinguishable structures. For isoheptane, separable ideal torsions would generate 3^3 = 27 structures, but we instead find 37 distinguishable structures. To understand these differences we must consider two issues: rotational symmetry and the pentane effect.

First consider rotational symmetry. As explained in the original MS-T paper,[97] the Voronoi calculation of the effective periodicities includes not just the indistinguishable structures, but also all the distinguishable structures located in the full torsion space. For example, in *n*-heptane, starting from the all-trans structure (structure 1), rotation of the $C^{(2)}$–$C^{(3)}$, $C^{(3)}$–$C^{(4)}$, $C^{(4)}$–$C^{(5)}$ and $C^{(5)}$–$C^{(6)}$ bonds by −122.95, −122.26, −116.63, and −270.06 degrees, respectively, gives the same structure (structure $\mathbf{sc^+sc^+g^+ac^-}$) as is obtained by rotation of these bonds by −270.06, −116.63, −122.26, and −122.95 degrees, respectively. Although there is only one distinguishable structure generated, both of these structures must be included in the torsional space for the effective periodicity calculations. For the present molecules, this kind of phenomenon occurs in *n*-heptane but not in isoheptane. In fact, counting both distinguishable structures and indistinguishable ones, *n*-heptane has 105 structures; these consist of 11 structures with a rotational symmetry number of two and 94 structures with a rotational symmetry of one, but overall rotations map 47 of these into the other 47, so the final number of distinguishable structures is 58. Thus, in considering the torsional landscape one must actually compare 105 structures (not 58) to the ideal number of 81 for *n*-heptane. For isoheptane, there is no rotational symmetry, so one must compare 37 structures to the ideal number of 27 in this case.

Next consider the pentane effect. For alkane or polyethylene chains of length five carbons or longer, it is well known that structures with $\mathbf{g^+g^-}$ or $\mathbf{g^-g^+}$ configurations

for successive torsions are either excluded or made unfavorable by steric repulsion; this is called the pentane effect.[39,40,51,117−130,] Naively one might simply assume that these structures are missing and that the number of structures would be less than the ideal number. In fact, Tables 2.2 and 2.3 show that none of the *n*-heptane or isoheptane structures contains $\mathbf{g}^{+}\mathbf{g}^{-}$ or $\mathbf{g}^{-}\mathbf{g}^{+}$. However, the situation is actually more complicated because the pentane effect can also make the conformational landscape more rugged. The sterically disfavored structure may, for example, be replaced by two structures,[17,39,51,123,124] for instance, in isoheptane the $\mathbf{g}^{+}\mathbf{g}^{-}$ conformation of $C^{(1)}$–$C^{(2)}$–$C^{(3)}$–$C^{(4)}$, $C^{(2)}$–$C^{(3)}$–$C^{(4)}$–$C^{(5)}$ is replaced by two structures: with $\mathbf{g}^{+}\mathbf{sc}^{-}$ for these torsions in structure 3 and with $\mathbf{sc}^{+}\mathbf{g}^{-}$ for these torsions in structure 18. This kind of effect makes the total number of conformers larger than the ideal number, and this added ruggedness explains why both *n*-heptane and isoheptane have more structures than the ideal number (105 vs. 81 and 37 vs. 27).

If one creates a list of 27 ideal structures for isoheptane by simply assigned **ap**, $\mathbf{g}^{+}$, or $\mathbf{g}^{-}$ to every torsion in all combinations, one finds that 15 of the 27 ideal structures have neither $\mathbf{g}^{+}\mathbf{g}^{-}$ nor or $\mathbf{g}^{-}\mathbf{g}^{+}$, and 10 have one of these, and two have two of them. Replacing each of the 12 disfavored structures by 2 structures yields the total of 37 structures that are observed.

The existence of this kind of ruggedness provides further confirmation that the torsional motion must be considered strongly coupled in partition function calculations.

We can compare some details of our structure counts for *n*-heptane to previous work. For this purpose we introduce the term "unique (nonisomorphic) conformers" used by Tasi et al.[51] to denote the number of structures excluding those generated from

ones already in the list by 180 deg rotation (here we are referring to overall rotation) or mirror reflection; Goto et al.[124] call these generatable conformers "symmetrically equivalent conformers". Scott and Scheraga[117] used a molecular mechanics potential functions and found 28 unique nonisomorphic conformers and a total of 101 conformers in the full torsional space; Goto et al. used the MM2 molecular mechanics method too explore the torsional landscape and they found 31 unique nonisomorphic conformers and a total of 109 conformers in the full torsional space; Tasi et al. used a parametrized effective one-electron quantum chemical model and found 30 unique nonisomorphic conformers and a total of 107 conformers in the full torsional space; and we find 30 unique nonisomorphic conformers (the 30 rows of Table 2.2) and a total of 105 conformers in the full torsional space. The agreement of these numbers of structures is reasonable since different electronic structure or molecular mechanics methods do not necessarily predict the same number of structures and furthermore the higher-energy ones might easily be missed in searches.

It is worthwhile to emphasize some statistical mechanical issues here. Goto[124] assigned each of the conformers a "statistical weight" equal to one plus the number of structures generated from it by 180 deg rotation, mirror reflection, or a combination of rotation and reflection. That is correct for the structures generated by mirror reflection but not for the structures generated from the original structure or its mirror image by rotation. If overall rotation maps a structure onto the same unique nonisomorphic conformer, then the rotated image should not be counted, and furthermore a rotational symmetry number of two should be included in the rotational partition function of the original structure. If overall rotation maps a structure into a different structure from the

list constructed considering only torsional symmetry, then one has two choices: either (i) count both and use a rotational symmetry number of 2 for both or (ii) count only one of them and use a rotational symmetry number of one. We make the latter choice (although the first choice might be preferred by some because it has the advantage that the rotational symmetry number is the same for every structure). Scott and Scheraga[117] computed a "statistical weight" in the same way as Goto et al., but they did not perform statistical mechanical calculations. Tasi et al.[51] include self-images that are equivalent by rotation in their figures.

The partition functions calculated for *n*-heptane and isoheptane in the present work are given in Tables 2.4 and 2.5. The zero of energy for the partition function calculations is taken to be the energy at the global minimum structure of the isomer under consideration, *n*-heptane or isoheptane. In *n*-heptane, four of the torsions [$C^{(2)}$–$C^{(3)}$, $C^{(3)}$–$C^{(4)}$, $C^{(4)}$–$C^{(5)}$ and $C^{(5)}$–$C^{(6)}$] are involved in a strongly coupled[97] (SC) group; the other two torsions [$C^{(1)}$–$C^{(2)}$, $C^{(6)}$–$C^{(7)}$] are considered to be nearly separable (NS). In isoheptane, three torsions [$C^{(2)}$–$C^{(3)}$ and $C^{(3)}$–$C^{(4)}$, and $C^{(4)}$–$C^{(5)}$] are strongly coupled and the other three [$C^{(1)}$–$C^{(2)}$ and $C^{(5)}$–$C^{(6)}$, and $C^{(2)}$–$C^{(7)}$] are treated as nearly separable torsions. The nearly separable torsions are all internal rotations of methyl groups that produce three identical structures. For these torsions we can take $M_{j,\tau}$ (the total number of minima, whether distinguishable or not, along torsional coordinate τ of structure *j*) as three. For the strongly coupled torsions, the $M_{j,\tau}$ parameters are obtained by four-dimensional and three-dimensional Voronoi tessellation methods[97,116] for *n*-heptane and isoheptane, respectively.

Tables 2.4 and 2.5 show that the partition functions obtained by CCSD(T)-F12a are smaller than those by BMC-CCSD, which are smaller than those by M06-2X. The percent deviations between CCSD(T)-F12a and M06-2X results decrease with temperature for both *n*-heptane and isoheptane as shown in Figures 2.4 and 2.5. The percent deviations between BMC-CCSD and M06-2X decrease with temperatures for *n*-heptane, but they are close to zero for isoheptane as shown in Figures 2.4 and 2.5. These temperature-dependent behaviors of deviations are understandable since the differences of the conformation energies calculated by CCSD(T)-F12a and M06-2X are large, but those between BMC-CCSD and M06-2X are small.

For *n*-heptane, Table 2.4 and Figure 2.6 show the differences of the partition functions calculated by the MS-LH and MS-T approximations. Two asymptotic trends have been correctly designed into the approximations:[97] (1) In the limit where the temperature approaches zero, the ratio $Q_{\text{con-rovib}}^{\text{MS-T}} / Q_{\text{con-rovib}}^{\text{MS-LH}}$ goes to one; and (2) as the temperature tends to infinity, the ratio goes to zero. As the temperature increases from zero, the $Q_{\text{con-rovib}}^{\text{MS-T}} / Q_{\text{con-rovib}}^{\text{MS-LH}}$ ratio first increases dramatically and then decreases gradually. At low temperature the LH approximation underestimates the partition functions, and at high *T* it overestimates it. Similar behavior is observed in Table 2.5 and Figure 2.7 for isoheptane.

Interestingly, it is found that the ratio of isoheptane partition functions to *n*-heptane partition functions decays dramatically with increasing temperature and then reaches a steady value at the high-temperature limit in both MS-LH and MS-T calculations. In the MS-T approximation, at 298 K the ratio is 1.34, 1.15, or 1.06 for

CCSD(T)-F12a, BMC-CCSD, or M06-2X calculations, respectively; and at 10000 K, the ratio becomes 0.55, 0.55, and 0.55. As already noted, *n*-heptane has 59 structures and isoheptane has 37, and these two numbers are correlated with the asymptotic behavior in the high-temperature range. Based on CCSD(T)-F12a, BMC-CCSD, and M06-2X calculations, the relative conformational energies have a spread from 0 to 6.18, 5.67, and 5.61 kcal/mol for *n*-heptane, and range from 0 to 4.50, 4.08, and 4.09 kcal/mol for isoheptane. Because of the higher conformational energies of *n*-heptane, at low temperature many conformers contribute much less to the total partition functions than for isoheptane; thus its partition functions are smaller. When temperature increases, the contribution from higher-energy conformers becomes significant, and the partition functions of *n*-heptane become larger than those of isoheptane.

3.4. Entropies and heat capacities of *n*-heptane and isoheptane

We employed the eqs 3, 4, 5, and 7 to calculate the standard-state entropy and heat capacity of *n*-heptane and isoheptane. The results are given in the Tables 2.6−2.9. In addition, we apply Benson's group additivity parameters[94,95] to estimate the same thermodynamic quantities, and these results are also tabulated in Tables 2.6−2.9. Note that Benson's heat-of-formation parameters in Ref. 95 are updated from those in Ref. 94, but the entropy and heat capacity parameters are still the same as those in Ref. 94. (Because Benson's parameters and the thermodynamic functions in the API tables correspond to a standard state of 1 atm, we correct them to a standard state of 1 bar in the present article; no such correction is needed for the values in the TRC tables, which already correspond to a standard state at 1 bar.)

For both *n*-heptane and isoheptane in the temperature range from 298 K to 2400 K, as discussed above, the partition functions obtained by the MS-LH approximation are consistently smaller than those by MS-T. However, the calculated entropies and heat capacities calculated using the MS-LH approximation are smaller than those obtained by MS-T in the low-temperature regime but larger in high-temperature regime. This observation can be explained by eq. 4, which shows that the entropy depends on the partition function and its temperature derivative. As a further consequence of this dependence, the ratio of the MS-T partition function to the MS-LH one is larger than the entropy ratio between MS-T and MS-LH results at each temperature (as shown in Figures 2.9 and 2.10).

Note that Benson's empirical parameters[94,95] are based on the API tables, which are based on experimental data. The direct experimental measurement of the entropy of *n*-heptane by calorimetric method was accomplished by Pitzer at 371.5 K.[131] Waddington and Huffman[132] determined the heat capacity of *n*-heptane experimentally between 350 K and 470 K, and the heat capacity data at the other temperatures in the range from 298 K to 1500 K were calculated by Person and Pimental.[133] All of these results were used to generate the thermodynamic data in the API tables. Huffman et al.[92] determined the heat capacity isoheptane at low temperature in the liquid and solid state, and we did not find direct experimental measurements of the heat capacity in the gas phase in the temperature range from 298 K to 1500 K. The API tables recommend that the heat capacity of isoheptane should be assumed to be the same as *n*-heptane (our calculations confirm that this holds within 0.1 cal K^{-1} mol^{-1} for 300−2000 K), and entropy and other thermodynamic-data in the API tables for isoheptane are those

estimated by Park et al. at 298 K.[134] The TRC tables are based on both direct measurements of thermodynamic properties and inferences from spectroscopic data.

For *n*-heptane, Table 2.8 demonstrates the heat capacity calculated by MS-T agrees well with the experimental values in the temperature range where they are available. At temperatures out of this range, MS-T calculations agree with Benson's estimates, with the TRC data series, and with the API data set very well. The entropy values we calculated using MS-T agree well with Pitzer's experimental data at 375.1 K, with the best results being obtained using CCSD(T)-F12a energies. At other temperatures between 298 and 1500 K, MS-T calculations with CCSD(T)-F12a energies are also consistent with Benson's estimates, the TRC data series, and the API data. Similarly, for the entropy and heat capacity of isoheptane, Tables 2.7 and 2.9 show good agreement between the MS-T calculations and estimates based on Benson's data, the TRC data series, and the API data. All of these comparisons validate the MS-T method for predicting entropy and heat capacity.

3.5. Change of entropies, enthalpies, and free energies in the isomerization reaction between *n*-heptane and isoheptane

Using eqs 4, 5, and 6, we obtain the entropy, enthalpy, and free energy for *n*-heptane and isoheptane and the change of entropies, enthalpies, and free energies in the isomerization reaction between *n*-heptane and isoheptane. These results are shown in Table 2.10. The MS-T and MS-LH calculations agree well with each other at low temperature for ΔS^{o}, ΔH, and ΔG^{o}, but the deviations between the two approximation

methods are larger in the high-temperature range, where the LH approximation breaks down.

Note that, our calculated data for the ΔS^{o} results agree very well with estimations based on Benson's empirical data, and they are also close to the TRC data series and the API data set. For the ΔH results, Benson's method gives negative deviations compared with the API data; MS-LH and MS-T methods using M06-2X and CCSD(T)-F12a energies give positive deviations, and those using BMC-CCSD energies give negative deviations; but they all still agree with the API data set within ±1 kcal/mol over the whole temperature range. A similar trend is observed for the ΔG^{o} results.

4. Conclusion

In the present work, we applied the MS-T and MS-LH methods to calculate the partition functions for *n*-heptane and isoheptane. Furthermore, we used the partition functions to predict the thermodynamic quantities, such entropy and heat capacity, for these two species, and we also calculated ΔS^{o}, ΔH, and ΔG^{o} for the isomerization reaction between *n*-heptane and isoheptane. The results show that all calculated thermodynamics quantities based on MS-T agree well with experimental data, in particular the API tables, the TRC data series, and estimates based on Benson's empirical parameters in the temperature range from 298 K to 1500 K. This shows that the MS-T method including both multi-structural anharmonicity and torsional anharmonicity effect can be used to calculate the thermodynamic properties for molecules containing many torsions. It also give us confidence that we can extend the

application of electronic structure theory with the MS-T method to predict the thermodynamic properties at even higher temperatures that are not included in the empirical API tables or TRC data series, and where empirical estimation would be a dangerous extrapolation, or—even more importantly for developing combustion mechanisms—to predict the thermodynamic parameters of many multiple-structure molecules where no data is available.

Table 2.1 Labeling of structures[a]

	Abbreviation	dihedral angle range (deg)
+syn-periplanar	**sp**$^{+}$	[0, 30]
−syn-periplanar	**sp**$^{-}$	[-30, –0]
+syn-clinal	**sc**$^{+}$	[30, 60]
−syn-clinal	**sc**$^{-}$	[–60, –30]
+gauche	**g**$^{+}$	[60, 90]
−gauche	**g**$^{-}$	[–90, –60]
+anti- clinal	**ac**$^{+}$	[90, 120]
−anti- clinal	**ac**$^{-}$	[–120, –90]
+anti-periplanar	**ap**$^{+}$	[150, 180]
−anti-periplanar	**ap**$^{-}$	[–180, –150]
anti-periplanar	**ap**	180

[a]The dihedral angles in used for torsions are and $C^{(1)}$–$C^{(2)}$–$C^{(3)}$–$C^{(4)}$, $C^{(2)}$–$C^{(3)}$–$C^{(4)}$–$C^{(5)}$, $C^{(3)}$–$C^{(4)}$–$C^{(5)}$–$C^{(6)}$, and $C^{(4)}$–$C^{(5)}$–$C^{(6)}$–$C^{(7)}$ for *n*-heptane; the dihedral angles in used for torsions are and $C^{(1)}$–$C^{(2)}$–$C^{(3)}$–$C^{(4)}$, $C^{(2)}$–$C^{(3)}$–$C^{(4)}$–$C^{(5)}$, and $C^{(3)}$–$C^{(4)}$–$C^{(5)}$–$C^{(6)}$ for isoheptane.

Table 2.2 Name, sequence number, energy[a] (kcal/mol), and rotational symmetry number of sstructures of *n*-heptane[a]

structures	Number	energy			σ_j
	j	M06-2X	BMC-CCSD	CCSD(T)-F12a	
apapap	1	0.00	0.00	0.00	2
ap$^-$ap$^-$g$^-$ap$^-$, ap$^+$ap$^+$g$^+$ap$^+$	2, 3	0.47	0.46	0.58	1
ap$^-$ap$^-$sc$^-$sc$^-$, ap$^+$ap$^+$sc$^+$sc$^+$	4, 5	0.47	0.41	0.57	1
ap$^-$ap$^-$ap$^-$g$^-$, ap$^+$ap$^+$ap$^+$g$^+$	6, 7	0.47	0.48	0.86	1
ap$^+$sc$^+$sc$^+$ap$^+$, ap$^-$sc$^-$sc$^-$ap$^-$	8, 9	0.48	0.43	0.85	2
ap$^+$sc$^+$sc$^+$sc$^+$, ap$^-$sc$^-$sc$^-$sc$^-$	10, 11	0.88	0.86	1.13	1
sc$^+$sc$^+$sc$^+$sc$^+$, sc$^-$sc$^-$sc$^-$sc$^-$	12, 13	0.92	0.88	1.14	2
g$^+$ap$^+$sc$^+$sc$^+$	14	0.98	0.91	1.15	1
ap$^+$g$^+$ap$^+$g$^+$, ap$^-$g$^-$ap$^-$g$^-$	15, 16	1.11	1.03	1.25	1
g$^+$ap$^+$ap$^+$g$^+$, g$^-$ap$^-$ap$^-$g$^-$	17, 18	0.49	0.54	1.13	1
g$^+$ap$^+$ap$^+$g$^-$, g$^-$ap$^-$ap$^-$g$^+$	19, 20	0.82	0.86	1.37	1
g$^+$ap$^+$sc$^-$sc$^-$, g$^-$ap$^-$sc$^+$sc$^+$	21, 22	1.09	1.09	1.56	1
ap$^+$g$^+$ap$^+$g$^-$, ap$^-$g$^-$ap$^-$g$^+$	23, 24	0.54	0.71	1.46	2
ap$^+$sc$^+$ac$^+$ap$^+$, ap$^-$sc$^-$ac$^-$ap$^-$	25, 26	2.25	2.31	2.58	1
ap$^+$g$^+$sc$^+$ac$^-$, ap$^-$g$^-$sc$^-$ac$^+$	27, 28	2.35	2.35	2.66	1
ap$^+$ap$^+$ac$^-$sc$^+$, ap$^-$ap$^-$ac$^+$sc$^-$	29, 30	2.18	2.18	2.50	1
ap$^+$ap$^+$g$^-$g$^-$, ap$^-$ap$^-$g$^+$g$^+$	31, 32	2.25	2.3	2.88	1
ap$^-$ap$^-$sc$^-$ac$^+$, ap$^+$ap$^+$sc$^+$ac$^-$	33, 34	2.29	2.31	2.83	1
sc$^+$sc$^+$g$^+$ac$^-$, sc$^-$sc$^-$g$^-$ac$^+$	35, 36	2.68	2.74	3.14	1
g$^+$g$^+$ac$^-$g$^-$, g$^-$g$^-$ac$^+$g$^+$	37, 38	2.81	2.86	3.25	1
g$^+$ap$^-$ac$^+$sc$^-$, g$^-$ap$^+$ac$^-$sc$^+$	39, 40	2.72	2.86	3.24	1
g$^+$ap$^+$ac$^-$sc$^+$, g$^-$ap$^-$ac$^+$sc$^-$	41, 42	2.81	2.81	3.17	1
ap$^+$sc$^+$ac$^-$g$^-$, ap$^-$sc$^-$ac$^+$g$^+$	43, 44	2.77	2.73	3.13	1
ap$^-$g$^+$ac$^+$sc$^-$, ap$^+$g$^-$ac$^-$sc$^+$	45, 46	2.59	2.72	3.39	1
sc$^+$ap$^+$g$^+$g$^-$, sc$^-$ap$^-$g$^-$g$^+$	47, 48	2.67	2.69	3.37	1
ap$^-$ac$^+$g$^-$g$^+$, ap$^+$ac$^-$g$^+$g$^-$	49, 50	3.88	3.94	4.72	1
sc$^+$ac$^-$ac$^-$sc$^+$, sc$^-$ac$^+$ac$^+$sc$^-$	51, 52	3.92	4.19	4.85	2
g$^+$ac$^+$g$^-$ac$^+$, g$^-$ac$^-$g$^+$ac$^-$	53, 54	4.75	4.72	5.36	1

$ac^+g^-ac^-sc^+$, $ac^-g^+ac^+sc^-$	55, 56	5.29	5.39	5.88	1
$ac^+g^-g^-ac^+$, $ac^-g^+g^+ac^-$	57, 58	5.61	5.67	6.18	2

[a] The energy is calculated by the M06-2X, BMC-CCSD, and CCSD(T)-F12a methods, respectively. If overall rotation maps a structure onto the same unique nonisomorphic conformer, then the rotated image is not counted, and a rotational symmetry number of two is included in the rotational partition function of the original structure. If overall rotation maps a structure onto a different structure from the list constructed considering only torsional symmetry, then we include only one of them and use a rotational symmetry number of one.

Table 2.3 Name convention, sequence number, energy[a] (kcal/mol), and rotational symmetry number of isoheptane

structures	number	energy			σ_j
	j	M06-2X	BMC-CCSD	CCSD(T)-F12a	
sc$^-$ap$^-$ap$^-$, sc$^+$ap$^+$ap$^+$	1, 2	0.00	0.00	0.00	1
g$^+$sc$^-$ap$^-$, g$^-$sc$^+$ap$^+$	3, 4	0.01	0.03	0.30	1
g$^+$sc$^-$sc$^-$, g$^-$sc$^+$sc$^+$	5, 6	0.02	0.09	0.57	1
sc$^-$ap$^+$g$^+$, sc$^+$ap$^-$g$^-$	7, 8	0.37	0.4	0.53	1
sc$^+$ap$^-$g$^+$, sc$^-$ap$^+$g$^-$	9, 10	0.65	0.59	0.69	1
g$^+$ap$^-$sc$^-$, g$^-$ap$^+$sc$^+$	11, 12	0.68	0.70	0.90	1
apapap	13	0.69	0.67	0.75	1
ap$^+$ap$^+$g$^+$, ap$^-$ap$^-$g$^-$	14, 15	1.22	1.24	1.43	1
g$^+$ac$^+$ap$^-$, g$^-$ac$^-$ap$^+$	16, 17	1.70	1.81	1.95	1
sc$^+$g$^-$ac$^+$, sc$^-$g$^+$ac$^-$	18, 19	1.98	2.04	2.43	1
sp$^+$sc$^+$ap$^+$, sp$^-$sc$^-$ap$^-$	20, 21	2.18	2.17	2.36	1
g$^-$ac$^-$g$^-$, g$^+$ac$^+$g$^+$	22, 23	2.26	2.32	2.54	1
sp$^+$g$^+$g$^+$, sp$^-$g$^-$g$^-$	24, 25	2.29	2.32	2.70	1
ap$^-$ac$^+$ap$^-$, ap$^+$ac$^-$ap$^+$	26, 27	2.42	2.48	2.69	1
ap$^+$g$^+$ap$^+$, ap$^-$g$^-$ap$^-$	28, 29	2.60	2.67	2.98	1
ap$^+$g$^+$sc$^+$, ap$^-$g$^-$sc$^-$	30, 31	2.61	2.83	3.34	1
sc$^-$g$^-$ac$^+$, sc$^+$g$^+$ac$^-$	32, 33	4.09	4.08	4.50	1
ap$^-$ac$^+$g$^+$, ap$^+$ac$^-$g$^-$	34, 35	3.06	3.10	3.38	1
sc$^+$ac$^+$g$^+$, sc$^-$ac$^-$g$^-$	36, 37	2.16	2.18	2.48	1

[a] The energy is calculated by the M06-2X, BMC-CCSD, and CCSD(T)-F12a methods, respectively. If overall rotation maps a structure onto the same unique nonisomorphic conformer, then the rotated image is not counted, and a rotational symmetry number of two is included in the rotational partition function of the original structure. If overall rotation maps a structure onto a different structure from the list constructed considering only torsional symmetry, then we include only one of them and use a rotational symmetry number of one.

Table 2.4 Calculated conformational-vibrational-rotational partition function of *n*-heptane

T (K)	MS-LH			MS-T		
	M06-2X	BMC-CCSD[a]	CCSD(T)-F12a[b]	M06-2X	BMC-CCSD[a]	CCSD(T)-F12a[b]
298	2.72E−90	2.51E−90	1.81E−90	4.01E−90	3.71E−90	2.70E−90
300	1.32E−89	1.22E−89	8.83E−90	1.95E−89	1.81E−89	1.32E−89
400	1.04E−63	9.69E−64	7.37E−64	1.79E−63	1.68E−63	1.29E−63
500	1.07E−47	1.01E−47	8.02E−48	2.12E−47	2.00E−47	1.60E−47
600	1.27E−36	1.21E−36	9.84E−37	2.77E−36	2.64E−36	2.16E−36
800	6.33E−22	6.09E−22	5.17E−22	1.54E−21	1.48E−21	1.27E−21
1000	2.96E−12	2.87E−12	2.51E−12	7.42E−12	7.18E−12	6.29E−12
1500	3.38E+03	3.31E+03	3.00E+03	7.52E+03	7.35E+03	6.67E+03
2000	9.71E+12	9.55E+12	8.87E+12	1.74E+13	1.71E+13	1.58E+13
2400	4.63E+18	4.57E+18	4.29E+18	6.81E+18	6.72E+18	6.28E+18
3000	2.48E+25	2.46E+25	2.33E+25	2.73E+25	2.70E+25	2.55E+25
4000	6.87E+33	6.82E+33	6.56E+33	4.78E+33	4.74E+33	4.54E+33
6000	3.02E+45	3.00E+45	2.92E+45	9.64E+44	9.59E+44	9.29E+44
8000	4.39E+53	4.37E+53	4.28E+53	7.45E+52	7.43E+52	7.24E+52
10000	8.78E+59	8.75E+59	8.61E+59	8.78E+58	8.76E+58	8.58E+58

[a]BMC-CCSD//M06-2X/MG3S.

[b]CCSD(T)-F12a/jul-cc-pVTZ//M06-2X/MG3S.

Table 2.5 Calculated conformational-vibrational-rotational partition function of isoheptane

T (K)	MS-LH			MS-T		
	M06-2X	BMC-CCSD[a]	CCSD(T)-F12a[b]	M06-2X	BMC-CCSD[a]	CCSD(T)-F12a[b]
298	3.03E−90	3.04E−90	2.55E−90	4.45E−90	4.46E−90	3.76E−90
300	1.47E−89	1.47E−89	1.23E−90	2.16E−89	2.17E−89	1.83E−89
400	9.35E−64	9.36E−64	8.09E−64	1.61E−63	1.61E−63	1.40E−63
500	8.71E−48	8.71E−48	7.68E−48	1.70E−47	1.70E−47	1.51E−47
600	9.67E−37	9.66E−37	8.66E−36	2.07E−36	2.08E−36	1.87E−36
800	4.49E−22	4.48E−22	4.10E−22	1.07E−21	1.07E−21	9.82E−22
1000	2.02E−12	2.02E−12	1.88E−12	4.92E−12	4.92E−12	4.58E−12
1500	2.20E+03	2.19E+03	2.08E+03	4.71E+03	4.70E+03	4.46E+03
2000	6.17E+12	6.15E+12	5.91E+12	1.06E+13	1.05E+13	1.01E+13
2400	2.90E+18	2.90E+18	2.80E+18	4.07E+18	4.06E+18	3.91E+18
3000	1.54E+25	1.54E+25	1.49E+25	1.61E+25	1.60E+25	1.55E+25
4000	4.20E+33	4.20E+33	4.10E+33	2.77E+33	2.76E+33	2.69E+33
6000	1.82E+45	1.82E+45	1.79E+45	5.50E+44	5.48E+44	5.38E+44
8000	2.63E+53	2.63E+53	2.60E+53	4.23E+52	4.22E+52	4.16E+52
10000	5.24E+59	5.23E+59	5.19E+59	4.97E+58	4.96E+58	4.90E+58

[a]BMC-CCSD//M06-2X/MG3S.

[b]CCSD(T)-F12a/jul-cc-pVTZ//M06-2X/MG3S.

Table 2.6 Standard-state entropy of *n*-heptane in cal mol^{-1} K^{-1} at various temperatures

T (K)	MS-LH			MS-T			Benson[c]	Exp.-API[d]	Exp.-TRC[e]	Exp[f]
	M06-2X	BMC-CCSD[a]	CCSD(T)-F12a[b]	M06-2X	BMC-CCSD[a]	CCSD(T)-F12a[b]				
298	101.30	101.21	100.91	103.03	102.95	102.67	102.21	102.27	102.32	
300	101.55	101.47	101.17	103.30	103.21	102.94	102.48	102.53	102.56	
371.5	110.44	110.39	110.18	112.58	112.53	112.34	111.81			111.80±0.3
400	113.93	113.89	113.71	116.20	116.15	115.99	115.44	115.45	115.44	
500	126.00	125.97	125.84	128.51	128.48	128.36	127.76	127.77	127.75	
600	137.66	137.64	137.54	140.21	140.18	140.09	139.45	139.42	139.53	
800	159.45	159.44	159.38	161.73	161.72	161.65	160.98	160.98	161.23	
1000	179.18	179.17	179.13	180.98	180.97	180.91	180.26	180.25	180.52	
1500	220.69	220.69	220.67	221.19	221.19	221.14	220.40		220.60	
2000	253.70	253.70	253.69	253.01	253.02	252.98				
2400	275.72	275.72	275.71	274.20	274.20	274.18				

[a]BMC-CCSD//M06-2X/MG3S.

[b]CCSD(T)-F12a/jul-cc-pVTZ//M06-2X/MG3S.

[c]Using Benson's data from Ref. 94 and adding 0.026 cal mol^{-1} K^{-1} to convert from a standard pressure of 1 atm to a standard pressure of 1 bar.

[d]Using API data from Ref. 103 and adding 0.026 cal mol^{-1} K^{-1} to convert from a standard pressure of 1 atm to a standard pressure of 1 bar.

[e]Using TRC data from Ref. 104.

[f]The experimental data come from Ref. 131, and we added 0.026 cal mol^{-1} K^{-1} to convert from a standard pressure of 1 atm to a standard pressure of 1 bar.

Table 2.7 Standard-state entropy of isoheptane in cal mol^{-1} K^{-1} at various temperatures

T (K)	MS-LH			MS-T			Benson[c]	Exp-API[d]	Exp-TRC[e]
	M06-2X	BMC-CCSD[a]	CCSD(T)-F12a[b]	M06-2X	BMC-CCSD[a]	CCSD(T)-F12a[b]			
298	99.76	99.77	99.62	101.48	101.49	101.36	100.90	100.38	100.50
300	100.02	100.02	99.88	101.75	101.76	101.63	101.16	100.62	100.74
400	112.61	112.61	112.51	114.82	114.82	114.74	114.08	114.03	113.65
500	124.79	124.79	124.71	127.22	127.22	127.16	126.40	126.63	126.05
600	136.51	136.50	136.45	138.98	138.97	138.92	138.11	138.63	137.93
800	158.37	158.37	158.33	160.56	160.55	160.51	159.69	160.33	159.73
1000	178.12	178.12	178.09	179.83	179.82	179.78	179.01	179.73	179.33
1500	219.65	219.64	219.63	220.02	220.02	219.99	219.21		220.12
2000	252.66	252.65	252.64	251.84	251.83	251.81			
2400	274.67	274.67	274.66	273.02	273.01	272.99			

[a]BMC-CCSD//M06-2X/MG3S.

[b]CCSD(T)-F12a/jul-cc-pVTZ//M06-2X/MG3S.

[c]Using Benson's data from Ref. 13 and adding 0.026 cal mol^{-1} K^{-1} to convert from a standard pressure of 1 atm to a standard pressure of 1 bar.

[d]Using API data from Ref. 103 and adding 0.026 cal mol^{-1} K^{-1} to convert from a standard pressure of 1 atm to a standard pressure of 1 bar.

[e]Using TRC data from Ref. 104.

Table 2.8 Heat capacity of *n*-heptane in cal mol^{-1} K^{-1} at various temperatures

T (K)	MS-LH			MS-T			Benson[c]	Exp.-API[d]	Exp.-TRC[e]	Exp[f]
	M06-2X	BMC-CCSD[a]	CCSD(T)-F12a[b]	M06-2X	BMC-CCSD[a]	CCSD(T)-F12a[b]				
357.1	44.10	44.23	44.60	45.89	46.00	46.35	46.14			45.77
373.2	45.90	46.02	46.36	47.61	47.70	48.02	47.83			47.51
400.4	48.94	49.04	49.34	50.45	50.54	50.81	50.62			50.37
434.4	52.65	52.73	52.99	53.89	53.96	54.18	53.97			53.85
466.1	55.99	56.06	56.28	56.95	57.01	57.20	56.96			57.00
300	37.57	37.76	38.31	39.52	39.69	40.24	39.88	39.86	39.67	
400	48.89	48.99	49.29	50.41	50.49	50.77	50.43	50.42	50.36	
500	59.41	59.47	59.66	60.06	60.12	60.27	60.05	60.07	60.25	
600	68.52	68.56	68.71	68.29	68.33	68.43	68.33	68.33	68.69	
800	82.97	82.99	83.09	81.34	81.37	81.43	81.39	81.43	81.81	
1000	93.70	93.71	93.78	91.15	91.17	91.22	91.24	91.20	91.20	
1500	110.28	110.28	110.32	106.51	106.52	106.56	106.41	106.40	106.12	
2000	118.73	118.73	118.75	114.37	114.38	114.41				
2400	122.63	122.63	122.65	117.99	117.99	118.02				

[a]BMC-CCSD//M06-2X/MG3S.

[b]CCSD(T)-F12a/jul-cc-pVTZ//M06-2X/MG3S.

[c]Using Benson's data from Ref. 13.

[d]Using API data from Ref. 103.

[e]Using TRC data from Ref. 104.

[f]The experimental data are from Ref. 132.

Table 2.9 Heat capacity of isoheptane in cal mol^{-1} K^{-1} at various temperatures

T (K)	MS-LH			MS-T			Benson[c]	Exp.-API[d]	Exp.-TRC[e]
	M06-2X	BMC-CCSD[a]	CCSD(T)-F12a[b]	M06-2X	BMC-CCSD[a]	CCSD(T)-F12a[b]			
300	38.56	38.51	38.74	40.40	40.35	40.28	39.61	39.86	39.32
400	49.52	49.49	49.62	50.90	50.87	50.98	50.37	50.42	50.67
500	59.85	59.84	59.93	60.42	60.40	60.46	60.12	60.07	60.66
600	68.83	68.83	68.90	68.55	68.55	68.59	68.47	68.33	69.19
800	83.11	83.12	83.18	81.47	81.46	81.49	81.58	81.43	82.60
1000	93.76	93.77	93.81	91.18	91.18	91.20	91.38	91.20	92.40
1500	110.28	110.28	110.31	106.46	106.47	106.48	106.66	106.40	108.03
2000	118.72	118.72	118.73	114.33	114.33	114.35			
2400	124.38	124.38	124.39	119.59	119.59	119.61			

[a]BMC-CCSD//M06-2X/MG3S.

[b]CCSD(T)-F12a/jul-cc-pVTZ//M06-2X/MG3S.

[c]Using Benson's data from Ref. 94.

Table 2.10 Standard-state entropy, enthalpy, and free energy changes of the isomerization reaction between *n*-heptane and isoheptane

T (K)	MS-LH			MS-T			Benson[c]	Exp.-API[d]	Exp.-TRC[e]
	M06-2X	BMC-CCSD[a]	CCSD(T)-F12a[b]	M06-2X	BMC-CCSD[a]	CCSD(T)-F12a[b]			
				ΔS^{o} (cal mol^{-1} K^{-1})					
298	−1.54	−1.45	−1.29	−1.55	−1.45	−1.30	−1.31	−1.89	−1.82
300	−1.53	−1.44	−1.29	−1.54	−1.45	−1.30	−1.31	−1.91	−1.82
400	−1.33	−1.29	−1.20	−1.38	−1.33	−1.25	−1.36	−1.42	−1.79
500	−1.21	−1.19	−1.13	−1.28	−1.26	−1.20	−1.36	−1.14	−1.70
600	−1.14	−1.13	−1.09	−1.23	−1.21	−1.17	−1.34	−0.79	−1.60
800	−1.08	−1.08	−1.05	−1.17	−1.17	−1.14	−1.28	−0.65	−1.51
1000	−1.06	−1.06	−1.04	−1.15	−1.16	−1.13	−1.25	−0.52	−1.20
1500	−1.05	−1.05	−1.04	−1.16	−1.17	−1.16	−1.19		−0.48
2000	−1.05	−1.05	−1.04	−1.18	−1.19	−1.18			
2400	−1.05	−1.05	−1.05	−1.18	−1.19	−1.18			
				ΔH (kcal/mol)					
298	−1.52	−1.96	−1.58	−1.52	−1.96	−1.58	−2.40	−1.71	−1.63
300	−1.51	−1.96	−1.58	−1.52	−1.96	−1.58		−1.72	−1.63
400	−1.44	−1.91	−1.55	−1.46	−1.92	−1.56	−2.42	−1.59	−1.60
500	−1.39	−1.87	−1.52	−1.42	−1.89	−1.54	−2.42	−1.46	−1.58
600	−1.35	−1.83	−1.50	−1.38	−1.86	−1.53	−2.40	−1.27	−1.53
800	−1.31	−1.80	−1.47	−1.35	−1.83	−1.51	−2.37	−1.02	−1.39
1000	−1.29	−1.78	−1.46	−1.33	−1.82	−1.50	−2.34	−1.04	−1.20
1500	−1.28	−1.77	−1.46	−1.34	−1.84	−1.53	−2.27		−0.24
2000	−1.28	−1.77	−1.47	−1.37	−1.87	−1.56			

2400	−1.29	−1.78	−1.48	−1.38	−1.88	−1.58			
				ΔG° (kcal/mol)					
298	−1.06	−1.53	−1.20	−1.05	−1.53	−1.20	−2.01	−1.15	−1.08
300	−1.05	−1.53	−1.20	−1.05	−1.53	−1.19		−1.15	−1.10
400	−0.91	−1.39	−1.07	−0.91	−1.39	−1.07	−1.87	−1.02	−0.91
500	−0.79	−1.27	−0.96	−0.77	−1.26	−0.94	−1.74	−0.89	−0.72
600	−0.67	−1.16	−0.85	−0.65	−1.14	−0.83	−1.60	−0.80	−0.57
800	−0.45	−0.93	−0.63	−0.41	−0.90	−0.59	−1.34	−0.50	−0.19
1000	−0.23	−0.72	−0.42	−0.18	−0.67	−0.37	−1.09	−0.52	0.02
1500	0.29	−0.20	0.10	0.40	−0.09	0.20	−0.48		0.48
2000	0.81	0.33	0.62	0.99	0.50	0.79			
2400	1.23	0.75	1.03	1.46	0.98	1.26			

[a]BMC-CCSD//M06-2X/MG3S.

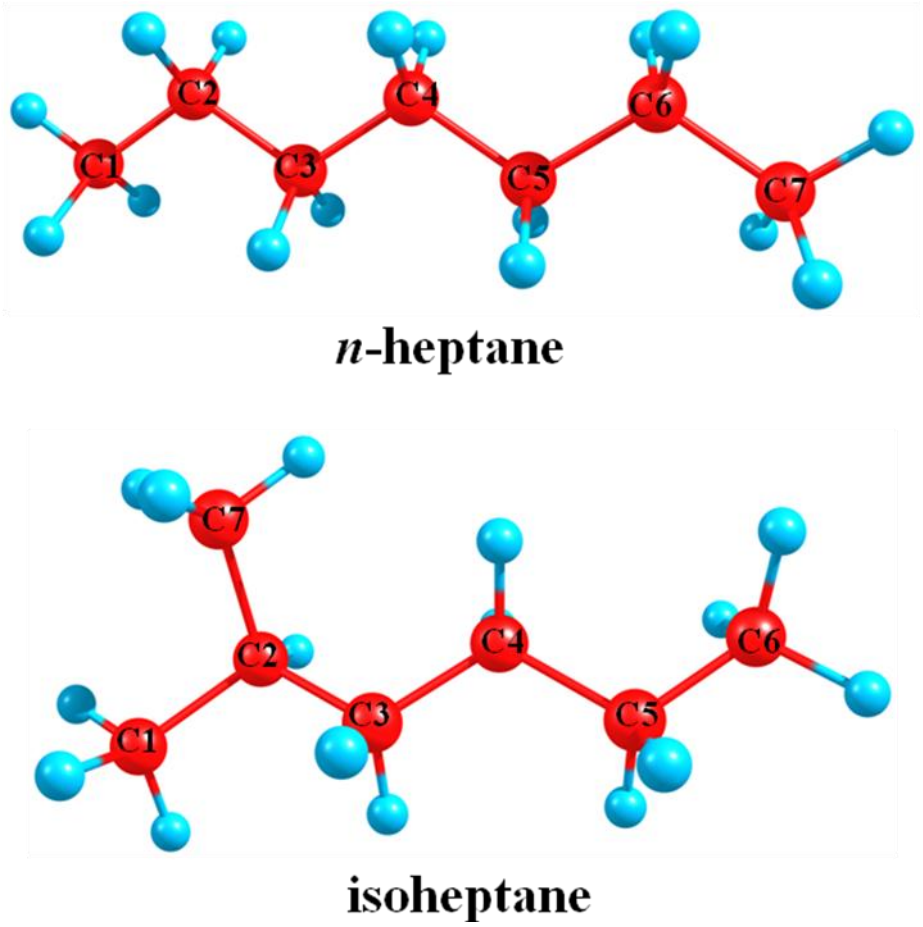

Figure 2.1 Numbering scheme for *n*-heptane and isoheptane.

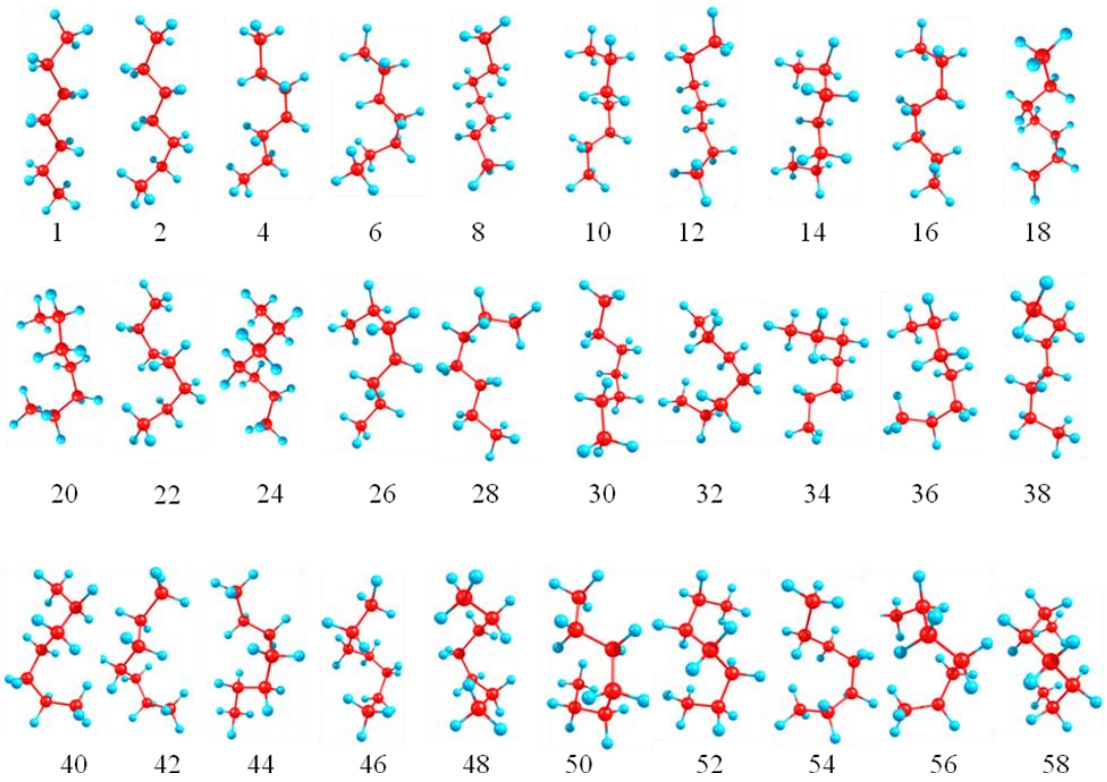

Figure 2.2 Structures of *n*-heptane. Note that all structures shown except structure 1 also have distinguishable mirror images.

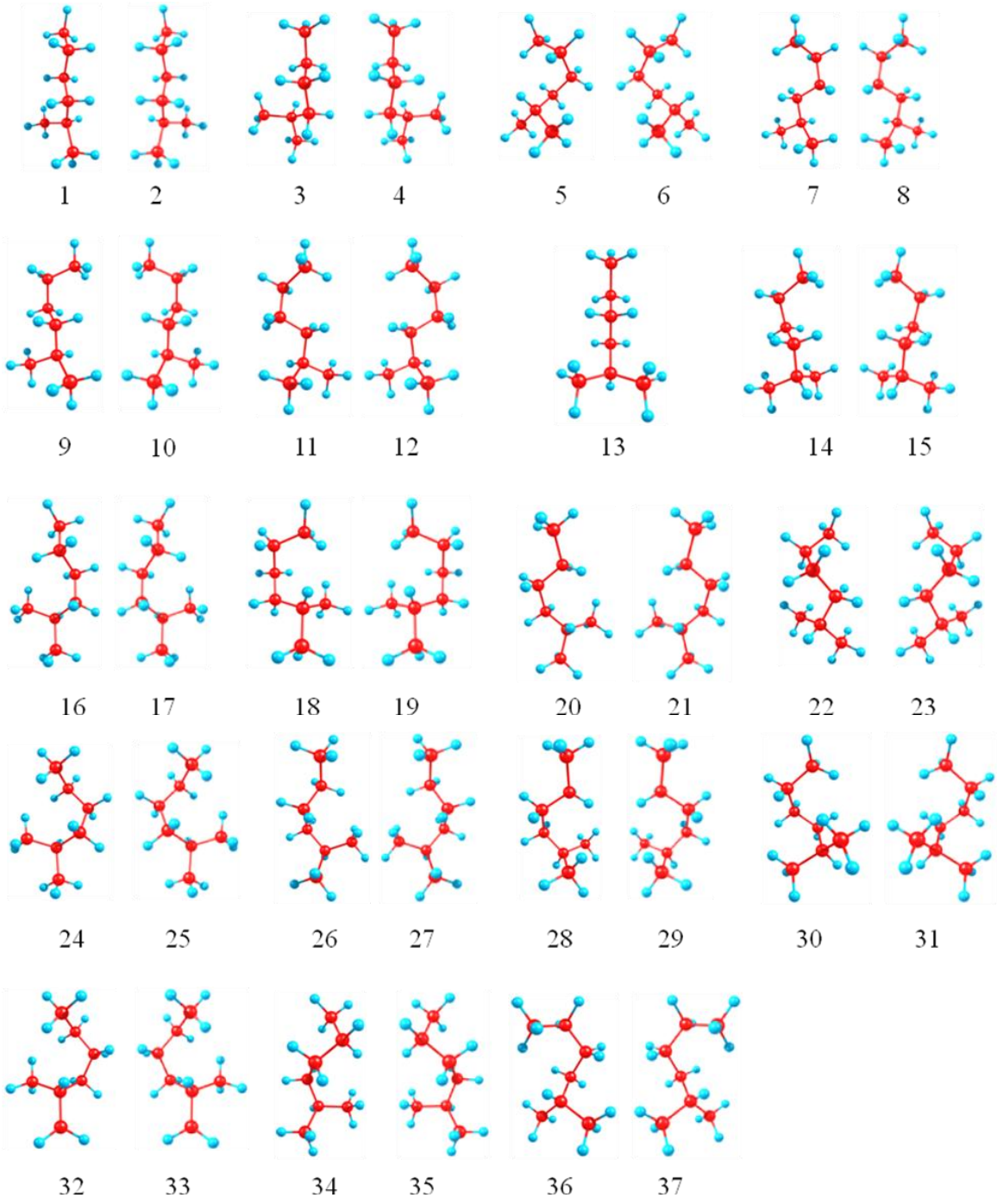

Figure 2.3 Structures of isoheptane. All structures occur in optically active pairs except structure 13.

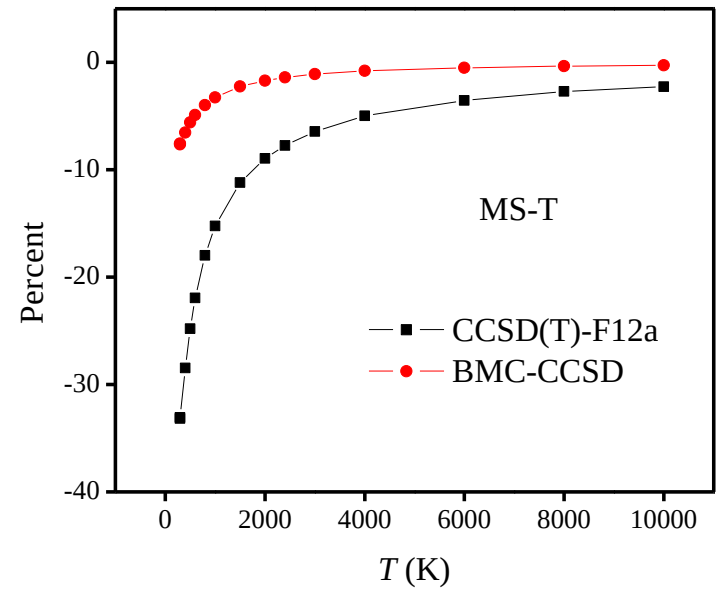

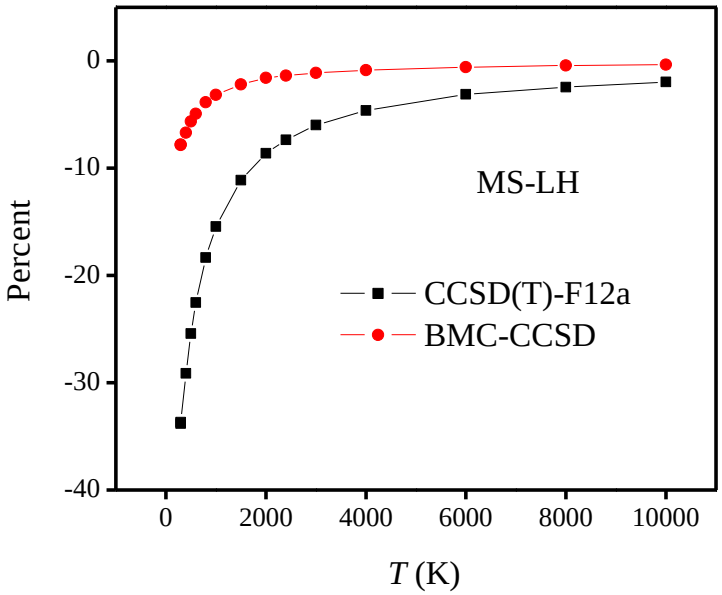

Figure 2.4 The percent deviations of partition functions of *n*-heptane between CCSD(T)-F12a and M06-2X results, and the percent deviations between BMC-CCSD and M06-2X results calculated by MS-LH and MS-T methods.

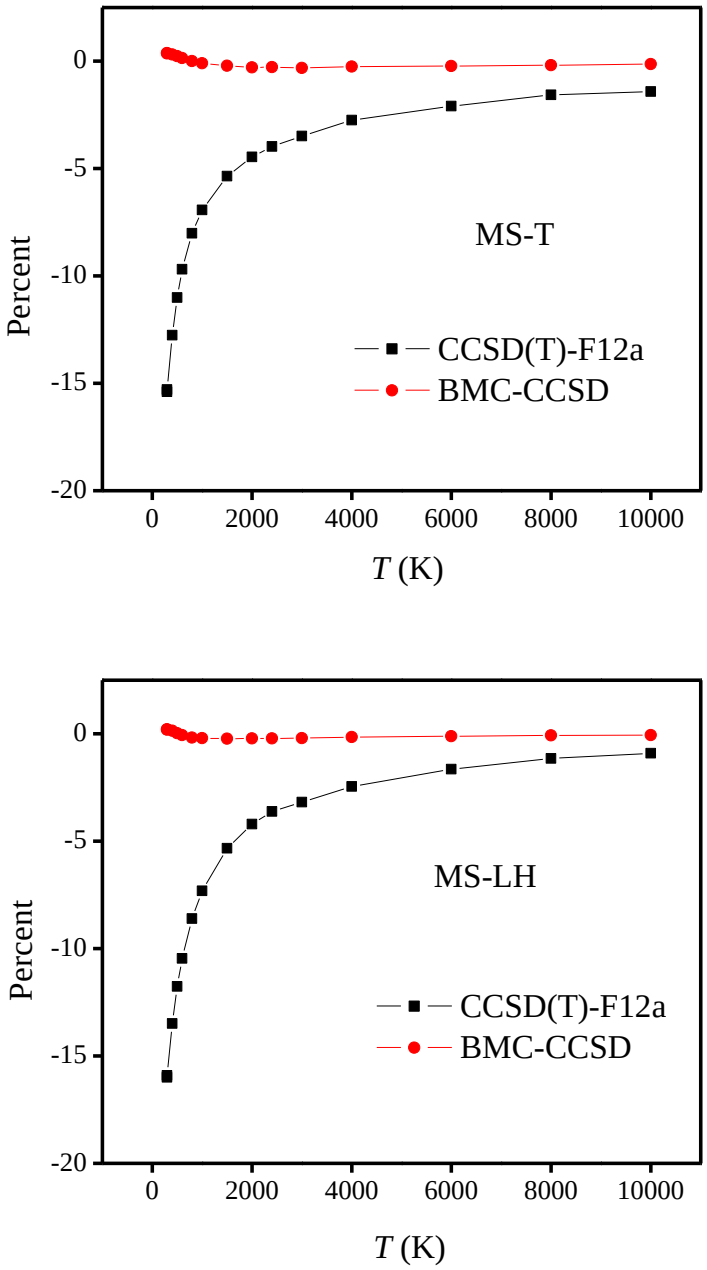

Figure 2.5 The percent deviations of partition functions of isoheptane between CCSD(T)-F12a and M06-2X results, and the percent deviations between BMC-CCSD and M06-2X results calculated by MS-LH and MS-T methods.

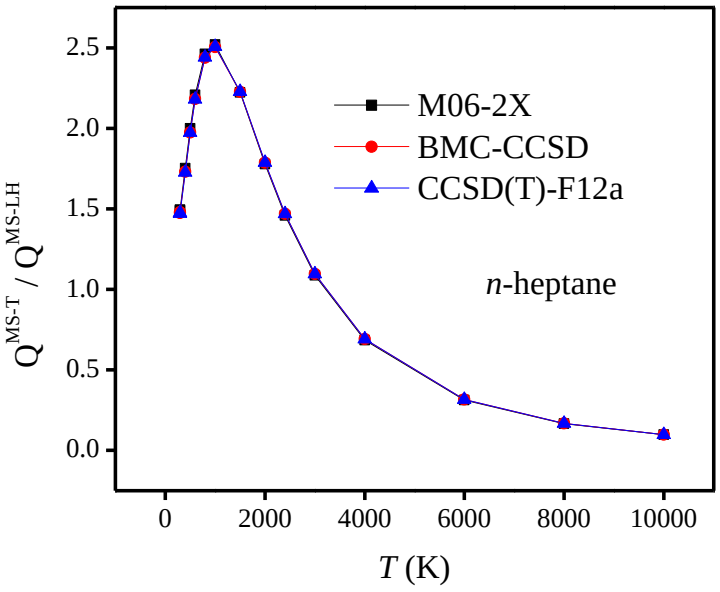

Figure 2.6 The ratio of partition functions of *n*-heptane calculated by MS-T and MS-LH approximations at various temperatures.

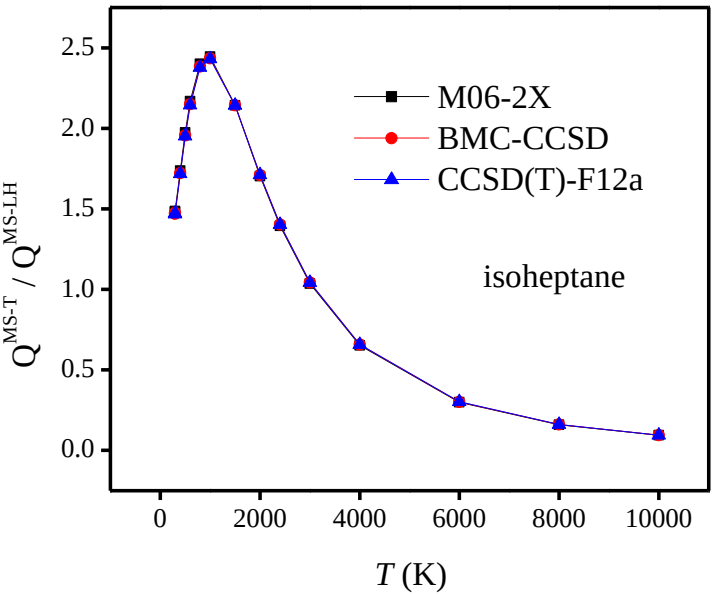

Figure 2.7 The ratio of partition functions of isoheptane calculated by MS-T and MS-LH approximations at various temperatures.

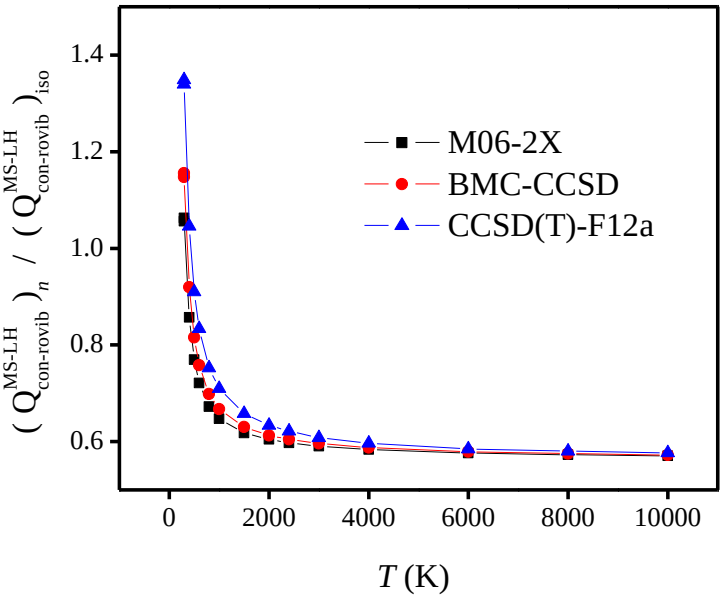

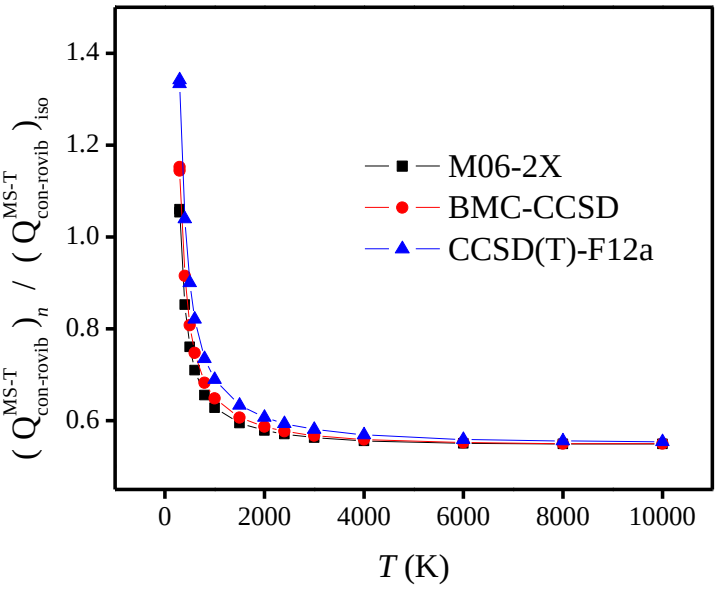

Figure 2.8 The ratio of partition functions of n-heptane over isoheptane calculated by MS-T and MS-LH approximations at various temperatures.

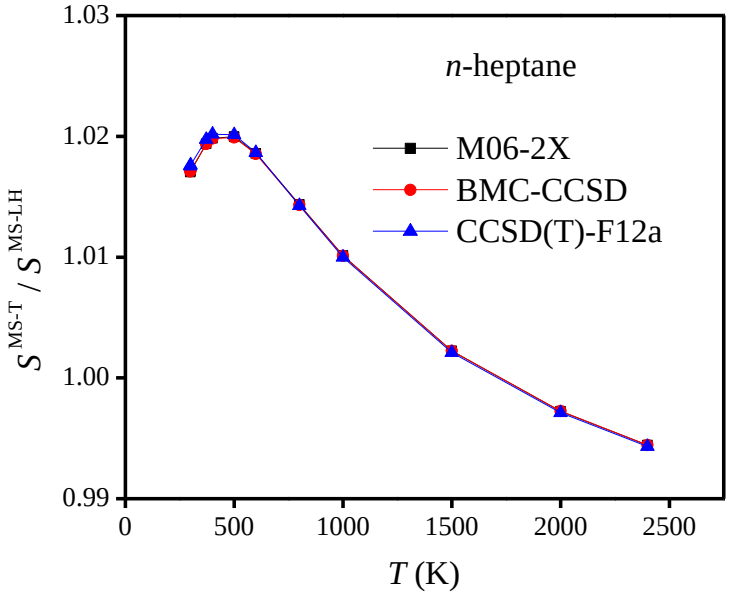

Figure 2.9 The ratio of entropies of *n*-heptane calculated by MS-T and MS-LH approximations at various temperatures.

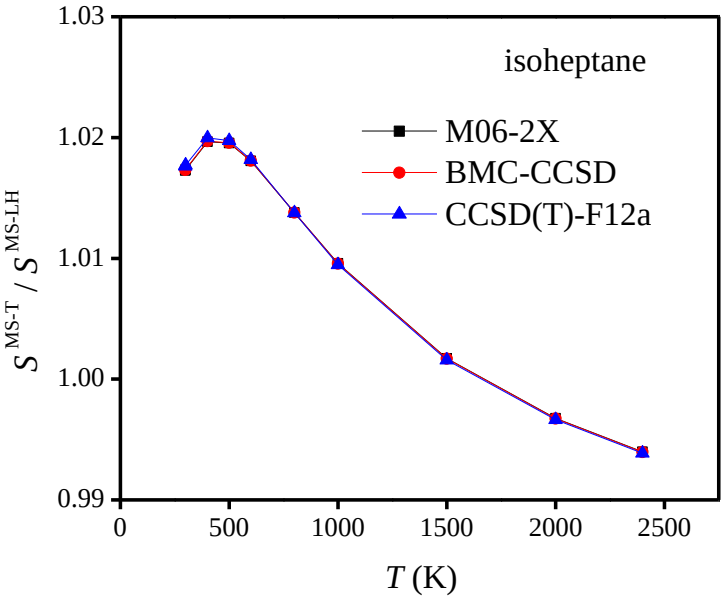

Figure 2.10 The ratio of entropies of isoheptane calculated by MS-T and MS-LH approximations at various temperatures.

Chapter 3. Multi-Structural Variational Transition State Theory. Kinetics of the 1,4-Hydrogen Shift Isomerization of the Pentyl Radical with Torsional Anharmonicity

1. Introduction

Combustion reactions of hydrocarbon fuels play a significant role as energy sources. However, the mechanisms of most combustion reactions have not been fully elucidated. This hampers the rational design of hydrocarbon fuels, and pollution and energy efficiency issues are not decided optimally. The situation is now being complicated by the use of biofuel additives. Therefore, understanding the kinetics of hydrocarbon combustion reactions is becoming more and more important; at the same time, computational chemistry is advancing to the stage where it has quantitative predictive capability for the reaction rates of complex species. This predictive capability is also important for other research areas involving gas-phase reactions of complex organic molecules, e. g., atmospheric chemistry. The goal of the work reported here is to develop and apply a more accurate method of calculating the rates of such reactions, in particular, reactions with potential energy barriers and multiple conformations of reactants, transition states, or both.

The 1,4-hydrogen shift isomerization reaction of 1-pentyl radical is a prototype for an important class of reaction in the combustion of hydrocarbons. Alkyl isomerization reactions have been investigated both experimentally[135–137] and computationally.[138] The first direct measurement of the 1,4-hydrogen shift isomerization of 1-pentyl was reported in 2002 by Miyoshi et al.[136] Hydrogen shift

reactions are expected to be dominated by tunneling contributions at 500 K and below. The evaluation of such contributions requires more global information about the potential energy surface than is required to evaluate the over-barrier contributions.

Computational modelling methods for the kinetics of complex reactions by direct-dynamics algorithms that include tunneling can be expensive when applied with reliable electronic structure methods because of the need to obtain Hessian information at least along a large portion of the minimum-energy reaction path[139] (MEP). Furthermore, when kinetics modeling is based on the harmonic-oscillator approximation, errors can accumulate from the anharmonic internal rotational motions (i.e., torsions) in complex molecules, especially at high temperature. The torsions can lead to multiple structures for the transition state. In the case at hand, the reactant 1-pentyl, the product 2-pentyl, and the saddle point all display multi-structural character due to internal rotation in reactants and products and pseudorotation in the transition state. The harmonic-oscillator approximation using only one structure to represent the critical configurations along the reaction path is inaccurate for rate-constant calculations; therefore a multi-structural approach is required.

In the present work, we propose an efficient method, based on either conventional transition state theory (TST)[140] or variational transition state theory (VTST),[106,140b,141] to compute high-pressure limit thermal rate constants of molecules with multi-structural anharmonicity and multidimensional tunneling, and we apply it to the 1,4-hydrogen shift reaction of 1-pentyl radical. In order to include tunneling for this hydrogen shift reaction, instead of applying expensive straight direct dynamics[142,143] calculations to obtain the reaction path and reaction path potential, we use the multi-

configuration Shepard interpolation (MCSI) method[144,145] to efficiently generate the potential energy surface from a small number of high-level electronic structure calculations. The M06 density functional[64,146] is used to optimize the geometry and compute the energies, gradients, and Hessians of stationary Shepard points (reactant well, product well, and saddle point), as well as non-stationary Shepard points along the reaction path. The Shepard-interpolated potential surface is used to compute the transmission coefficient by utilizing the multidimensional small-curvature tunneling (SCT) approximation.[147,148]

A key aspect of the present calculations is that we analyze all the different conformers (here called structures) of the critical configurations (1-pentyl, 2-pentyl, and the saddle point) that are generated by internal rotation or pseudorotation. For this purpose, the M06-2X density functional[64,146] is used to obtain all the structures. Then the conformational-vibrational-rotational partition function is calculated by the multi-structural all-structures[97] (MS-AS) and multi-structural reference-structure[97] (MS-RS) methods. The thermal rate constant over the temperature range 200–2000 K is evaluated by the POLYRATE program[149] employing a new formulation of VTST, called multi-structural variational transition state theory.

2. Theory

2.1. Rate constant

VTST has been widely applied to barrier reactions in the gas phase,[106,141,150,151] barrierless reactions in the gas phase,[152−154] and reactions at gas-solid interfaces,[155] in solids,[156] in liquid solutions,[157,158] and in enzymes,[159,160] and the most appropriate

formalism is different for each case.[161,162] In the present article we recognize a distinction between two kinds of gas-phase barrier reactions, which we may loosely categorize as small-molecule reactions and complex-molecule reactions. In the small-molecule case both the reactants and transition states have only one conformation or they have more than one conformer, but only one is low enough in energy to merit consideration or the others can be accounted for by a separable torsional anharmonicity approximation. An example with only one conformation for both reactant and transition state would be Cl•+ CH_4 → H• + CH_3Cl. The previous formulation[106,141,148,150,151,163−166] of VTST for gas-phase reactions with a barrier is applicable to this kind of case, and we label this formulation of VTST as single-structural VTST. An example of a complex reaction would be the case considered in this paper, namely the isomerization of 1-pentyl radical to 2-pentyl radical. Here the reactant has 15 distinguishable conformations, and the transition state has four. We label these conformations as "structures," and we here propose a multi-structural formulation of VTST theory that includes them. First we need to review single-structural VTST.

2.1.1. Single-structural VTST

In single-structural VTST as usually applied, the quasiclassical thermal rate constant of canonical variational theory (CVT: the formulation of VTST in which a best compromise transition state is found for each temperature) is[106,141,148,150,151,163−166]

$$k^{\mathrm{CVT}} = \min_{s} k^{\mathrm{GT}}(T,s) \qquad (1)$$

where s is the progress variable parametrizing a sequence of trial transition states, and k^{GT} is the generalized transition-state rate constant at temperature T for a transition

state at *s*; in practice we usually take *s* as the signed distance along the minimum-energy path (MEP), which is the path[139] of steepest descents in isoinertial coordinates from the saddle point down toward reactants joined at $s = 0$ to the path of steepest descents down toward products. By quasiclassical we mean that bound vibrations are quantized, but the motion along the reaction coordinate is classical. To include quantum effects on reaction coordinate motion (e.g., tunneling), we multiply by a transmission coefficient:

$$k^{\mathrm{CVT/T}} = \kappa(T) k^{\mathrm{CVT}}(T) \qquad (2)$$

where /T in a superscript denotes the inclusion of tunneling, and κ is the transmission coefficient.

The transmission coefficient that we usually use is called a ground-state (G) transmission coefficient,[150,165] and it is taken as ratio of the quantum mechanical thermally averaged flux through the ground-state level[167,168] of the transition state dividing surface divided by the same quantity computed with classical reaction coordinate motion. The quantity averaged in the divisor is equal to a Heaviside step function at the threshold energy implied by CVT; this threshold energy is the value of the vibrationally adiabatic ground-state potential energy curve[139,165] $V_{\mathrm{a}}^{\mathrm{G}}$ at the temperature-dependent CVT transition state, where

$$V_{\mathrm{a}}^{\mathrm{G}} = V_{\mathrm{MEP}}(s) + \varepsilon^{\mathrm{G}}(s) \qquad (3)$$

whereas V_{MEP} denotes the minimum potential energy of the transition state dividing surface at *s* relative to that of reactants, and ε^{G} denotes the local zero-point vibrational energy of the modes transverse to the reaction coordinate at *s*. Note that potential

energy is also called Born-Oppenheimer energy, classical energy, and zero-point-exclusive energy.

The other factor, k^{CVT}, in eq 2 is computed from eq 1, where the generalized transition state theory rate constant of eq 1 may be written as

$$k^{\mathrm{GT}} = \frac{1}{\beta h} \frac{Q_{\mathrm{el}}^{\mathrm{GT}}(T) Q_{\mathrm{rovib}}^{\mathrm{GT}}(T,s)}{Y(T) Q_{\mathrm{el}}^{\mathrm{R}}(T) Q_{\mathrm{rovib}}^{\mathrm{R}}(T)} \exp(-\beta V_{\mathrm{MEP}}(s)) \qquad (4)$$

where β is $(k_{\mathrm{B}}T)^{-1}$, k_{B} is Boltzmann's constant, h is Planck's constant, Q is a partition function, GT denotes a generalized transition state at location s along the reaction coordinate, R denotes reactant, "el" denotes electronic, "rovib" denotes rotational-vibrational, and

$$Y = \begin{cases} \Phi_{\mathrm{rel}}^{\mathrm{R}}(T) & \text{for biomolecular reactions} \\ 1 & \text{for unimolecular reactions} \end{cases} \qquad (5)$$

where $\Phi_{\mathrm{rel}}^{\mathrm{R}}$ is the relative transitional partition function of two reactants. Note that $Q_{\mathrm{rovib}}^{\mathrm{GT}}$ is missing a degree of freedom, in particular the reaction coordinate, which is the degree of freedom normal to the transition state dividing surface. In eq 4 the zero of energy for the reactant partition functions is the minimum potential energy of reactants (which we set to equal to zero by convention), not the reactant zero point level; and the zero of energy of $Q_{\mathrm{el}}^{\mathrm{GT}}$ and $Q_{\mathrm{rovib}}^{\mathrm{GT}}$ is at V_{MEP}, not at a zero point level. Finally note that all symmetry numbers for overall rotation are included in the rotational

partition functions.[169] Symmetry numbers for internal rotation are included in $Q_{\text{rovib}}^{\text{R}}$. Full details of eqs 1−5 are given elsewhere.[148,165,166]

Note that, when using eq 4, there are two approximations that can be employed to evaluate $Q_{\text{rovib}}^{\text{GT}}$ and $Q_{\text{rovib}}^{\text{R}}$. If neither the generalized TS nor the reactant include any torsional motion, $Q_{\text{rovib}}^{\text{GT}}$ and $Q_{\text{rovib}}^{\text{R}}$ are taken as a product of a rotational partition function and a vibrational one that can be calculated using the harmonic approximation. This will be called the SS-HO approximation, where SS denotes single-structural. If the generalized TS or the reactant includes any torsional mode, the corresponding partition functions should be calculated by using a single-structural torsional method proposed previously[13] or the one introduced below, called SS-T. The details of calculations using the SS-HO and SS-T approximations are presented in section 2 of Calculation Methods.

The theory reviewed above has usually just been labeled as VTST, although it will be labelled SS-VTST when we are specifically distinguishing it from the multi-structural generalization, which is presented next.

2.1.2. Multi-structural VTST

Note that eq 2 corresponds to minimizing the generalized free energy of activation.[106,141] For a multi-structural case we want a generalization where all quantities are computed along a single reaction path. We label the distinguishable saddle point structures as $c = 1, 2, \ldots, C$ (where C is the total number of the saddle point structures). Similarly we label the distinguishable structures of the reactants and products by $j = 1, 2, \ldots J$ (where J is the total number of reactant structures) and $l = 1, 2, \ldots, L$ (where L is the total number of product structures), respectively.

Correspondingly, U_j^{R} and U_l^{P} denote the potential energies of structures j and l with respect to the lowest-potential-energy structure of reactants, which is always numbered as $j = 1$; thus U_1^{R} is zero by definition. Also, we use the convention that the $l = 1$ structure is the lowest-potential-energy structure of products.

We choose the reaction path to be the MEP through the saddle point with lowest value of $V_{\mathrm{a}}^{\mathrm{G}}$ that connects reactants to products, and we label this structure with $c = c^*$. For a unimolecular reaction with a simple barrier and a single product, this MEP terminates at a reactant structure for negative s and at a product structure for positive s; we label these structures with j equal to j^* and l equal to l^*. (For a bimolecular reaction the MEP for negative s would terminate at a well in the entrance valley of the potential energy surface.) The potential energy relative to structure $j = 1$ as the reactant moves along the MEP that passes through structure c of the saddle point is called $V_{\mathrm{MEP},c}$. Then we replace eqs 1 and 4 by

$$k^{\mathrm{CVT}} = \min_s k^{\mathrm{MS\text{-}GT}}(T,s) \tag{6}$$

where

$$k^{\mathrm{MS\text{-}GT}} = \frac{1}{\beta h}\frac{Q_{\mathrm{el}}^{\mathrm{GT}}(T)Q_{\mathrm{con\text{-}rovib}}^{\mathrm{GT}}(T,s)}{Y(T)Q_{\mathrm{el}}^{\mathrm{R}}(T)Q_{\mathrm{con\text{-}rovib}}^{\mathrm{R}}(T)}\exp(-\beta V_{\mathrm{MEP},c^*}(s)) \tag{7}$$

where $Q_{\mathrm{con\text{-}rovib}}^{\mathrm{X}}$, with X = GT or R, denotes a conformational-rotational-vibrational partition function (as in section 1.1, it is missing a degree of freedom when X = GT); $Q_{\mathrm{el}}^{\mathrm{R}}$ and $Q_{\mathrm{con\text{-}rovib}}^{\mathrm{R}}$ have their zero of energy at the lowest potential energy of the $j = 1$

structure of the reactant, and $Q_{\mathrm{el}}^{\mathrm{GT}}$ and $Q_{\mathrm{con\text{-}rovib}}^{\mathrm{GT}}$ have their zero of energy at the *s*-dependant V_{MEP,c^*} .

For reactants we have

$$Q_{\mathrm{con\text{-}rovib}}^{\mathrm{R}} = \sum_{j=1}^{J} Q_{\mathrm{rovib},j}^{\mathrm{R}} \exp(-\beta U_j^{\mathrm{R}}) \tag{8}$$

For the generalized transition state we approximate $Q_{\mathrm{con\text{-}rovib}}^{\mathrm{GT}}$ as the *s*-dependent rotational-vibrational partition function of the structure $c = c^*$ (computed just as $Q_{\mathrm{rovib}}^{\mathrm{GT}}$ for eq 4) times the ratio of the multi-structural result to the single-structural result at the saddle point, which is denoted ‡. This yields

$$Q_{\mathrm{con\text{-}rovib}}^{\mathrm{GT}} = Q_{\mathrm{rovib},c^*}^{\mathrm{GT}}(T,s) F_{\mathrm{MS}}^{\ddagger}(T) \tag{9}$$

where

$$F_{\mathrm{MS}}^{\ddagger} = \frac{Q_{\mathrm{con\text{-}rovib}}^{\ddagger}(T)}{Q_{\mathrm{rovib},c^*}^{\ddagger}(T)} = \frac{\sum_{c=1}^{C} Q_{\mathrm{rovib},c}^{\ddagger}(T) \exp[-\beta(V_c^{\ddagger} - V_{c^*}^{\ddagger})]}{Q_{\mathrm{rovib},c^*}^{\ddagger}(T)} \tag{10}$$

where $V_c^{\ddagger}$ denotes the potential energy of saddle point structure *c* with respect to the potential energy of the lowest-energy structure, *j* = 1, of the reactant, and $Q_{\mathrm{rovib},c}^{\ddagger}$ has its zero of energy at $V_c^{\ddagger}$. Note that $V_{c^*}^{\ddagger}$ is not necessarily the lowest-energy saddle point energy.

For computational purposes, we rewrite the generalized transition-state theory rate constant of eq 6 as

$$k^{\text{MS-CVT}} = F^{\text{MS}}(T) k_{1,c^*}^{\text{SS-CVT}}(T) \tag{11}$$

where

$$k_{j,c}^{\text{SS-CVT}} = \min_{s} k_{j,c}^{\text{SS-GT}}(T, s) \tag{12}$$

where $k_{j,c}^{\text{SS-GT}}$ and $k_{j,c}^{\text{SS-CVT}}$ are respectively the single-structural generalized transition state rate constant and the single-structural CVT rate constant computed using the MEP through structure c of the saddle point and using structure j for reactants. Note that eq 11 corresponds to $j = 1$ and $c = c^*$. Comparing eqs 11 and 12 to eqs 6−10 yields

$$F^{\text{MS}} = \frac{F_{\text{MS}}^{\ddagger}(T)}{F_{\text{MS}}^{\text{R}}(T)} \tag{13}$$

where

$$F_{\text{MS}}^{\text{R}} = \frac{Q_{\text{con-rovib}}^{\text{R}}(T)}{Q_{\text{rovib},1}^{\text{R}}(T)} \tag{14}$$

2.2. Transmission coefficient

Equation 2 is used for the transmission coefficient for either the single-structural case of eq 1 or the multi-structural case of eq 6. In either case one uses the MEP through the saddle point with the lowest V_{a}^{G} that connects reactants to produces, and

$\kappa^{\mathrm{CVT/T}}$ is the ratio of a thermally averaged approximate quantal transmission probability divided by a thermally averaged quasiclassical one.[148,165,166]

2.3. Vibrational anharmonicity

When using eqs 8, 9, 10, 13, and 14, $Q^{\mathrm{GT}}_{\mathrm{con\text{-}rovib}}$, $Q^{\ddagger}_{\mathrm{con\text{-}rovib}}$, and $Q^{\mathrm{R}}_{\mathrm{con\text{-}rovib}}$ can be calculated by using the recently proposed[15] internal-coordinate multi-structural approximation in either its full version, called the multi-structural-all-structures (MS-AS) approximation, or its more practical version, called the multi-structural reference-structure (MS-RS) approximation. When employing MS-AS calculations, we denote such partition functions as $Q^{\mathrm{MS\text{-}AS,R}}_{\mathrm{con\text{-}rovib}}$ and $Q^{\mathrm{MS\text{-}AS,}\ddagger}_{\mathrm{con\text{-}rovib}}$. Similarly we denote the reactant and transition state partition functions as $Q^{\mathrm{MS\text{-}RS,R}}_{\mathrm{con\text{-}rovib}}$ and $Q^{\mathrm{MS\text{-}RS,}\ddagger}_{\mathrm{con\text{-}rovib}}$ when using the MS-RS method. Then eqs 10, 11, 13, and 14 can be rewritten as

$$F^{\ddagger}_{\mathrm{MS\text{-}X}} = \frac{Q^{\mathrm{MS\text{-}X,}\ddagger}_{\mathrm{con\text{-}rovib}}}{Q^{\ddagger}_{\mathrm{rovib},c^*}(T)} \tag{15}$$

$$F^{\mathrm{R}}_{\mathrm{MS\text{-}X}} = \frac{Q^{\mathrm{MS\text{-}X,\,R}}_{\mathrm{con\text{-}rovib}}}{Q^{\mathrm{R}}_{\mathrm{rovib},1}(T)} \tag{16}$$

$$k^{\mathrm{MS\text{-}CVT}} = F^{\mathrm{MS\text{-}X}}(T) k^{\mathrm{SS\text{-}CVT}}_{1,c^*}(T) \tag{17}$$

$$F^{\mathrm{MS\text{-}X}} = \frac{F^{\ddagger}_{\mathrm{MS\text{-}X}}(T)}{F^{\mathrm{R}}_{\mathrm{MS\text{-}X}}(T)} \tag{18}$$

where X could be either AS or RS.

In addition, in the present article we consider two versions of the MS-AS and MS-RS approximations. The first versions are the MS-AS-HO and MS-RS-HO, which

treat the included structures harmonically. This includes multi-structural anharmonicity (which is the difference between the MS-AS-HO or MS-RS-HO result and the single-structural HO result) but not torsional, bend, or stretch anharmonicity. The second versions are called MS-AS-T and MS-RS-T, where T denotes torsional anharmonicity, and it is reviewed in section 2 of Calculation Method.

We note that the MS-AS-T and MS-RS-T methods explicitly include only multi-structural and torsional anharmonicity. However other forms of anharmonicity can be included implicitly by using scale factors for vibrational frequencies or by, for example, using the Morse approximation for stretches[164] and the quadratic-quartic[170,171] approximation for bends. In the present article we make the former choice, i. e., scaling.

3. Calculation Methods

3.1. Electronic Structure Calculations

The M06-2X density functional with the 6-311+G(2df,2p) basis set[66,67,108] was applied to optimize the geometry and obtain the frequency for all the conformers of the reactant 1-pentyl radical, the product 2-pentyl radical, and the transition state. These structures are generated by internal rotation around C−C bonds or by pseudorotation of the ring. The 6-311+G(2df,2p) basis set for H and C is also called MG3S, and we will use the short name for brevity.

For the global minimum conformers of 1-pentyl, 2-pentyl, and the transition state, the M06, M06-2X, and M08-SO[172] density functionals were used to optimize the geometries of reactants, products, and transition states to obtain the reaction energies and barrier heights. In addition, two multilevel methods, BMC-CCSD[110] and MCG3-

TS,[173] and the ab initio CCSD(T)-F12b[111,112] method were used to calculate single-point energies at the M06-2X and M08-SO stationary points.

In addition to the already mentioned MG3S basis set, several other basis sets were also utilized for the electronic structure calculations, including 6-31+G(d,p),[63] maug-cc-pVTZ,[174] aug-cc-pVTZ,[175] jul-cc-pVTZ[113] and def2-TZVP.[176] The M06 and M06-2X density functional calculations were performed by using the *Gaussian 09* program,[68] and the M08-SO density functional calculations were carried out via *Gaussian* 03 locally modified by MN-GFM-4.1.[177] CCSD(T)-F12a calculations were performed using MOLPRO;[115] and the BMC-CCSD and MCG3-TS calculations were carried out using MLGAUSS2.0.[114] The integration grid employed for density functional calculations of frequencies had 99 radial shells and 974 angular points per shell. The frequencies used for the partition function and $F^{\text{MS-X}}$ calculations in sections 2 and 4 of Calculation Methods are obtained by using M06-2X/MG3S density functional calculations and multiplying the directly calculated values by an empirical frequency scaling factor[69] of 0.970.

3.2. The conformational-vibrational-rotational partition function calculations

The most structurally complete conformational-vibrational-rotational partition functions were calculated by the MS-AS method[97] mentioned above; in the MS-AS-HO and MS-AS-T version of this method we have

$$Q_{\text{con-rovib}}^{\text{MS-AS-HO}} = \sum_{j=1}^{J} Q_{\text{rot},j} \exp\left(-\beta U_j\right) Q_j^{\text{HO}} \qquad (19)$$

and

$$Q_{\text{con-rovib}}^{\text{MS-AS-T}} = \sum_{j=1}^{J} Q_{\text{rot},j} \exp\left(-\beta U_j\right) Q_j^{\text{HO}} Z_j \prod_{\tau=1}^{t} f_{j,\tau} \qquad (20)$$

where $Q_{\text{rot},j}$ is the rotational partition function of structure *j*, Q_j^{HO} is the usual normal-mode harmonic oscillator vibrational partition function calculated at structure *j*, Z_j is a factor designed to ensure that the MSTor scheme reaches the correct high-*T* limit (within the parameters of the model), and $f_{j,\tau}$ is an internal-coordinate torsional anharmonicity function that, in conjunction with Z_j, adjusts the harmonic partition function of structure *j* for the presence of the torsional motion τ. As mentioned in section 1 of Calculation Methods, frequencies used for Q_j^{HO}, Z_j, and $f_{j,\tau}$ calculations were scaled by an empirical frequency scaling factor.[69] We use the label MS-AS-HO to denote the partition function calculated without Z_j and $f_{j,\tau}$, that is, with all Z_j and all $f_{j,\tau}$ equal to unity. When using either the MS-AS-HO or the MS-AS-T version of the MS-AS method, it is not necessary to assign each torsional motion to a specific normal mode. The MS-AS-T approximation reduces to the MS-AS-HO approximation in the low-temperature limit, and it approaches the free-rotor result in the high-temperature limit. The Z_j and $f_{j,\tau}$ factors are designed to interpolate the partition function between these limits in the intermediate temperature range. In principle, more accurate interpolations could be carried out[97] if one calculated the barrier heights for torsional motions that interconvert the reactant structures with one

another and the transition state structures with one another, but an advantage of the method employed here is that we forego this expensive step in present application.

In the notation of Ref. 97, we assume, when applying the MS-AS-T method, that some of the torsions are strongly coupled, as
specified further in section 4 of Results and Discussion. We use eqs 19 and 20 to obtain the conformational-vibrational-rotational partition functions for the reactant, transition state, and product, labeled as, $Q_{\text{con-rovib}}^{\text{MS-AS-X, R}}$, $Q_{\text{con-rovib}}^{\text{MS-AS-X, ‡}}$, and $Q_{\text{con-rovib}}^{\text{MS-AS-X, P}}$, respectively, where X is either HO or T.

Note that if one includes only a single conformer in eqs 19 and 20, that is, if J equals one, the corresponding equations reduce to

$$Q_{\text{rovib}}^{\text{SS-HO}} = Q_{\text{rot},1} Q_{\text{vib}}^{\text{HO}} \tag{21}$$

and

$$Q_{\text{rovib}}^{\text{SS-T}} = Q_{\text{rot},1} Q_{\text{vib},1}^{\text{HO}} Z_1 \prod_{\tau=1}^{t} f_{1,\tau} \tag{22}$$

which can be used to calculate the SS-HO and SS-T partition functions for the SS-VTST calculations reviewed in Theory section 1.1.

We also calculated the conformational-vibrational-rotational partition functions by the MS-RS-HO and MS-RS-T methods.[97] These methods include only the structures that can be obtained by a one-at-a-time torsion from a reference structure. This restriction yields[15]

$$Q_{\text{con-rovib}}^{\text{MS-RS-HO}} = Q_{\text{rovib}}^{\text{SS-HO}} \prod_{\tau=1}^{t} \sum_{i(\tau)=1}^{P_{1,\tau}} \frac{Q_{j[\tau,i(\tau)]}^{\text{IT-HO}}}{Q_{j=1}^{\text{IT-HO}}} \tag{23}$$

$$Q_{\text{con-rovib}}^{\text{MS-RS-T}} = Q_{\text{rovib}}^{\text{SS-T}} \prod_{\tau=1}^{t} \sum_{i(\tau)=1}^{P_{1,\tau}} \frac{Q_{j[\tau,i(\tau)]}^{\text{IT-T}}}{Q_{j=1}^{\text{IT-T}}} \tag{24}$$

where

$$Q_j^{\text{IT-HO}} = Q_{\text{rot},j} \exp(-\beta U_j) Q_{\text{vib},j}^{\text{HO}} \prod_{\tau'=1}^{t} P_{j,\tau} \tag{25}$$

$$Q_j^{\text{IT-T}} = Q_{\text{rot},j} \exp(-\beta U_j) Q_{\text{vib},j}^{\text{HO}} Z_j \prod_{\tau'=1}^{t} P_{j,\tau} f_{j,\tau} \tag{26}$$

where we use $j = 1$ as the reference structure. The $P_{j,\tau}$ factor in eqs 25 and 26 denotes the number of distinguishable minima along torsion τ in structure *j*.

3.3. Transmission coefficient calculation using the MCSI algorithm

The transmission coefficient κ(T) that incorporates the tunneling for the hydrogen shift reaction was evaluated using the small-curvature tunneling approximation[147] (SCT). The MEP and ground-state vibrationally adiabatic potential curve (V_a^G) were obtained by the MCSI method[144,145,178−182] using the MCSI[183] and MC-TINKERATE[184] programs. Although the reactant, product, and the transition state all have a multi-structural character, we only need one structure of each to do MCSI calculations. We always use the transition state structure c^* with the lowest V_a^G as the saddle point to determine the V_{MEP} and V_a^G curves in the MCSI calculations. We choose the two structures, j^* and l^*, that are connected to the transition state c^* as the reactant and product wells, respectively, in the MCSI interpolation of the potential energy surface; and they were determined by following the paths of steepest descent.

To build the potential energy surface by the MCSI method, nine electronic-structure Shepard points were used. All the information about Shepard points, namely energies, gradients, and Hessians, was obtained by M06/6-31+G(d,p) calculations. The first Shepard point was placed at the saddle point c^* as optimized by M06/6-31+G(d,p). The six non-stationary Shepard points were placed close to the minimum energy reaction path (MEP) using a similar strategy to that in a previous paper[47] and they were at the following locations: 6.91, 12.21, and 17.30 kcal/mol below the saddle point on the 1-pentyl radical side and 6.26, 14.03, 19.96 kcal/mol below the saddle point on the 2-pentyl radical side. The final two Shepard points are the reactant well and product well structures, j^* and l^*, mentioned at the end of the previous paragraph.

The MCSI method involves interpolating the off-diagonal element of a diabatic potential matrix[178,185] where the diagonal elements are given by molecular mechanics. We use the MM3 method[186−188] for the molecular mechanics. It was found that using a Morse potential for the C−H bond in the MM3 force field for the Shepard interpolation provided smoother V_a^G curves than using quadratic stretch potentials, and so we used Morse stretches in all MM3 calculations. The parameters are: bond energy: 98 kcal/mol;[189] bond length: 1.12 angstrom;[186-188] and force constant: 4.74 N/cm.[186-188]

As discussed in the previous work,[180,182] we used three different internal coordinate sets for MCSI calculations: set q for molecular mechanics calculations, set r for Shepard interpolation, and set s to calculate the Shepard weighting function. In the present work, the set q is the standard set of MM3 internal coordinates, the set r consists of 42 nonredundant internal coordinates (15 bond distances, 20 bond angles, and 7

dihedral angles), and the set s consists of three intra-atomic distances shown in Figure 3.1.

3.4. Thermal rate constant calculation

All rate constant calculations were carried out using the MC-TINKERATE[184] and POLYRATE[149,190] programs. All multi-structural anharmonicity calculations are carried out using MSTor program.[116] First the single-structural CVT[150,151] forward rate constant using harmonic approximation is calculated by eq 12. Here the transition state and reactant well are $c = c^*$, and $j = j^* = 1$, which are the same structures used in the MCSI calculations in section 3 of Calculation Methods, since $j^* = 1$ in the present work. We label the single-structural CVT forward rate constant as $k^{\text{SS-CVT}}$.

In the next step we carry out the calculations on $F^{\ddagger}_{\text{MS-X}}$ and $F^{\text{R}}_{\text{MS-X}}$ (X = AS-T or RS-T) using eqs 15 and 16. The final thermal rate constant was determined by equation 27

$$k^{\text{MS-CVT/SCT}} = \kappa^{\text{SCT}}(T) F^{\text{MS-X}}(T) k^{\text{SS-CVT}}(T) \qquad (27)$$

where the transmission coefficient κ^{SCT} was calculated as presented in section 3 of Calculation Methods, and $F^{\text{MS-X}}$ is defined in eq 18.

Because we use the SCT approximation[147,148,190] for the ground-state transmission coefficient, the MS-CVT/T rate constant may be labeled $k^{\text{MS-CVT/SCT}}$.

The thermal reverse rate constant is calculated by using the partition function of the product instead of that of the reactant. The ratio of forward to reverse rate constant gives the equilibrium constant.

3. Results and Discussion

3.1. Structures, energies, and conformational-vibrational-rotational partition functions of reactant, product, and saddle point

Table 3.1 lists the zero-point-exclusive barrier heights and energies of reaction for the 1,4-hydrogen shift isomerization reaction of 1-pentyl radical calculated by various theoretical levels. The CCSD(T)-F12b−jul-cc-pVTZ//M06-2X/MG3S (our best estimate), BMC-CCSD//M06-2X/MG3S, and MCG3-TS//M06-2X/MG3S methods agree very well with each other. However, the M06-2X and M08-SO density functionals with the 6-31+G(d,p), MG3S, maug-cc-pVTZ, aug-cc-pVTZ, and def2-TZVP basis sets predict larger barrier heights. It is found that the M06 functional with the 6-31+G(d,p) basis gives results reasonably close to the CCSD(T)-F12b/jul-cc-pVTZ//M06-2X/MG3S calculation. Therefore, we chose M06/6-31+G(d,p) for the single-structural components of the kinetics calculation, that is, to calculate $k^{\text{SS-CVT}}$ and κ^{SCT}. However we expect M06-2X/MG3S to be more accurate for conformational energy differences, so we calculated $F^{\text{MS-X}}$ based on M06-2X/MG3S results.

Based on M06-2X calculations, 1-pentyl radical, 2-pentyl radical, and the transition state have 15, twelve, and four distinguishable structures, respectively (Figure

3.2). The five carbon atoms in the molecule (1-pentyl and 2-pentyl) are numbered as: H2C(1)–H2C(2)–H2C(3)–H2C(4)–H3C(5) and H3C(1)–H2C(2)–H2C(3)–HC(4)–H3C(5). In the 1-pentyl and 2-pentyl radicals, there exist four torsions, which are around the C(1)–C(2), C(2)–C(3), C(3)–C(4), and C(4)–C(5) bonds. Table 3.2 and Figure 3.2 show the naming convention that is used for labeling of the structures. For instance, "**1a^{+}g^{-}t**" means the conformer of 1-pentyl radical with the first, second, and third dihedral angles in the ranges of 140 to 163, −85 to −55 and −173 to 173 degrees, respectively, and "**2g^{-}a^{+}**" means the conformer of 2-pentyl radical with the first and second dihedral angles in the ranges of −85 to −55 and 140 to 172 degrees, respectively. The numbering of the structures is specified in Table 3.3.

In 1-pentyl radical, the torsional motion around the C(1)–C(2), C(2)–C(3), and C(3)–C(4) bonds can contribute to generate distinguishable conformers, and there are 15 structures. However in the 2-pentyl radical, the C(1) and C(5) tails in the molecule are both methyl groups, whose internal rotations do not generate distinct structures. Therefore, only the torsional motions around C(2)–C(3) and C(3)–C(4) bonds produce distinguishable conformers, and there are twelve structures. The transition state structures (Figure 3.2(c)) contain a relatively rigid five-membered-ring and a methyl tail group. The ring-structure character reduces the number of conformers to four (two pairs of mirror images). Unlike the structures of 1-pentyl and 2-pentyl, these transition state structures are not connected with each other through torsion motions around C–C bonds; rather they are connected by pseudorotation, as in cycloalkanes.

The multi-structural character of these critical configurations on the potential surface makes the kinetics of the reaction complex. In Theory and Calculation Methods

sections, we presented a practical way to calculate the rate constants while calculating only a single reaction path based on that the saddle point with the lowest zero-point-inclusive energy. We found that this structure is the **TS-1** structure, which is $c^* = 1$; and the reactant and product wells connected with **TS-1** are **1a**$^+$**g**$^-$**t** ($j^* = 1$) and **2g**$^-$**a**$^+$ ($l^* = 1$), respectively.

The next step is to calculate the partition functions of 1-pentyl, 2-pentyl and the transition state. The difficulty comes from treating this multi-structural character and torsional anharmonicity correctly. In literature, such as Sharma, Green[191] and Van Speybroeck[25] et al, torsional issues were treated by approximations based on hindered-rotor model. But these approximations either assume a one-to-one correspondence between torsions and individual normal modes[191] or require high-dimensional rotational potential surfaces.[191,25] In the present work, the torsions between C(1)–C(2) and C(2)–C(3) in 1-pentyl are strongly coupled, and assigning the torsions to specific normal modes is impossible. The new method MS-AS-T and MS-RS-T approximations that apply internal coordinate correction factors to the harmonic treatments thus can treat the coupled torsions properly.[97]

We employed eqs 21 and 22 to calculate the partition functions of the structures **TS-1**, **1a**$^+$**g**$^-$**t**, and **2g**$^-$**a**$^+$ using the SS-HO and SS-T approximations, respectively. The conformational-rovibrational partition functions of 1-pentyl, 2-pentyl, and their transition state were evaluated by both the MS-AS-X and MS-RS-X (X = HO or T) methods[97,116] using eqs 19−26 reviewed in section 2 of Calculation Methods. The MS-AS-T and MS-RS-T approximations provide more accurate partition functions than either the single-structural or MS-AS-HO and MS-RS-HO approximations. Tables 3.4,

3.5, and 3.6 list information for each structure of the 1-pentyl radical, 2-pentyl radical, and transition state that is used for the partition function calculations carried out by the MSTor program.[69] All the calculated partition functions are given in Tables 3.7−3.9.

First we discuss the MS-AS-T calculations for the 1-pentyl radical, 2-pentyl radical, and the transition state. There are four torsions in 1-pentyl and 2-pentyl radicals. For 1-pentyl, two of the torsions around the C(1)–C(2) and C(2)–C(3) bonds are involved in a strongly coupled[97] (SC) group; the other two torsions, around C(3)–C(4) and C(4)–C(5) bonds are considered to be nearly separable[97] (NS). For 2-pentyl, the torsions around the C(2)–C(3) and C(3)–C(4) bonds are treated as a strongly coupled (SC) group; the other two torsions, around the C(1)–C(2) and C(4)–C(5) bonds, are considered to be nearly separable (NS). Tables 3.7 and 3.8 give the conformational-vibrational-rotational partition functions of the 1-pentyl and 2-pentyl radicals using NS:SC =2:2. In the transition state, there is only one torsion around the bond between the methyl group and the five-membered ring. The conformational-vibrational-rotational partition functions are given in Table 3.9.

Tables 3.7−3.9 show that at low temperature (200−250 K), the differences of the partition functions calculated by the multi-structural-all-structure harmonic-oscillator method (MS-AS-HO) and MS-AS-T for 1-pentyl and the transition sate are within 6−19%. For 2-pentyl, the deviations are larger, 31−33%. As the temperature increases, the MS-HO approximation changes from being an underestimate to being an overestimate. By 2400 K, the MS-AS-HO results overestimate the MS-AS-T ones by 102% for 1-pentyl, 7% for the transition state, and 118% for 2-pentyl. We will use the more accurate MSTor method for the final kinetics calculations.

Next we discuss the MS-RS-T calculations for the 1-pentyl and 2-pentyl radicals (The transition state conformers are not generated by torsions; thus MS-RS is considered to be the same as MS-AS for the TS partition function calculations on the reaction considered in this paper.).When employing the MS-RS method, we need to identify all structures obtained by independent internal rotations from a reference structure. In this work, we use the global minimum structures **1a^{+}g^{-}t** and **2g^{-}a^{+}** as the reference structures for 1-pentyl and 2-pentyl radicals, respectively. For 1-pentyl, the internal rotation around the C(1)–C(2) bond in the reference structure **1a^{+}g^{-}t** does not generate any distinguishable structures, but the independent rotations around the C(2)–C(3) and the C(3)–C(4) bonds produce the other four structures used in the MS-RS calculations. They are **1a^{-}g^{+}g^{+}**, **1a^{-}g^{+}g^{-}**, **1a^{-}tt**, and **1a^{-}g^{+}t**. For 2-pentyl, independent rotations around the C(2)–C(3) and the C(3)–C(4) bonds in the reference structure **2g^{-}a^{+}** generate the other four structures: **2g^{+}a^{-}, 2ta^{+},2g^{-}g^{-}, and 2g^{-}s**. The detailed information about each structure of the 1-pentyl and 2-pentyl radicals used for MS-RS calculation are listed in the Electronic Supplementary Information , and the MS-RS-T partition functions are given in Tables 3.7 and 3.8. It is found that the deviations of the MS-RS-T partition functions from for 1-pentyl radical from the MS-AS-T ones are 6 % at 200 K, increasing to 25 % at 400−600 K, then decreasing to 9 % at 2400 K. For the 2-pentyl radical, the deviations are smaller at 200−1000 K; but they increase to 15 % by 2400 K. However, the MS-RS-T method needs much less structural information than the MS-AS-T method, and it saves considerable time in the calculations.

3.2. Transmission coefficient

Figure 3.3 displays the V_{MEP} and V_a^G curves. Both the V_{MEP} and V_a^G curve are well converged with only six nonstationary Shepard points, which is consistent with earlier work.[56] The transmission coefficient calculated using the SCT approximation is also well converged. Therefore, only nine high-level electronic structure theory Hessians along the reaction path were needed to interpolate the potential curves used for the following rate constant calculations.

Because the MCSI method uses just a few Hessian calculations, it saves considerable computation time relative to straight direct dynamics calculations. Also, as compared with theIVTST-M algorithm,[192] the MCSI method provides a more accurate interpolation of the V_{MEP} and V_a^G curves, IVTST-M needs relatively large number of Hessians for a converged result, and those Hessians are located only close to the saddle point, but the Hessians in the MCSI calculations are widely spaced along the reaction path; this makes the interpolation more reliable and robust.

Figure 3.4 shows an Arrhenius plot of the SCT transmission coefficient. This shows that the reaction has a very large tunneling contribution at temperatures below 500 K. In particular, quantum effects on reaction coordinate motion increase the rate constant by factors of 7.6, 29, 821, and 2.6×10^4 at 500, 400, 300,and 250 K, respectively. However, above 1000 K, quantum effects on the reaction coordinate motion increase the rate by less than 60 %.

3.3. SS-VTST rate constant calculations

The forward and reverse single-structural rate constants $k^{\text{SS-CVT/SCT}}$ are calculated using both the SS-HO and the SS-T approximations, and they are labeled as $k_{\text{SS-HO}}^{\text{CVT/SCT}}$ and $k_{\text{SS–T}}^{\text{CVT/SCT}}$, respectively. The results are given in the first and second rate constant columns of Tables 3.10 and 3.11. The SS results of Tables 3.10 and 3.11 replace the older single-structure results of Ref. 138. The calculated rate constant in Ref. 138 agreed well with experiment, but that resulted from a cancellation of three errors: (1) the reactant structure used was not the lowest-energy structure; (2) the V_{a}^{G} curve was poorly interpolated duo to a poor choice of interpolation variable causing the transmission coefficient to be underestimated; and (3) multi-structural and torsional anharmonicity were neglected.

3.4. Multi-structural anharmonicity torsional factors

As mentioned in section 1 of Results and Discussion, for the transition state MS-RS is the same as MS-AS in the present work. Thus here we denote both $F_{\text{MS-X-T}}^{\ddagger}$ as $F_{\text{MS-AS-T}}^{\ddagger}$. Table 3.12 gives the $F_{\text{MS-AS-T}}^{\ddagger}$ factors at various temperatures and it is found that the $F_{\text{MS-AS-T}}^{\ddagger}$ factors range from 3.4 to 4.2. The magnitude can be qualitatively rationalized by the existence of four conformers for the transition state and the similar energies and frequencies of these conformers. $F_{\text{MS-X-T}}^{\text{R}}$ and $F_{\text{MS-X-T}}^{\text{P}}$ (X = RS or T) are also given in Table 3.12. The table shows that the deviations between

$F^{R}_{MS\text{-}AS\text{-}T}$ and $F^{R}_{MS\text{-}RS\text{-}T}$ are larger than those between $F^{P}_{MS\text{-}AS\text{-}T}$ and $F^{P}_{MS\text{-}RS\text{-}T}$. This observation is consistent with the deviations of the conformational-rotational-vibrational partition functions calculated using the two methods mentioned in section 1 of Results and Discussion. In addition, it shows that the reactant and product wells have larger multi-structural anharmonicity factors than the transition state over the whole temperature range. This result is consistent with their larger number of conformers. However, there is no simple relationship between the multi-structural anharmonicity factor and the number of conformers. For instance, the 1-pentyl radical has 15 conformers, but its $F^{R}_{MS\text{-}AS\text{-}T}$ and $F^{R}_{MS\text{-}RS\text{-}T}$ factors are 7.4−9.6 and 6.4−7.6 instead of 15 at 200−300 K.

In the $k^{CVT/SCT}_{MS\text{-}AS\text{-}T}$ calculation, $F^{‡}_{MS\text{-}AS\text{-}T}/F^{R}_{MS\text{-}AS\text{-}T}$ varies from 0.49 at 200 K to 0.31 at 1000 K, then back up to 0.44 at 2400 K. A corresponding analysis for the reverse reaction yields $F^{‡}_{MS\text{-}AS\text{-}T}/F^{P}_{MS\text{-}AS\text{-}T}$ equals to 0.27, 0.26, and 0.46 at these three temperatures.

All the multi-structural torsional anharmonicity factors $F^{‡}_{MS\text{-}AS\text{-}T}$, $F^{R}_{MS\text{-}AS\text{-}T}$, and $F^{P}_{MS\text{-}AS\text{-}T}$ depend on the frequencies used for partition function calculations by the MSTor program.[69] As mentioned in section 3 of Calculation Methods, , the frequencies used in the present work are the ones obtained from the M06-2X/MG3S density functional calculations multiplied by the scale factor 0.970.[46] This scale factor is designed to yield an accurate zero- point energy, and thus applying it makes the V_a^G curve more reliable for the transmission coefficient calculations. However, when

calculating conformational-rotational-vibrational partition functions using the MSTor method, the contributions from the low-frequency modes dominate, and the current scaling factor need not improve the results for those low frequencies. Therefore, we tested the effect of calculating the multi-structural torsional anharmonicity factors without using the scale factor. The ratio of the multi-structural torsional anharmonicity factors calculated with the scaling factors over that without the scaling factors, that is $(F^{X}_{\text{MS-AS-T}})_{\text{scale}} / (F^{X}_{\text{MS-AS-T}})_{\text{noscale}}$ (where X = ‡, R, or P), are listed in Electronic Supplementary Information. One finds that the effect is 6 % or less for 1-pentyl; 2 % or less for the transition state; 7 % or less for 2-pentyl. Thus both the forward and reverse rate constant is not sensitive to the frequencies of the low frequency modes.

3.5. Final thermal rate constants

We employ $k^{\text{CVT/SCT}}_{\text{SS-HO}}$ and $\kappa^{\text{SCT}}(T)$ results discussed in sections 2, 3, and 4 of Results and Discussion to calculate the final thermal rate constant using eq 27. The results are given in the final four columns of Tables 3.10 and 3.11, and Figure 3.5 shows how the final forward and reverse thermal rate constants vary with the temperature. The final rate constants are the canonical thermal rate constants, which are calculated at high-pressure limit. We compare the corresponding experimental data for the forward reaction, also at high-pressure limit in Refs 135 and 136; and Figure 3.5(a) demonstrates that the calculated forward rate constants are in excellent agreement with the experimental results of Yamauchi and Miyoshi et al.[135,136] over their whole temperature range of 300−1300 K.

The next issue to consider is the comparison of MS-CVT/SCT rate constants calculated with the less expensive MS-RS-T approximation to those calculated with the full MS-AS-T approximation. Table 3.10 shows deviations of only 16 % at 200 K, increasing to 33 % at 400−600 K, then decreasing again to 11 % at 2400 K. The performance is even better for the reverse reaction where Table 3.11 shows errors of 8 % or less at 200−600 K, increasing to 13 % at 1500−2400 K. However, one's sense of encouragement in the accuracy of the less expensive reference structure method must be tempered by realization that it results in part from a cancellations of errors. Further testing is warranted.

3.6. Arrhenius activation energy

Based on the calculated thermal rate constant, we calculate the Arrhenius activation energies and fit the rate constant to obtain a formula to predict the rate at any temperature at high-pressure limit. The Arrhenius activation energies is calculated using

$$E_{\mathrm{a}} = -R\frac{d\ln k}{d(1/T)} \tag{28}$$

and the results are listed in Table 3.13. Table 3.13 shows that E_{a} increases with temperature but much more slowly than linear in T, whereas linear behavior is predicted by the very popular fitting expression

$$k = A(\frac{T}{300})^{n}\exp(-\frac{B}{T}) \tag{29}$$

Therefore, as recommended previously,[193] we abandon this popular form and instead fit the calculated rate constants to the more physical functional form given by[193]

$$k = A(\frac{T}{300})^n \exp[-\frac{E(T+T_0)}{R(T^2+T_0^2)}] \quad (30)$$

We obtain $A = 1.06\times10^8$ s^{-1}, $n = 3.2897$, $E = 11.436$ kcal/mol, and $T_0 = 185.34$ K for the forward reaction, and we obtain $A = 8.81\times10^6$ s^{-1}, $n = 4.01577$, $E = 13.865$ kcal/mol, and $T_0 = 165.90$

4. Conclusion

We have addressed the challenge of developing an efficient and accurate way to predict the thermal rate constant of a reaction with multiple conformational states, and we illustrate the new method here by calculating the rate constant of the 1,4-hydrogen shift reaction of 1-pentyl radical. The calculation involved several steps. First, we apply the multi-configuration Shepard interpolation (MCSI) method to obtain the potential energy surface of the reaction by using molecular mechanics to interpolate density functional calculations in the reaction valley that passes through the transition state with the lowest zero-point-inclusive energy. Then a single-structural variational transition state calculation is carried out, and the multi-dimensional tunneling contribution is calculated by the SCT approximation. Finally, the multi-structural effect, including torsional anharmonicity, is added based on optimizations and frequency calculations for all structures of the reactants, products, and transition state. These steps together constitute a new formulation of variational transition state theory labeled MS-VTST.

We found that multi-structural anharmonicity in the harmonic approximation lowers the forward-reaction rate by factors of 0.56, 0.32, and 0.23 at 200, 600, 2400 K,

respectively, and torsional anharmonicity lowers it (again with respect to the single-structural harmonic approximation) by factors of 0.49, 0.32, and 0.44 at these three temperatures. A large transmission coefficient is found for this reaction at lower temperatures, in particular 1.2×10^{7} and 3.90 at 200 and 600 K, respectively. The calculated final forward thermal rate constant agrees with experimental data[1-2] over the entire temperature range (from 300 K to 1300 K) very well. The MS-VTST method used here can be applied to calculate thermal rate constants for other complex unimolecular or bimolecular reactions involving molecules with even larger size.

Table 3.1 Calculated forward and reverse zero-point-exclusive barrier heights and energies of reaction for the 1,4-hydrogen shift isomerization of 1-pentyl radical as calculated by various methods (in kcal/mol)

Method	$V_f^{\ddagger}$	$V_r^{\ddagger}$	ΔE
CCSD(T)-F12b/jul-cc-pVTZ //M06-2X/MG3S	24.65	27.32	−2.67
BMC-CCSD//M06-2X/MG3S	24.60	27.11	−2.51
MCG3-TS//M06-2X/MG3S	24.12	26.91	−2.79
M06-2X/6-31+G(d,p)	25.27	28.27	−3.00
M06-2X/MG3S	25.83	28.97	−3.14
M06-2X/aug-cc-pVTZ	25.94	28.99	−3.05
M06-2X/maug-cc-pVTZ	25.93	28.98	−3.05
M06-2X/def2-TZVP	25.83	28.91	−3.08
M08-SO/MG3S	25.99	29.34	−3.35
M08-SO/aug-cc-pVTZ	25.87	29.42	−3.41
M08-SO/maug-cc-pVTZ	25.94	29.30	−3.36
M08-SO/def2-TZVP	26.04	29.45	−3.40
M06/6-31+G(d,p)	24.61	28.42	−3.81
M06/MG3S	25.18	28.73	−3.55

Table 3.2 Labeling of structures[a]

1	1-pentyl radical	
2	2-pentyl radical	
TS	transition state	
	Abbreviation	dihedral angle range (deg)
antiperiplanar	**a**$^{+}$	[140,172]
	a^{-}	[-172, –140]
gauche for 1-pentyl	**g**$^{+}$	[55, 80]
	g^{-}	[–80, –55]
syn for 1-pentyl only	**s**	[80, 112] or [–112, –80]
trans	**t**	[–173, –180] and [180, 173]

[a] The dihedral angles used for torsions are H–$C^{(1)}$–$C^{(2)}$–$C^{(3)}$, $C^{(1)}$–$C^{(2)}$–$C^{(3)}$–$C^{(4)}$ and $C^{(2)}$–$C^{(3)}$–$C^{(4)}$–$C^{(5)}$ for 1-pentyl and $C^{(1)}$–$C^{(2)}$–$C^{(3)}$–$C^{(4)}$ and $C^{(2)}$–$C^{(3)}$–$C^{(4)}$–$C^{(5)}$ for 2-pentyl, respectively.

Table 3.3 The sequence number and energy[a] (kcal/mol) of structures of the reactant, product, and transition state

structures	number	energy	
		V	$V + \varepsilon^{G}$
		1-pentyl radical	
1a^{-}g^{+}t, 1a^{+}g^{-}t	j = 1, 2	0	89.01
1a^{-}g^{+}g^{+}, 1a^{+}g^{-}g^{-}	j = 3, 4	0.08	89.55
1a^{-}g^{+}g^{-}, 1a^{+}g^{-}g^{+}	j = 5, 6	1.00	92.14
1a^{+}tg^{+}, 1a^{-}tg^{-}	j = 7, 8	0.66	91.02
1a^{+}tt, 1a^{-}tt	j = 9, 10	0.21	89.52
1a^{+}tg^{-}, 1a^{-}tg^{+}	j = 11, 12	0.74	91.20
1stg^{+}, 1stg^{-}	j = 13, 14	0.84	91.64
1stt	j = 15	0.36	90.11
		2-pentyl radical	
2g^{-}a^{+}, 2g^{+}a^{-}	l = 1, 2	−3.14	85.96
2g^{-}g^{-}, 2g^{+}g^{+}	l = 3, 4	−3.12	86.04
2tg^{-}, 2tg^{+}	l = 5, 6	−2.85	86.85
2t^{+}a^{-}, 2t^{-}a^{+}	l = 7, 8	−2.98	86.25
2sg^{-}, 2sg^{+}	l = 9, 10	−2.77	86.99
2g^{+}p, 2g^{-}p	l = 11, 12	−0.59	90.93
		Transition sate	
TS-1, **TS-2**	c = 1, 2	25.83	112.69
TS-3, **TS-4**	c = 3, 4	25.83	112.80

[a] V is the M06-2X/MG3S zero-point-exclusive energy of the structures, and $V + \varepsilon^{G}$ is the zero-point-inclusive energy that is calculated by adding the zero-point energy which is calculated using M06-2X frequencies multiplied by a scale factor from Ref. 69.

Table 3.4 Information used for the 1-pentyl radical partition function using the MS-AS-T method[a]

Torsion	$\overline{\omega}$	I	W	M
		Structure 1 and 2 (U = 0)		
C(1)–C(2)	133	1.71	281	2.53
C(2)–C(3)	142	10.91	2047	2.53
C(3)–C(4)	99	15.98	1040	3
C(4)–C(5)	228	2.92	998	3
		Structure 3 and 4 (U = 0.077 kcal/mol)		
C(1)–C(2)	161	1.71	426	2.48
C(2)–C(3)	131	17.09	2819	2.48
C(3)–C(4)	108	18.38	1418	3
C(4)–C(5)	247	3.05	1228	3
		Structure 5 and 6 (U = 1.00 kcal/mol)		
C(1)–C(2)	157	1.71	382	2.56
C(2)–C(3)	132	15.88	2521	2.56
C(3)–C(4)	110	14.79	1188	3
C(4)–C(5)	254	3.06	1297	3
		Structure 7 and 8 (U = 0.66 kcal/mol)		
C(1)–C(2)	126	1.67	81	4.40
C(2)–C(3)	110	14.45	533	4.40
C(3)–C(4)	125	11.48	1177	3
C(4)–C(5)	229	3.04	1049	3

		Structure 9 and 10 (U = 0.21 kcal/mol)		
C(1)–C(2)	118	1.66	76	4.28
C(2)–C(3)	119	11.4	523	4.28
C(3)–C(4)	117	11.91	1079	3
C(4)–C(5)	227	2.87	976	3
		Structure 11 and 12 (U = 0.74 kcal/mol)		
C(1)–C(2)	109	1.67	64	4.30
C(2)–C(3)	107	14.52	536	4.30
C(3)–C(4)	123	11.34	1135	3
C(4)–C(5)	228	3.04	1041	3
		Structure 13 and 14 (U = 0.84 kcal/mol)		
C(1)–C(2)	103	1.67	82	3.57
C(2)–C(3)	109	15.34	845	3.57
C(3)–C(4)	124	11.53	1161	3
C(4)–C(5)	229	3.04	1051	3
		Structure 15 (U = 0.36 kcal/mol)		
C(1)–C(2)	108	1.65	90	3.56
C(2)–C(3)	121	11.88	816	3.56
C(3)–C(4)	116	11.96	1068	3
C(4)–C(5)	232	2.88	1024	3

[a] We used NS : SC = 2 : 2. The units are cm^{-1} for torsional barrier heights W and frequencies $\overline{\omega}$. The unit is amu $Å^2$ for internal moments of inertia, I, and the local periodicity M is unitless. See Ref. 97 for details of the method.

Table 3.5 Information used for the 2-pentyl radical partition function using the MS-AS-T method[a]

Torsion	$\overline{\omega}$	I	W	M
		Structure 1 and 2 (U = 0)		
C(1)–C(2)	216	3.06	943	3
C(2)–C(3)	145	10.93	1160	3.43
C(3)–C(4)	63	13.66	275	3.43
C(4)–C(5)	121	2.94	285	3
		Structure 3 and 4 (U = 0.022 kacl/mol)		
C(1)–C(2)	223	3.06	1001	3
C(2)–C(3)	116	18.82	2157	2.92
C(3)–C(4)	77	15.68	795	2.92
C(4)–C(5)	136	3.04	371	3
		Structure 5 and 6 (U = 0.29 kcal/mol)		
C(1)–C(2)	227	2.91	990	3
C(2)–C(3)	105	16.34	1240	2.94
C(3)–C(4)	72	10.27	362	2.94
C(4)–C(5)	114	3.02	260	3
		Structure 7 and 8 (U = 0.16 kcal/mol)		
C(1)–C(2)	228	2.85	975	3
C(2)–C(3)	117	12.13	551	4.24
C(3)–C(4)	62	10.78	138	4.24
C(4)–C(5)	122	2.82	278	3
		Structure 9 and 10 (U = 0.37 kcal/mol)		
C(1)–C(2)	238	3.07	1147	3
C(2)–C(3)	140	12.86	1484	3.56
C(3)–C(4)	61	15.24	336	3.56
C(4)–C(5)	98	3.03	190	3
		Structure 11 and 12 (U = 0.37 kcal/mol)		
C(1)–C(2)	204	3.05	836	3
C(2)–C(3)	175	18.97	2660	3.59
C(3)–C(4)	135	10.42	879	3.59
C(4)–C(5)	223	3.05	1003	3

[a] We used NS:SC = 2:2. The units are cm^{-1} for torsional barrier heights *W* and frequencies $\overline{\omega}$. The unit is amu $Å^2$ for internal moments of inertia. *I*, and the local periodicity *M* is unitless. See Ref. 97 for details of the method.

Table 3.6 Information used for the transition state partition function using the MS-AS-T method[a]

Torsion	$\overline{\omega}$	I	W	M
		Structure 1 and 2 (U = 0)		
C(4)–C(5)	191	2.980	718	3
		Structure 3 and 4 (U = −0.0028 kacl/mol)		
C(4)–C(5)	187	3.032	700	3

[a] We used NS : SC = 1 : 0. The units are cm^{-1} for torsional barrier heights W and frequencies $\overline{\omega}$. The unit is amu $Å^2$ for internal moments of inertia. I, and the local periodicity M is unitless. See Ref. 97 for details of the method.

Table 3.7 Calculated conformational-vibrational-rotational partition function of 1-pentyl radical using single-structural and multi-structural methods[a]

T (K)	SS-HO[b]	SS-T[c]	MS-RS-HO	MS-RS-T	MS-AS-HO	MS-AS-T[d]
200	3.40E−92	4.24E−92	2.09E−91	2.16E−91	2.04E−91	2.50E−91
250	3.06E−72	4.05E−72	2.08E−71	2.14E−71	2.14E−71	2.63E−71
298.15	3.24E−59	4.52E−59	2.37E−58	2.45E−58	2.54E−58	3.12E−58
300	8.52E−59	1.19E−58	6.25E−58	6.44E−58	6.69E−58	8.22E−58
400	1.13E−41	1.72E−41	9.26E−41	9.66E−41	1.05E−40	1.28E−40
600	1.01E−23	1.71E−23	9.51E−23	1.01E−22	1.14E−22	1.34E−22
1000	1.65E−07	2.78E−07	1.76E−06	1.78E−06	2.20E−06	2.21E−06
1500	1.88E+03	2.68E+03	2.14E+04	1.82E+04	2.74E+04	2.13E+04
2000	4.05E+09	4.63E+09	4.79E+10	3.29E+10	6.18E+10	3.71E+10
2400	2.60E+13	2.49E+13	3.13E+14	1.82E+14	4.06E+14	2.01E+14

[a] All partition functions in this table have their zero of energy at the bottom of the potential well for the *j* = 1 structure of 1-pentyl.

[b] The partition function of the structure *j* = 1, **1a**$^{+}$**g**$^{-}$**t** calculated using SS-HO approximation.

[c] The partition function of the structure *j* = 1, **1a**$^{+}$**g**$^{-}$**t** calculated using SS-T approximation.

[d] MS-AS-T partition function is calculated using the MS-T program with NS:SC = 2:2.

Table 3.8 Calculated conformational-vibrational-rotational partition function of 2-pentyl radical using single-structural and multi-structural methods[a]

T (K)	SS-HO[b]	SS-T[c]	MS-RS-HO	MS-RS-T	MS-AS-HO	MS-AS-T[d]
200	4.30E−92	6.16E−92	4.00E−91	5.63E−91	4.00E−91	5.81E−91
250	4.17E−72	6.25E−72	4.27E−71	6.24E−71	4.22E−71	6.29E−71
298.15	4.27E−59	6.59E−59	4.71E−58	7.00E−58	4.98E−58	7.50E−58
300	1.22E−58	1.88E−58	1.34E−57	2.00E−57	1.31E−57	1.98E−57
400	1.69E−41	2.67E−41	2.08E−40	3.11E−40	2.00E−40	2.99E−40
600	1.57E−23	2.38E−23	2.17E−22	3.09E−22	2.06E−22	2.84E−22
1000	2.56E−07	3.18E−07	3.94E−06	4.53E−06	3.70E−06	4.01E−06
1500	2.88E+03	2.64E+03	4.70E+04	3.94E+04	4.40E+04	3.43E+04
2000	6.18E+09	4.19E+09	1.04E+11	6.39E+10	9.68E+10	5.57E+10
2400	3.95E+13	2.15E+13	6.72E+14	3.31E+14	6.29E+14	2.89E+14

[a] All partition functions in this table have their zero of energy at the bottom of the potential well for the l = 1 structure of 2-pentyl.

[b] The partition function of the structure l = 1, $\mathbf{2g^{-}a^{+}}$ calculated using SS-HO approximation.

[c] The partition function of the structure l = 1, $\mathbf{2g^{-}a^{+}}$ calculated using SS-T approximation.

[d] MS-AS-T partition function is calculated using the MS-T program with NS:SC = 2:2.

Table 3.9 Calculated conformational-vibrational-rotational partition function of the transition state using single-structural and multi-structural methods[a]

T (K)	SS-HO[b]	SS-T[c]	MS-RS-HO	MS-RS-T	MS-AS-HO	MS-AS-T[d]
200	2.39E−90	2.55E-90	8.05E−90	8.60E−90	8.05E−90	8.60E−90
250	5.63E−71	6.13E-71	1.93E−70	2.11E−70	1.93E−70	2.11E−70
298.15	2.40E−58	2.66E-58	8.33E−58	9.26E−58	8.33E−58	9.26E−58
300	6.12E−58	6.80E-58	2.13E−57	2.37E−57	2.13E−57	2.37E−57
400	2.32E−41	2.65E−41	8.17E−41	9.37E−41	8.17E−41	9.37E−41
600	5.37E−24	6.29E−24	1.92E−23	2.25E−23	1.92E−23	2.25E−23
1000	2.64E−08	3.02E−08	9.55E−08	1.09E−07	9.55E−08	1.09E−07
1500	1.53E+02	1.63E+02	5.54E+02	5.89E+02	5.54E+02	5.89E+02
2000	2.22E+08	2.19E+08	8.06E+08	7.95E+08	8.06E+08	7.95E+08
2400	1.14E+12	1.06E+12	4.13E+12	3.85E+12	4.13E+12	3.85E+12

[a] All partition functions in this table have their zero of energy at the bottom of the potential well for the c = 1 structure of the transition state.

[b] The partition function of the **TS-1** calculated using SS-HO approximation.

[c] The partition function of the **TS-1** calculated using SS-T approximation.

[d] MS-AS-T partition function is calculated using the MS-T program with NS : SC = 1 : 0.

Table 3.10 Forward SS-VTST and MS-VTST thermal rate constants (in s^{-1}) for the 1,4-hydrogen shift isomerization reaction of 1-pentyl radical to produce 2-pentyl radical at various temperatures[a]

T (K)	$k_{\text{SS-HO}}^{\text{CVT/SCT}}$	$k_{\text{SS-T}}^{\text{CVT/SCT}}$	$k_{\text{MS-RS-HO}}^{\text{CVT/SCT}}$	$k_{\text{MS-RS-T}}^{\text{CVT/SCT}}$	$k_{\text{MS-AS-HO}}^{\text{CVT/SCT}}$	$k_{\text{MS-AS-T}}^{\text{CVT/SCT}}$
200	5.27E−06	4.51E−06	2.89E−06	2.98E−06	2.96E−06	2.58E−06
250	9.19E−04	7.56E−04	4.63E−04	4.92E−04	4.50E−04	4.01E−04
298.15	4.80E−02	3.81E−02	2.28E−02	2.45E−02	2.13E−02	1.92E−02
300	5.12E−02	4.07E−02	2.43E−02	2.62E−02	2.27E−02	2.06E−02
400	2.11E+01	1.58E+01	9.07E+00	9.97E+00	8.00E+00	7.52E+00
600	3.27E+04	2.26E+04	1.24E+04	1.37E+04	1.04E+04	1.03E+04
1000	2.59E+07	1.76E+07	8.78E+06	9.91E+06	7.03E+06	7.98E+06
1500	9.34E+08	6.98E+08	2.96E+08	3.71E+08	2.32E+08	3.17E+08
2000	6.02E+09	5.19E+09	1.85E+09	2.65E+09	1.43E+09	2.35E+09
2400	1.56E+10	1.51E+10	4.71E+09	7.53E+09	3.62E+09	6.81E+09

[a] Includes variational effects, torsional anharmonicity, and tunneling.

Table 3.11 SS-VTST and MS-VTST thermal rate constants (in s^{-1}) for the 1,4-hydrogen shift isomerization reaction of 2-pentyl radical to produce 1-pentyl radical at various temperatures[a]

T (K)	$k^{\text{CVT/SCT}}_{\text{SS-HO}}$	$k^{\text{CVT/SCT}}_{\text{SS-T}}$	$k^{\text{CVT/SCT}}_{\text{MS-RS-HO}}$	$k^{\text{CVT/SCT}}_{\text{MS-RS-T}}$	$k^{\text{CVT/SCT}}_{\text{MS-AS-HO}}$	$k^{\text{CVT/SCT}}_{\text{MS-AS-T}}$
200	1.94E−10	1.44E−10	7.02E−11	5.33E−11	7.03E−11	5.18E−11
250	2.14E−07	1.56E−07	7.17E−08	5.37E−08	7.26E−08	5.32E−08
298.15	3.45E−05	2.47E−05	1.08E−05	8.11E−06	1.11E−05	8.20E−06
300	4.09E−05	2.95E−05	1.29E−05	9.67E−06	1.32E−05	9.73E−06
400	7.93E−02	5.73E−02	2.27E−02	1.74E−02	2.36E−02	1.81E−02
600	5.87E+02	4.54E+02	1.52E+02	1.25E+02	1.60E+02	1.36E+02
1000	1.67E+06	1.67E+06	3.91E+05	3.89E+05	4.16E+05	4.38E+05
1500	1.15E+08	1.34E+08	2.54E+07	3.23E+07	2.74E+07	3.73E+07
2000	1.03E+09	1.49E+09	2.22E+08	3.55E+08	2.38E+08	4.08E+08
2400	3.12E+09	5.33E+09	6.66E+08	1.26E+09	7.15E+08	1.45E+09

[a] Includes variational effects, torsional anharmonicity, and tunneling. Note that the reaction in this table is the reverse of that in Table 3.10.

Table 3.12 Multi-structure torsional anharmonicity factors with respect to the structures **TS-1** as the transition state, **1a^{+}g^{-}t** as the reactant well, and **2g^{-}a^{+}** as the product well

T (K)	$F^{\ddagger}_{\text{MS-AS-X}}$		$F^{\text{R}}_{\text{MS-RS-X}}$		$F^{\text{R}}_{\text{MS-AS-X}}$		$F^{\text{P}}_{\text{MS-RS-X}}$		$F^{\text{P}}_{\text{MS-AS-X}}$	
	HO	T	HO	T	HO	T	HO	T	HO	T
200	3.37	3.60	6.15	6.36	6.00	7.36	9.30	13.26	9.31	13.50
250	3.43	3.75	6.80	6.98	6.99	8.58	10.25	15.00	10.13	15.10
298.15	3.47	3.86	7.31	7.54	7.84	9.62	11.02	16.27	10.78	16.23
300	3.48	3.87	7.34	7.57	7.85	9.65	11.02	16.32	10.74	16.27
400	3.52	4.04	8.19	8.56	9.29	11.34	12.29	17.93	11.82	17.65
600	3.58	4.19	9.42	9.98	11.29	13.20	13.83	18.69	13.13	18.14
1000	3.62	4.12	10.67	10.71	13.33	13.34	15.40	16.34	14.46	15.67
1500	3.62	3.86	11.38	9.64	14.57	11.29	16.33	12.41	15.25	11.90
2000	3.63	3.59	11.83	8.11	15.26	9.14	16.76	9.36	15.68	9.01
2400	3.62	3.39	12.04	6.97	15.62	7.71	17.01	7.56	15.90	7.31

Table 3.13 Forward and reverse activation energy (in kcal/mol) calculated by MS-VTST for the 1,4-hydrogen shift isomerization reaction of 1-pentyl radical to produce 2-pentyl radical at various temperatures

T (K)	300	400	600	1000	1500	2000
forward (MS-VTST)	12.6	15.6	18.7	21.7	23.4	26.1
reverse (MS-VTST)	16.4	19.0	22.9	25.4	27.9	29.5

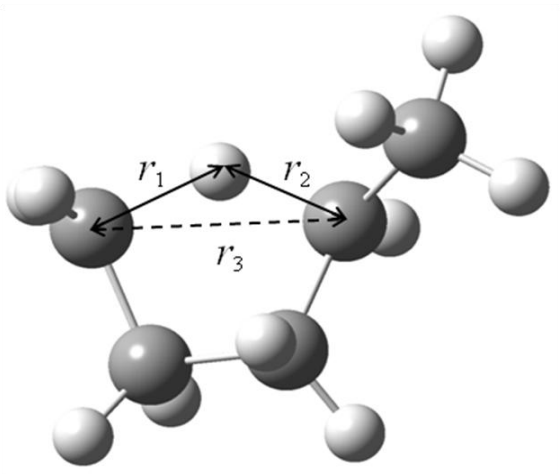

Figure 3.1 Three intra-atomic distances r_1, r_2 and r_3 used to calculate weight function (set s) for Shepard interpolation.

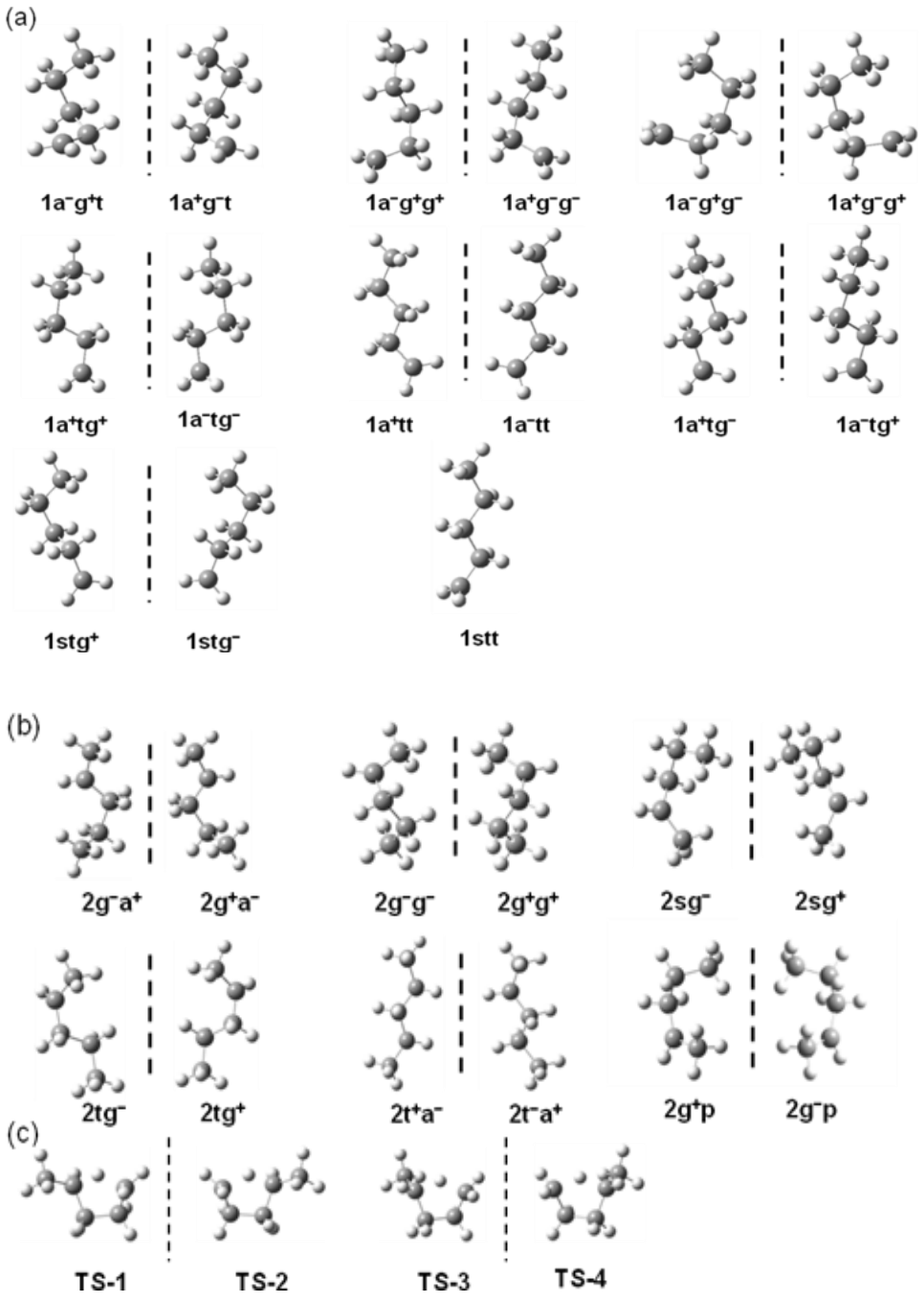

Figure 3.2 Fifteen structures of 1-pentyl radical (a); ten structures of 2-pentyl radical (b); and four structures of the transition state (c). A vertical dashed line is used to separate the mirror image structures.

.

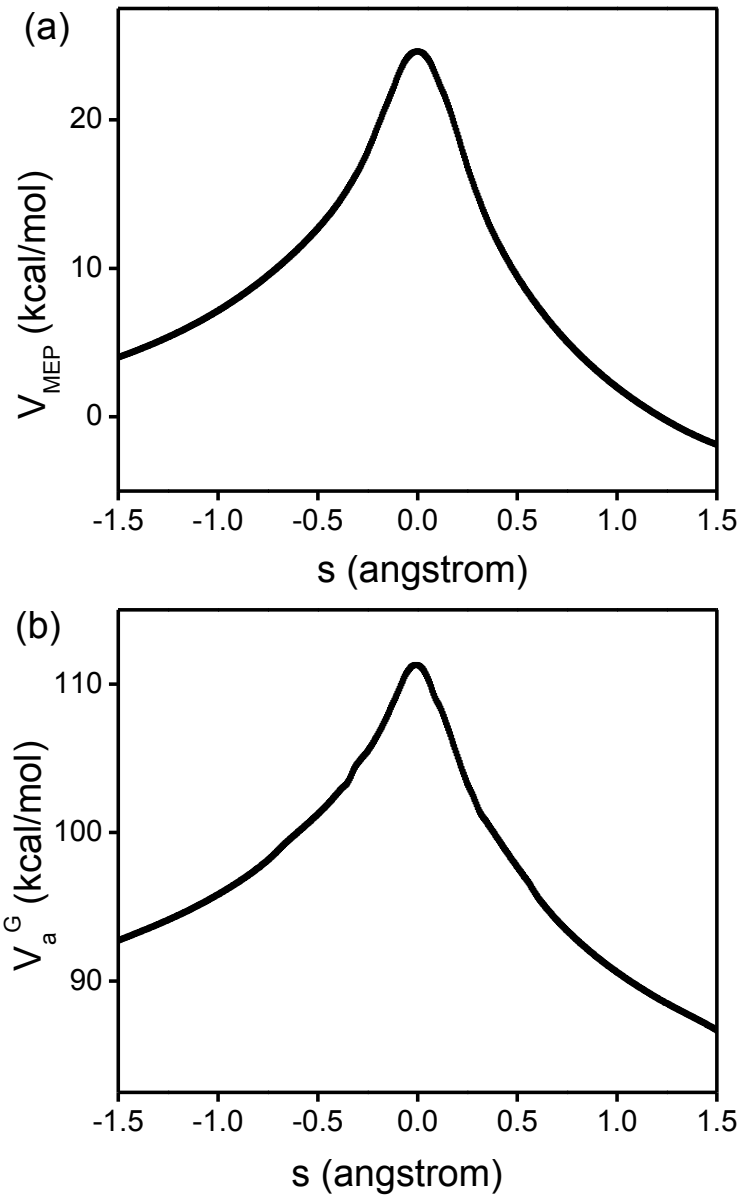

Figure 3.3 Calculated V_{MEP} and ground-state vibrationally adiabatic potential ($V_{\mathrm{a}}^{\mathrm{G}}$) vs the reaction coordinate *s* (scaled to a reduced mass of one amu) for the 1,4-hydrogen shift isomerization reaction of 1-pentyl radical. This figure is based on M06/6-31+G(d,p).

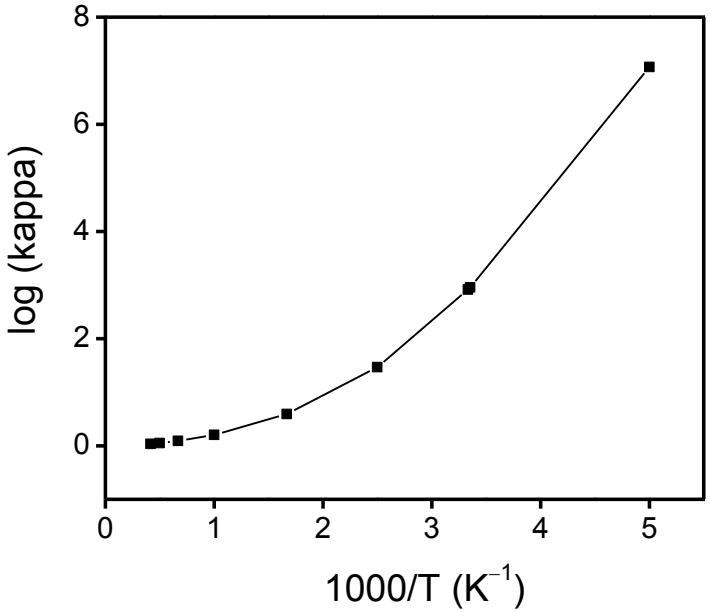

Figure 3.4 Calculated common logarithm of the SCT transmission coefficient κ vs reciprocal temperature (times a thousand).

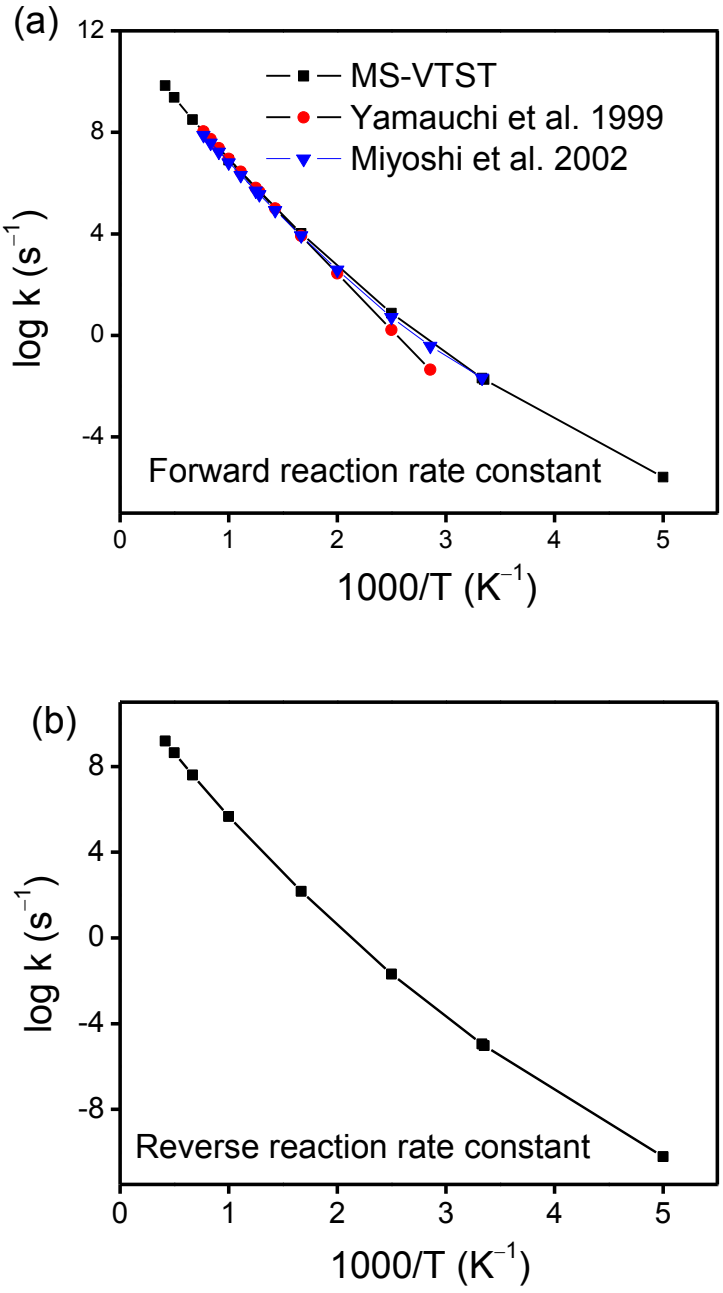

Figure 3.5 Arrhenius plots of calculated (a) forward and (b) reverse rate constant $k_{\text{MS-AS-T}}^{\text{CVT/SCT}}$ calculated by MS-VTST (black curve) and previous experimental data for the 1,4-hydrogen shift isomerization reaction of 1-pentyl radical to produce 2-pentyl radical.

Chapter 4. Multi-Path Variational Transition State Theory. Rate Constant of the 1,4-Hydrogen Shift Isomerization of the 2-Cyclohexylethyl Radical

1. Introduction

The 1,4-hydrogen shift isomerization of an alkyl radical is an important type of reaction in combustion. The 1,4-hydrogen shift isomerizations of 1-pentyl[135−138] and 1-hexyl[3] radicals in the gas phase have been studied by both experimental and computational methods. In the present work, we calculate the thermal rate constant of another 1,4-hydrogen shift isomerization, in particular that of a more complicated molecule, 2-cyclohexylethyl radical. The 2-cyclohexylethyl radical contains a six-membered ring and a side chain that has internal rotations around two carbon−carbon bonds, and these features require including torsional anharmonicity and a large number of diverse structures to model the reaction; this makes accurate calculation of the thermal rate constant challenging. In addition, the large size of the molecule makes minimum-energy-path[139] (MEP) calculations using direct-dynamics[142,143] algorithms very time-consuming.

In the present work, to address these issues and to compute the thermal rate constants for both the forward and reverse reactions efficiently, we propose a new formulation of variational transition state theory (VTST) called multi-path VTST (MP-VTST); this formulation is based on the recent formulation[98] of multi-structural VTST (MS-VTST). In MS-VTST we employ only one reaction path to evaluate the dynamic recrossing and tunneling effects in the reaction. However, MP-VTST can be based on all reaction paths (full multi-path) or a subset of dominating paths to calculate the

quantum mechanical dynamic effects on reaction-coordinate motion. The potential energy surface in the broad vicinity of each reaction path is obtained by multi-configuration Shepard interpolation[144,182] (MCSI) method.

A key component of the free energy of reaction and free energy of activation for complex reactions is the conformational free energy, which is defined as the difference between the conformational−rotational−vibrational free energy calculated including all the conformations (also called structures) and that calculated including just the lowest-energy conformation. The free energy of activation includes the conformational free energy of the transition state minus that of reactants. MP-VTST, like MS-VTST, contains conformational free energy contributions based on the MS-T method[97] for including multiple-structure effect and explicit torsional anharmonicity in the partition functions of the reactant and saddle point configurations; thus it provides more reliable results than those calculated using single-structural variational transition state theory[148,151] (SS-VTST) with the harmonic approximation, especially at high temperature. In the present article we also calculate reverse reaction rates, and therefore we also calculate the conformational free energy and torsional anharmonicity of the product.

The MCSI method avoids the very expensive straight direct-dynamics method to obtain the MEP and ground-state vibrationally adiabatic potential curve V_a^G, and in particular it efficiently generates a semiglobal potential energy surface based on a small number of high-level electronic structure calculations. In this article, the M06 density functional[64,146] is used to compute the energies, gradients, and Hessians of stationary Shepard points (reactant well, product well, and saddle point) and non-stationary

Shepard points along each reaction path. The Shepard-interpolated potential energy surface is used to compute the transmission coefficient for each reaction path by utilizing the multidimensional small-curvature tunneling (SCT) approximation.[147,148]

In order to obtain the MP-VTST rate constant, the multi-structural anharmonicity factors are calculated by using the multi-structural (MS) anharmonicity method[97,116] for the conformational−rotational−vibrational partition functions of the reactant, product, and transition state. For this purpose, we include all structures of the reactant, product, and saddle point, and we employ the M06-2X density functional[64,146] to obtain the structures of the reactant, product, and transition state, which are generated either by internal rotations around the carbon−carbon bond or by pseudorotation of the six-membered ring structure.

The theory presented here assumes that the internal states of the reactant, product, and transition state are described by a canonical ensemble. For a unimolecular reaction, this is called the high-pressure limit. For a bimolecular reaction, the theory assumes that the reaction is slow enough that energy transfer collisions maintain the reactant in a Boltzmann distribution.

2. Calculation Methods

2.1. Electronic Structure Calculations

The M06-2X density functional with the 6-311+G(2df,2p) basis set[66,67,108] was applied to optimize the geometries and obtain the frequencies for all the conformers of the reactant 2-cyclohexylethyl radical, the product *R*-2-ethylcyclohexan-1-yl radical,

and the transition state. The 6-311+G(2df,2p) basis set for H and C is also called MG3S,[109] and we will use the short name for brevity.

For the global minimum-energy conformers of the reactant 2-cyclohexylethyl radical, the product *R*-2-ethylcyclohexan-1-yl radical, and the transition state, we employed the M06, M06-2X, and M08-SO[172] density functionals to optimize the geometries and calculate the energetics, in particular the reaction energies and barrier heights. In addition, two multilevel methods, BMC-CCSD[110] and MCG3-TS,[173] and the ab initio CCSD(T)-F12a[111,112] method were used to calculate single-point energies at the M06-2X optimized geometries.

Other basis sets were also used for electronic structure calculations, including 6-31+G(d,p),[67] maug-cc-pVTZ,[174] aug-cc-pVTZ,[175] may-cc-pVTZ[113] and def2-TZVP.[176] The M06 and M06-2X density functional calculations were performed by using the *Gaussian 09* program,[69] the M08-SO density functional calculations were carried out via MN-GFM-4.1,[177] which is a locally modified version of *Gaussian* 03; CCSD(T)-F12a calculations were performed using *Molpro*;[115] and the BMC-CCSD and MCG3-TS calculations were carried out using MLGAUSS2.0.[114] The integration grid employed for density functional calculations of frequencies had 99 radial shells and 974 angular points per shell. The frequencies used for the partition function and multi-structural torsional anharmonicity factor calculations in section 2.2 are obtained by using M06-2X/MG3S density functional calculations and multiplying the directly calculated values by an empirical frequency scaling factor[69] of 0.970.

2.2. Conformational−vibrational−rotational partition functions and multi-structural torsional anharmonicity calculations

The complete conformational−rotational−vibrational partition functions of the reactant (R), product, (P) and transition state (TS or ‡) were calculated by the MS method[15] mentioned above by using the *MSTor* program.[116] Including multiple structures and making the harmonic approximation in the vicinity of each local minimum of the potential energy surface is called the local harmonic (LH) approximation, and calculations including torsional anharmonicity have a suffix -T. If one uses all structures (AS), one may call the resulting multi-structural methods MS-AS-LH and MS-AS-T. However, in the rest of this paper (and in future work, except when we need to emphasize that all structures are included), we will shorten MS-AS-LH and MS-AS-T to MS-LH and MS-T, respectively; this will not cause confusion in the present paper because we always employ all structures in the present article. (MS-AS-T and MS-AS-LH were called MS-AS and MS-HO, respectively, in the original[11] reference, but we have abandoned that notation as being too easily misunderstood.)

In the MS-LH and MS-T versions of the MS method we respectively have

$$Q_{\text{con-rovib}}^{\text{MS-LH,X}} = \sum_{j=1}^{J} Q_{\text{rot},j} \exp\left(-\beta U_j\right) Q_j^{\text{HO}} \tag{1}$$

and

$$Q_{\text{con-rovib}}^{\text{MS-T,X}} = \sum_{j=1}^{J} Q_{\text{rot},j} \exp\left(-\beta U_j\right) Q_j^{\text{HO}} Z_j \prod_{\text{t}=1}^{t} f_{j,\text{t}} \tag{2}$$

where "con" denotes conformational, "rovib" denotes rotational−vibrational, and X can be R, P, or ‡, representing the reactant, product, and transition state; $Q_{\mathrm{rot},j}$ is the classical rotational partition function of structure *j*, Q_j^{HO} is the normal-mode harmonic-oscillator vibrational partition function calculated at structure *j*, Z_j is a factor designed to ensure that the MS-T scheme reaches the correct high-*T* limit (within the parameters of the model), and $f_{j,\tau}$ is an internal-coordinate torsional anharmonicity function that, in conjunction with Z_j, adjusts the harmonic partition function of structure *j* for the presence of the torsional motion τ. As mentioned in section 2.1, frequencies used for the Q_j^{HO}, Z_j, and $f_{j,\tau}$ calculations were scaled by an empirical frequency scaling factor.[33] We use the label MS-LH to denote the partition function calculated without Z_j and $f_{j,\tau}$, that is, with all Z_j and all $f_{j,\tau}$ equal to unity.

When using either the MS-LH or the MS-T version of the MS method, it is not necessary to assign each torsional motion to a specific normal mode. The MS-T approximation reduces to the MS-LH approximation in the low-temperature limit, and it approaches the free-rotor result in the high-temperature limit. The Z_j and $f_{j,\tau}$ factors are designed to interpolate the partition functions between these limits in the intermediate temperature range. In principle, more accurate interpolations could be carried out if one calculated the barrier heights for torsional motions that interconvert the reactant structures with one another and the transition state structures with one another, but an advantage of the method employed here is that it does not require this expensive step.

We define a single-structure (SS) rotational-vibrational partition function for structure *j* using the harmonic-oscillator approximation and including torsional anharmonicity, respectively

$$Q_{\text{rovib},j}^{\text{SS-HO}} = Q_{\text{rot},j} \exp(-U_j/\beta) Q_{\text{vib},j}^{\text{HO}} \tag{3}$$

and

$$Q_{\text{rovib},j}^{\text{SS-T}} = Q_{\text{rot},j} \exp(-U_j/\beta) Q_{\text{vib},j}^{\text{HO}} Z_j \sum_{t=1}^{t} f_{j,t} \tag{4}$$

Equation 3 is used to calculate the SS-HO partition functions for the single-structural variational theory (SS-VTST) calculations discussed in section 2.3. In the calculations of the present article, the structure retained is the one with the lowest energy, i.e., $j = 1$.

We define $F_{\text{MS-X}}^{\text{Y}}$ as the ratio of the partition function calculated by the MS-T method to that calculated by SS-HO,

$$F_{\text{MS-X}}^{\text{Y}} = Q_{\text{con- rovib}}^{\text{MS- X,Y}} / Q_{\text{rovib, 1}}^{\text{SS-HO,Y}} \tag{5}$$

where X = LH or T; Y = R, P, or ‡ (we use TS and ‡ interchangeably to denote the transition state). We call $F_{\text{MS-T}}^{\text{Y}}$ the multi-structural torsional anharmonicity factor, whereas $F_{\text{MS-LH}}^{\text{Y}}$ is an intermediate result that includes all the structures, but not torsional anharmonicity. For brevity, $F_{\text{MS-LH}}^{\text{Y}}$ will be called the multiple-structure factor. Both $F_{\text{MS-T}}^{\text{Y}}$ and $F_{\text{MS-LH}}^{\text{Y}}$ are used in this paper for MP-VTST thermal rate constant calculations, with $F_{\text{MS-T}}^{\text{Y}}$ leading to our most reliable results and $F_{\text{MS-LH}}^{\text{Y}}$ being used to illustrate what would be predicted an intermediate level of statistical mechanical theory. Further details are discussed in section 2.4.

2.3 Multi-path variational transition state theory (MP-VTST) rate constants

For a unimolecular reaction, multi-path variational transition state theory (MP-VTST) rate constants are calculated by

$$k^{\mathrm{MP-VTST}} = \langle \gamma \rangle_p^{\mathrm{MP}} \frac{1}{\beta h} \frac{Q_{\mathrm{el}}^{\ddagger} Q_{\mathrm{con-rovib}}^{\mathrm{MS-T},\ddagger}}{Q_{\mathrm{el}}^{\mathrm{R}} Q_{\mathrm{con-rovib}}^{\mathrm{MS-T,R}}} \exp(-\beta V^{\ddagger}) \qquad (6)$$

where $\langle g \rangle_P^{\mathrm{MP}}$ is a path-averaged generalized transmission coefficient, P is the number of paths considered, β is $(k_{\mathrm{B}}T)^{-1}$, k_{B} is Boltzmann's constant, h is Planck's constant, $Q_{\mathrm{el}}^{\mathrm{X}}$ is electronic partition function for species X (X = R or TS), $V^{\ddagger}$ is a zero-point-exclusive barrier height (sometimes also called classical barrier height) which is the energy difference between the lowest-energy reactant structure and the lowest-energy saddle point. The energy of the lowest-energy reactant structure is set as the zero of energy in eq 6, and the zero of energy for the transition state partition function is the lowest-energy saddle point. The path-averaged generalized transmission coefficient $\langle g \rangle_P^{\mathrm{MP}}$ is discussed in section 2.4. In order to make the calculations more practical and the physical meaning of the formulism more clear as compared with the well established variational transition state theory that uses only a single structure of the reactant and the saddle point, we rearrange eq 6 as

$$k^{\mathrm{MP\text{-}VTST}} = \langle \gamma \rangle_p^{\mathrm{MP}} F^{\mathrm{MS\text{-}X}}(T) \frac{1}{\beta h} \frac{Q_{\mathrm{el}}^{\ddagger}(T) Q_{\mathrm{rovib},k^*}^{\mathrm{SS\text{-}HO},\ddagger}(T)}{Q_{\mathrm{el}}^{\mathrm{R}}(T) Q_{\mathrm{rovib},1}^{\mathrm{SS\text{-}HO}}(T)} \exp(-\beta V_{k^*}^{\ddagger}) \qquad (7)$$

where k^* is a selected transition-state structure that can be any of the K saddle points; $V_{k^*}^{\ddagger}$ is the energy of structure k^* relative to the global minimum reactant structure; we

use the global minimum of the reactant (j = 1 structure) for $Q_{\text{rovib},1}^{\text{SS-HO}}(T)$, and $F^{\text{MS-X}}(T)$ is defined by

$$F^{\text{MS-X}} = \frac{F_{\text{MS-X}}^{\ddagger}(T)}{F_{\text{MS-X}}^{\text{R}}(T)} \tag{8}$$

where X = LH or T, and the quantities on the right side of eq 8 were defined in eq 5. In greater detail, we have

$$F_{\text{MS-X}}^{\ddagger} = \frac{Q_{\text{con-rovib}}^{\text{MS- X},\ddagger}(T)}{Q_{\text{rovib},\,k^*}^{\text{SS-HO},\,\ddagger}(T)} \tag{9}$$

$$F_{\text{MS-X}}^{\text{R}} = \frac{Q_{\text{con-rovib}}^{\text{MS-X,R}}(T)}{Q_{\text{rovib},1}^{\text{SS-HO, R}}(T)} \tag{10}$$

where $Q_{\text{con-rovib}}^{\text{MS–X},\ddagger}(T)$ is the conformational−rotational−vibrational partition functions calculated using eqs 1 and 2.

If we set the generalized transmission coefficient $\langle \gamma \rangle_P^{\text{MP}}$ to unity, eq 7 reduces to the multi-structural conventional transition state theory (MS-TST) rate

$$k^{\text{MS-TST}} = F^{\text{MS-X}}(T)\frac{1}{\beta h}\frac{Q_{\text{el}}^{\ddagger}(T)Q_{\text{rovib},k^*}^{\text{SS-HO},\,\ddagger}(T)}{Q_{\text{el}}^{\text{R}}(T)Q_{\text{rovib},1}^{\text{SS-HO}}(T)}\exp(-\beta V_{k^*}^{\ddagger}) \tag{11}$$

For the two versions of the MS method (X = LH or T), the corresponding rate constants are labeled $k_{\text{MS-LH}}^{\text{MS-TST}}$ and $k_{\text{MS-T}}^{\text{MS-TST}}$ where the latter one includes not only multiple-structure anharmonicity but also the torsional anharmonicity effect; thus it is used in the final calculation of the MP-VTST rate constant.

If the multi-structural anharmonicity factor $F^{\text{MS-X}}$ is set to unity, eq 10 is further reduced to the single-structure conventional transition state theory rate constant using harmonic-oscillator approximation

$$k^{\text{TST}}_{\text{SS-HO},k*}(T) = \frac{1}{\beta h}\frac{Q^{\ddagger}_{\text{el}}(T)Q^{\text{SS-HO},\ddagger}_{\text{rovib},k*}(T)}{Q^{\text{R}}_{\text{el}}(T)Q^{\text{SS-HO}}_{\text{rovib},1}(T)}\exp(-\beta V^{\ddagger}_{k*}) \qquad (12)$$

2.4. Path-averaged generalized transmission coefficients

In multi-path variational transition state theory, the reactant, product, and transition state all have a multi-structural anharmonicity with usually a different number of structures; but the number of reaction paths is equal to the number of transition state structures, and we denote this number as K as stated before. We label the structures of the transition state, as k ($k = 1, 2, \ldots, K$), those of reactant as j ($j = 1, 2, 3, \ldots, J$), and those of product as l ($l = 1, 2, 3, \ldots, L$). The potential energy along each path, relative to the overall zero of energy, which is the potential energy of the lowest energy equilibrium structure of the reactants, is denoted as V_{MEP}. Each k labels a path; and the structures j and l that are connected with it by an MEP were used for MCSI calculations.

In practice, although the number of reaction paths is K, one can base the calcuations on a smaller number P, where $2 \le P \le K$. (When $P = 1$, the theory reduces to MS-VTST.) The calculated dynamic recrossing coefficient and transmission coefficient for path k are labeled as $\Gamma_k(T)$ and $\kappa_k(T)$. The path-averaged transmission coefficients and dynamic recrossing coefficients can be calculated using[194]

$$\langle \gamma \rangle_P^{\mathrm{MP}} = \langle \Gamma(T)\kappa(T)g(T) \rangle_P = \frac{\sum_{k=1}^{P} \Gamma_k(T)\kappa_k(T)g_k(T)Q_{\mathrm{rovib},k}^{\mathrm{SS\text{-}HO},\ddagger}}{\sum_{k=1}^{P} Q_{\mathrm{rovib},k}^{\mathrm{SS\text{-}HO},\ddagger}} \qquad (13)$$

where P is the number of paths considered, $\Gamma_k(T)$, $\kappa_k(T)$, and $g_k(T)$ are respectively the dynamic recrossing coefficient, transmission coefficient, and non-equilibrium coefficient of path k. We assume that $g_k(T)$ is equal to unity in the present work.

In a full treatment, eq 13 should include all the reaction paths, i.e., P should be K. However some paths have very large barrier heights, and their contribution to the path-averaged generalized transmission coefficient may be negligible at some temperatures in general because the weighting factor $Q_{\mathrm{rovib},k}^{\mathrm{SS\text{-}HO},\ddagger}$ is small due to high energy. Therefore, only those paths with the lowest barrier heights (more rigorously, with the largest $Q_{\mathrm{rovib},k}^{\mathrm{SS\text{-}HO},\ddagger}$) need to be considered in the calculation. Furthermore, it may not be necessary to include all paths that have a significant weight because we expect many low-energy paths have similar $\Gamma_k(T)$ and $\kappa_k(T)$. For example, if $\Gamma_k(T)\kappa_k(T)$ were the same for all paths, then $\langle \gamma \rangle_P^{\mathrm{MP}}$ would already reach its limiting value with P = 1, which was used previously.[98] In the present work, we choose to average over two reaction paths corresponding to TS structures k =1 and k = 2, i. e., P = 2.

For each reaction path, corresponding to a particular transition-state conformer (k), the MCSI method was utilized to obtain the MEP and ground-state vibrationally adiabatic potential curve ($V_{\mathrm{a}}^{\mathrm{G}}$), which were used to calculate the dynamic recrossing

coefficients $\Gamma_k(T)$ and the transmission coefficient $\kappa_k(T)$ that incorporates the tunneling contributions using the small-curvature tunneling approximation[147,148] (SCT). The effective potential for tunneling is given by

$$V_a^G = V_{MEP}(s) + \varepsilon^G(s) \quad (14)$$

where *s* is the signed arc length along the MEP, $V_{MEP}(s)$ is the potential energy along the MEP, and $\varepsilon^G(s)$ is the local zero point energy (summed over all bound local vibrational modes). Note that the quantities in eq 14 should all have a label *k*, but we suppress the *k* dependence to keep the notation simpler. The *MCSI*[183] and *MC-TINKERATE*[184] programs were employed to carry out these calculations.

2.5. MCSI algorithm for potential energy surfaces

In the MCSI calculation for each path, the zero of energy for the potential energy surface is defined at the global minima of the reactant, and we call that structure $j = 1$, and its potential energy is $U_1 = 0$ by definition. For each path, nine electronic-structure Shepard points (three stationary and six nonstationary) were used to build the potential energy surface by the MCSI method. All the information needed at Shepard points, namely energies, gradients, and Hessians, was obtained by M06/6-31+G(d,p) calculations. The three stationary Shepard points were placed at the saddle point, reactant well, and product well for that path. The other six Shepard points are non-stationary points and were placed close to the minimum energy reaction path (MEP) using the strategy to that developed previously.[178]

The MCSI method involves interpolating the off-diagonal element of a diabatic potential matrix[145,180,181] where the diagonal elements are given by molecular mechanics. We use the MM3 method[186–188] for the molecular mechanics. It was found that using a Morse potential for the C−H bond in the MM3 force field for the Shepard interpolation provided smoother V_a^G curves than using quadratic stretch potentials, and so we used Morse stretches for C−H bonds in all MM3 calculations. The Morse parameters are: bond energy: 98 kcal/mol;[189] bond length: 1.12 angstrom;[180,181,186] and force constant: 4.74 N/cm.[180,186–188]

As discussed in previous work,[182] we used three different internal coordinate sets for MCSI calculations: set q for molecular mechanics calculations, set r for Shepard interpolation, and set s to calculate the Shepard weighting function. In the present work, the set q is the standard set of MM3 internal coordinates, the set r consists of 63 nonredundant internal coordinates (23 bond distances, 38 bond angles, and 2 dihedral angles), and the set s consists of the three intra-atomic distances involving the atoms of the breaking and forming bonds.

Note that in principle the MCSI method provides the PES in a broad swath around a reaction path; where a region broad enough to calculate even the large-curvature tunneling effect, including multi-dimensional corning-cutting tunneling, is called a reaction swath.[195,196]

2.6. Arrhenius activation energies and fitting of the calculated rate constants

We calculate Arrhenius activation energies as

$$E_{\mathrm{a}} = -R\frac{d\ln k}{d(1/T)} \tag{15}$$

for both the forward and reverse reactions, where R is the gas constant. We fit the calculated rate constants to the recently proposed[193] form given by

$$k = A(\frac{T}{300})^n \exp[-\frac{E(T+T_0)}{R(T^2+T_0^2)}] \tag{16}$$

which contains four parameters, A, n, T_0, and E. Based on eq 16, the Arrhenius activation energy E_{a} can be obtained by

$$E_{\mathrm{a}} = E\frac{T^4+2T_0T^3-T_0^2T^2}{(T^2+T_0^2)^2} + n\mathrm{R}T \tag{17}$$

3. Results and Discussion

3.1. Structures, energetics, and conformational−vibrational−rotational partition functions of reactant, product, and saddle point

Table 4.1 gives the zero-point-exclusive barrier heights and energies of reaction for the 1,4-hydrogen shift isomerization reaction of 2-cyclohexylethyl radical calculated by various theoretical methods. The CCSD(T)-F12a/may-cc-pVTZ//M calculation (where we use //M as shorthand for //M06-2X/MG3S) provides our best estimate. Barriers calculated by the BMC-CCSD//M and MCG3-TS//M multi-coefficient methods

agree extremely well with each other (especially when one consider that these methods have quite different components) and with the best estimate. However, the M06-2X and M08-SO density functionals with the 6-31+G(d,p), MG3S, maug-cc-pVTZ, aug-cc-pVTZ, and def2-TZVP basis sets predict larger barrier heights. It is found that the M06 functional with the 6-31+G(d,p) basis gives results reasonably close to the CCSD(T)-F12a/may-cc-pVTZ//M calculation. Therefore, we chose M06/6-31+G(d,p) for the single-structural components of the kinetics calculation, that is, to calculate $k_{\mathrm{SS-HO}}^{\mathrm{CVT}}$ and κ^{SCT}. However we expect M06-2X/MG3S to be more accurate for conformational energy differences, so we calculated $F^{\mathrm{MS\text{-}X}}$ based on M06-2X/MG3S results.

The M06-2X/MG3S calculations show that 2-cyclohexylethyl radical, which contains two torsions and a six-membered ring, has 22 distinguishable structures (Figure 4.1). We label the molecule as shown in Figure 4.2. The combination of the $C^{(1)}$–$C^{(2)}$ torsion and the $C^{(2)}$– $C^{(3)}$ torsion with the pseudo-rotation of the six-membered ring can produce many different conformers. The internal rotations around the $C^{(1)}$–$C^{(2)}$ and $C^{(2)}$–$C^{(3)}$ bonds generate torsional conformers, and the pseudo-rotation of the six-membered ring produces ring conformers, in particular, the chair equatorial (**C-e**), chair axial (**C-a**), twisted-boat equatorial (**B-e**), and twisted-boat axial (**B-a**) conformers. Table 4.2 and Figure 4.1 show the naming convention that is used for labeling of the structures. For example, **C-e-g$^-$g$^+$** means that the conformer of 2-cyclohexylethyl radical has a chair-equatorial ring structure and that the first and second exocyclic dihedral angles are in the ranges of −80 to −40 and 40 to 80 degrees, respectively. The numbering of the structures is specified in Table 4.3. It is found that

structures 5 and 6 have a plane of symmetry, but the others do not, and they occur in mirror image pairs. The global minimum conformer is the mirror image pair **C-e-g$^-$g$^+$** and **C-e-g$^+$g$^-$**, and those structures with twisted-boat ring structure have an energy 6−7 kcal/mol higher than the global minimum.

The product, *R*-2-ethylcyclohexan-1-yl radical is labeled as Figure 4.2.The internal rotation around $C^{(1)}$–$C^{(2)}$ does not generate any distinguishable conformers. Therefore, only the torsion around $C^{(2)}$– $C^{(3)}$ bond and the pseudo-rotation of the ring produce conformers, and the resulting nine structures are displayed in Figure 4.3. None of these nine conformers forms a mirror image pair with any other.

Based on M06-2X calculations, the transition state between 2-cyclohexylethyl and *R*-2-ethylcyclohexan-1-yl radicals has four distinguishable structures (Figure 4.4). Unlike the reactant and product, the transition state structure has no internal rotation; instead it contains two rigid rings. The energetic information of the transition state structures is also given in Table 4.3, and we label these four structures **TS-1**, **TS-2**, **TS-3**, and **TS-4**, where **TS-1** and **TS-2** are the ones with lowest zero-point-inclusive energy at M06-2X/MG3S level. The structures of **C-a-g$^+$a$^-$** (j = 3) and **C-a-g$^+$** (l = 4) are the reactant and product structures that are connected with TS-1 by the MEP through TS-1; and the structures of **C-e-tx$^-$** (j = 5) and **C-e-t** (l = 3) are the reactant and product structures that are connected with TS-2 by the MEP through TS-2. As discussed in section 2.3, these are the structures that are used in the MCSI calculations.

Note that there is a second possible product, namely, *S*-2-ethylcyclohexan-1-yl radical, which is a mirror image of the *R* enantiomer. The transition states leading these two structures are also mirror images as illustrated in Figure 4.5. Therefore the rate

constants are the same for these two reactions. Here we only report the rate constant for the reaction to produce *R*-2-ethylcyclohexan-1-yl radical.

We employed eqs 3 and 4 to calculate the partition functions of the structures **TS-1**, **C-e-g$^-$c$^+$**, and **C-e-g$^+$** using the SS-HO and SS-T approximations, respectively. The conformational-rovibrational partition functions of 2-cycloheylethyl, *R*-2-ethylcyclohexan-1-yl, and their transition state were evaluated by both of the MS-X methods[15,16] (that is, using both X = LH and X = T) using eqs 1 and 2 reviewed in section 2.2. The MS-T method should provide more accurate partition functions than either the single-structural or MS-LH approximations. All the calculated partition functions of the reactant, product, and transition state are given in Tables 4.4−4.6.

For 2-cyclohexylethyl, the torsions around the $C^{(1)}$–$C^{(2)}$ and $C^{(2)}$–$C^{(3)}$ bonds are strongly coupled[15] (SC), thus we carried out the partition function calculations using the scheme[15] labeled NS:SC = 0:2, which denotes no nearly separable (NS) torsions and two strongly coupled ones. By contrast, *R*-2-ethylcyclohexan-1-yl has two nearly separable torsions; thus the partition calculation scheme for this case is NS:SC = 2:0. The transition state does not have any torsion; therefore MS-T reduces to MS-LH automatically. All the information of each reactant, product, and transition-state structure used for the partition function calculations carried out by the *MSTor* program is given Tables 4.7 and 4.8.

Table 4.4 shows that at low temperature (200−250 K), the partition functions calculated by MS-LH and MS-T for 2-cyclohexylethyl are within 5−9%, and as the temperature increases, the MS-LH approximation changes from being an underestimate to being an overestimate by a factor of up to 1.9. Table 4.5 shows that the deviations are

smaller for *R*-2-ethylcyclohexan-1-yl, where they are less than a factor of 1.4 over the entire temperature range. For the transition state, the MS-T and MS-LH partition functions are identical, and they are given in Table 4.6.

3.2. Path-averaged transmission coefficients and dynamic recrossing coefficients

Given that **TS-3** and **TS-4** have higher values of V_a^G than **TS-1** and **TS-2**, we average only over the reaction paths crossing **TS-1** (path 1) and **TS-2** (path 2) for the path-averaged transmission coefficients and dynamic recrossing coefficients calculation using eq 13. For path1, the MCSI method uses the structure **TS−1** as the transition state and stcutures **C-a-g$^+$a$^-$** and **C-a$^-$-g$^+$** as the reactant and product wells; and for path 2, **TS−2** is the transition state, and **C-e-tx$^-$** and **C-e-t** locate in the reactant and product wells. For each path, three stationary and six non-stationary Shepard points are used to obtain well converged V_{MEP} and V_a^G curves. The calculated V_{MEP} and V_a^G curves are displayed in Figures 4.6 and 4.7 by plotting $V_{MEP} - V^{\ddagger}$ and $V_a^G - V_a^{AG}$, where V_a^{AG} is the maximum of a V_a^G curve. The V_a^G curves are used to calculate transmission coefficients by the SCT approximation, and the results of path-averaged transmission coefficients and dynamic recrossing coefficients are listed in Table 4.9. Figure 4.6 shows that path 1 and path 2 have very similar V_{MEP} profiles in the range of *s* from −0.5 to 1.0 Å. But the potential energy profile along path 1 is a little thinner than than that along path 2 in the range 0.1 to 0.3 Å. From −0.5 to −1.0 Å, the V_{MEP} profile of path 2 is higher that that of path 1. The V_a^G curve of path 2 is smoother than that of

path 2, and the V_a^G curve of path 1 is thinner than that of path 2. Although the nonsmoothness of path 1 complicates the comparison of the two V_a^G curves, the region close to the saddle point seems trustable, and already in this region Figure 4.7 shows that path 1 is thinner than path 2. Consequently, κ_1 is around twelve, nine, five, two times, larger than κ_2 at 250 K, 300 K, 400 K, and 600 K, respectively. In addition, the dynamic recrossing coefficients Γ_1 and Γ_2 are close to each other. These calculations show that the reaction has a very large generalized transmission coefficient $\langle\gamma\rangle_2^{MP}$ below 500 K. In particular, it increases the TST rate constant by factors of 1.8, 6.2, 4350, and 2.15×10^5 at 1000, 600, 300, and 250 K, respectively. Above 1000 K, it increases the rate by less than 80%.

3.3. SS-TST and rate constants

We select TS-1 for the single-structure TST rate constant calculation, as discussed in section 2.3; thus k^* = 1 (**TS-1**) in the current study. The forward and reverse single-structural rate constants $k_{SS\text{-}HO,1}^{TST}$ and $k_{SS-T,1}^{TST}$ are calculated by the SS-HO and the SS-T approximations using eqs 12. The reactant and product for SS calculations are structures j = 1 and l = 1, which are **C-e-g$^-$c$^+$** and **C-e-g$^+$**. Both of these two rate constants only include one structure in the reactant and transition state, but they treat the internal rotations differently. Note that the SS-HO and SS-T two rate constants are based on the same transition state partition functions because there is no torsional motion in the transition state. But the reactant partition function has a different trend as

a function of temperature in these two approximations. The SS-T provides a more accurate result because it approaches the free rotor partition function at the high temperature limit. By contrast, SS-HO overestimates the partition function at high temperature. Therefore, the SS-HO approximation makes the rate constant smaller in the high-temperature range. The results are given in the first and second rate constant columns of Tables 4.10 and 4.11. The results, given in the SS columns of Table 4.10, show that the forward rate constant $k^{\mathrm{TST}}_{\mathrm{SS\text{-}HO},1}$ is larger than $k^{\mathrm{TST}}_{\mathrm{SS-T},1}$ below 1500 K, but the trend is opposite at higher temperature. Table 4.11 shows that the SS-HO and SS-T results agree much better for the reverse reaction with the largest deviation being a factor of 1.28 at 1000 K.

3.4 Multi-structural anharmonicity factors

Table 4.12 gives $F^{\ddagger}_{\mathrm{MS\text{-}X}}$, $F^{\mathrm{R}}_{\mathrm{MS\text{-}X}}$, and $F^{\mathrm{P}}_{\mathrm{MS\text{-}X}}$ (X = LH or T) for the transition state, reactant, and product at various temperatures. It shows that these multiple-structure factors $F^{\mathrm{Y}}_{\mathrm{MS\text{-}LH}}$ (Y = TS, R or P) are in the range 1.9−3.5, 2.2−11, and 1.7−3.8, respectively; and multi-structural torsional anharmonicity factors $F^{\mathrm{Y}}_{\mathrm{MS\text{-}T}}$ are spread over the range 1.9−3.5, 2.6−5.8, and 1.8−4.3, respectively. Note that the transition state has no torsion so that $F^{\ddagger}_{\mathrm{MS\text{-}LH}}$ and $F^{\ddagger}_{\mathrm{MS\text{-}T}}$ are identical. To understand the trends in the multi-structural torsional anharmonicity factor $F^{\mathrm{Y}}_{\mathrm{MS\text{-}T}}$, it is useful to factor it as

$$F^{\mathrm{Y}}_{\mathrm{MS\text{-}T}} = F^{\mathrm{Y}}_{\mathrm{MS\text{-}LH}} F^{\mathrm{Y}}_{\mathrm{tor}} \tag{18}$$

where $F_{\text{MS-LH}}^{\text{Y}}$ is defined in eq 5, and $F_{\text{tor}}^{\text{Y}}$ is called the torsional factor, which is defined as

$$F_{\text{tor}}^{\text{Y}} = \frac{Q_{\text{con-rovib}}^{\text{MS-T,Y}}(T)}{Q_{\text{con-rovib}}^{\text{MS-LH,Y}}(T)} \tag{19}$$

Figures 4.8, 4.9, and 4.10 show the two factors at various temperatures for the reactant, transition state, and product, respectively. It is found that $F_{\text{MS-LH}}^{\text{Y}}$ and $F_{\text{tor}}^{\text{Y}}$ show different trends with increasing temperature. $F_{\text{MS-LH}}^{\text{Y}}$ is a monotonically increasing function of temperature. As *T* increases, those structures with higher conformation energy make a greater contribution to the partition function $Q_{\text{con-rovib}}^{\text{MS-LH,Y}}(T)$. By contrast, $F_{\text{tor}}^{\text{Y}}$ for 2-cyclohexylethyl decays with increasing temperature above 500 K; and $F_{\text{tor}}^{\text{Y}}$ for *R*-2-ethylcyclohexan-1-yl first slightly increases with *T* in the temperature range 200−1000 K, and then it decrease above 1000 K. The transition state has no torsion; thus its $F_{\text{tor}}^{\text{Y}}$ is 1.0 across over the whole temperature range.

The reactant has the largest number of conformers; and as a consequence it has the largest multiple-structure factors over the whole 200 K to 2400 K temperature range. However, although the reactant has 22 conformers, $F_{\text{MS-LH}}^{\text{R}}$ is only 2.2−2.6 in the low-temperature and slightly above room-temperature range of 200−400 K although it rises to 10.95 at 2400 K. The fact that the multiple-structure factors are much less than the number of structures over the whole temperature range for reactant may be attributed to the fact such that the twisted-boat conformers are high in energy relative to

the global minimum structure. Nevertheless, their contribution to the total partition function increase with temperature, and they do play a significant role when temperature is high enough.

3.5. Final thermal rate constants and Arrhenius activation energy

We calculate the final MP-VTST/SCT thermal rate constant using eq 6. The results are given in the MSMP columns of Tables 4.10 and 4.11; Figures 4.11 and 4.12 display the calculated forward and reverse rate constants over the temperature range of 200−2400 K.

We note that the forward $k_{\text{MS-T}}^{\text{MP-CVT/SCT}}$ is lowers $k_{\text{MS-LH}}^{\text{MP-CVT/SCT}}$ by factors of 0.85 and 0.91at 200 and 600 K. But at 2400 K, $k_{\text{MS-T}}^{\text{MP-CVT/SCT}}$ is larger $k_{\text{MS-LH}}^{\text{MP-CVT/SCT}}$ by a factor of 2.2.

Table 4.13 shows the Arrhenius activation energy E_a calculated by eq 15 based on $k_{\text{MS-T}}^{\text{MP-CVT/SCT}}$. Table 4.13 shows that E_a increases with temperature but much more slowly than linearly in T, in disagreement with the linearity predicted by the usual fitting expression.[48] Thus we employ eq 16 to fit the rate constant for both forward and reverse reactions, and the fitting plots are displayed in Figures 4.11 and 4.12. We obtain the following fitting parameters: $A = 1.00\times10^{8}$ s^{-1}, $n = 3.30$, $E = 11.87$ kcal/mol, and $T_0 = 182.83$ K for the forward reaction; $A = 1.55\times10^{7}$ s^{-1}, $n = 3.94$, $E = 12.18$ kcal/mol, and $T_0 = 171.11$ K for the reverse reaction. The results are also listed in Table 4.13. It shows that the Arrhenius activation energy E_a predicted using eq 15 agree very well

with that calculated using eq 17 in the temperature range 300−1500 K for both forward and reverse reactions. At 2000–2400 K, the deviation gets large.

4. Conclusion

We proposed a new formulation of VTST called MP-VTST. It is based on the recent MS-VTST formulation, but it extends that formulation to incorporate multiple paths in the calculation of the tunneling transmission coefficient and the variational effect. To demonstrate MP-VTST, we apply it to calculate both the forward and reverse reaction rate constant of the 1,4-hydrogen shift reaction of 2-cyclohexylethyl radical in the temperature range from 200 K to 2400 K. This reaction has 23 atoms (C_8H_{15}), and a major challenge in predicting the thermal rate constant in the current study is that the reactant, product, and transition state each have many structures that make the potential energy surface and partition functions used in the rate calculations very complex. We average over two reaction paths and use multi-configuration Shepard interpolation (MCSI) to obtain a semi-global potential energy surface, V_{MEP}, and $V_{\mathrm{a}}^{\mathrm{G}}$ potential energy curves for each of the reaction path. The MCSI method uses molecular mechanics to facilitate an efficient interpolation of density functional calculations. MCSI provides, with only nine electronic structure Hessians, a good enough interpolation of the 63-dimensional potential energy surface to calculate path-averaged generalized transmission coefficients using the SCT approximation. Then the multi-structural anharmonicity factors, which include both multiple-structure and torsional anharmonicity effects were evaluated using MS-T approximation by using the *MSTor* program. Finally, the thermal rate constants were the product of the SS-VTST rate

constant with the harmonic approximation, path-averaged generalized transmission coefficient, and the multi-structural anharmonicity factors.

Table 4.1 Calculated forward and reverse zero-point-exclusive barrier heights and energies of reaction for the 1,4-hydrogen shift isomerization of 2-cyclohexylethyl radical as calculated by various methods (in kcal/mol)

Method[a]	$V_f^{\ddagger}$	$V_r^{\ddagger}$	ΔE
CCSD(T)-F12a/jul-cc-pVTZ//M	25.63	27.75	−2.12
BMC-CCSD//M	25.66	27.51	−1.85
MCG3-TS//M	25.66	27.50	−1.84
M06-2X/MG3S	27.07	29.28	−2.21
M06-2X/aug-cc-pVTZ	27.14	29.36	−2.23
M06-2X/maug-cc-pVTZ	27.14	29.33	−2.19
M06-2X/def2-TZVP	27.04	29.20	−2.16
M08-SO/MG3S	26.73	29.16	−2.43
M08-SO/aug-cc-pVTZ	26.87	29.42	−2.55
M08-SO/maug-cc-pVTZ	26.79	29.29	−2.51
M08-SO/def2-TZVP	26.74	29.16	−2.42
M06/6-31+G(d,p)	26.09	28.61	-2.52

[a] //M is shorthand for //M06-2X/MG3S.

Table 4.2 Labeling of structures[a]

C	chair	
B	twisted boat	
e	equatorial	
a	axial	
	Abbreviation	dihedral angle range (deg)
antiperiplanar	$\mathbf{a}^{+}$	[140,163]
	$\mathbf{a}^{-}$	[-163, –140]
gauche	$\mathbf{g}^{+}$	[55, 80]
	$\mathbf{g}^{-}$	[–80, –55]
syn	$\mathbf{x}^{+}$	[80, 130]
	$\mathbf{x}^{-}$	[–130, –80]
synclinal	$\mathbf{c}^{+}$	[30, 50]
	$\mathbf{c}^{-}$	[–50, –30]
trans	**t**	[–173, –180] and [180, 173]

[a]The dihedral angles used for torsions are and H–$C^{(3)}$–$C^{(2)}$–$C^{(1)}$ and $C^{(3)}$–$C^{(2)}$–$C^{(1)}$–H for 2-cyclohexylethyl; the dihedral angle used for torsion are and H–$C^{(3)}$–$C^{(2)}$–$C^{(1)}$ for *R*-2-ethylcyclohexan-1-yl.

Table 4.3 The sequence number and energy[a] (kcal/mol) of structures of 2-cyclohexylethyl radical, *R*-2-ethylcyclohexan-1-yl radical, and the transition state

structures	number	energy	
		V	$V + \varepsilon^{G}$
	2-cyclohexylethyl radical		
C-e-g$^-$c$^+$, C-e-g$^+$c$^-$	$j = 1, j = 2$	0	129.46
C-a-g$^+$a$^+$, C-a-g$^-$a$^-$	$j = 3, j = 4$	1.42	133.06
C-e-tx$^-$	$j = 5$	0.50	130.66
C-a-tx$^-$	$j = 6$	3.86	137.57
B-e-g$^-$a$^+$, B-e-g$^+$a$^-$	$j = 7, j = 8$	6.06	141.60
B-e-g$^-$a$^-$, B-e-g$^+$a$^+$	$j = 9, j = 10$	6.14	141.76
B-a-tx$^+$, B-a-tx$^+$	$j = 11, j = 12$	6.48	142.71
B-e-g$^-$a$^+$, B-e-g$^+$a$^-$	$j = 13, j = 14$	6.55	142.62
B-e-ts$^+$, B-e-ts$^-$	$j = 15, j = 16$	6.63	142.88
B-e-ta$^-$, B-e-ta$^+$	$j = 17, j = 18$	6.82	143.17
B-a-g$^-$c$^+$, B-a-g$^+$c$^-$	$j = 19, j = 20$	7.09	143.94
B-a-g$^+$a$^+$, B-a-g$^-$a$^-$	$j = 21, j = 22$	7.43	144.59
	R-2-ethylcyclohexan-1-yl		
C-e-g$^+$	$l = 1$	–2.21	127.44
C-e-g$^-$	$l = 2$	–2.14	127.82
C-e-t	$l = 3$	–1.94	128.56
C-a-g$^+$	$l = 4$	–1.21	130.81
C-a-g$^-$	$l = 5$	–0.69	132.49
C-a-t	$l = 6$	0.72	136.78
B-a-g$^+$	$l = 7$	2.37	141.41
B-a-g$^-$	$l = 8$	2.48	141.73
B-a-t	$l = 9$	4.14	146.82
	Transition state		
TS-1	$k = 1$	27.07	154.70
TS-2	$k = 2$	27.34	155.33
TS-3	$k = 3$	31.52	167.92
TS-4	$k = 4$	32.74	171.57

[a]V is the M06-2X/MG3S zero-point-exclusive energy of the structures, and $V + \varepsilon^{G}$ is the zero-point-inclusive energy that is calculated by adding the zero-point energy which is calculated using M06-2X frequencies multiplied by a scale factor from Ref. 114. All energies in this table are relative to the classical equilibrium geometry of the j = 1 structure of the reactant.

Table 4.4 Calculated conformational−rotational−vibrational partition function of 2-cyclohexylethyl radical using single-structural and multi-structural methods[a]

T (K)	SS-HO[b]	SS-T[c]	MS-LH	MS-T[d]
200	8.62E−136	1.02E−135	1.90E−135	2.24E−135
250	6.60E−107	7.89E−107	1.53E−106	1.82E−106
298.15	4.58E−88	5.50E−88	1.11E−87	1.33E−87
300	1.85E−87	2.22E−87	4.49E−87	5.38E−87
400	1.06E−62	1.26E−62	2.79E−62	3.31E−62
600	1.01E−36	1.16E-36	3.12E−36	3.52E−36
1000	3.72E−13	3.89E-13	1.64E−12	1.57E−12
1500	1.94E+02	1.83E+02	1.31E+03	9.86E+02
2000	4.01E+11	3.40E+11	3.68E+12	2.24E+12
2400	1.65E+17	1.29E+17	1.81E+18	9.49E+17

[a] All partition functions in this table have their zero of energy at the bottom of the potential well for the *j* = 1 structure of 2-cyclohexylethyl.

[b] The partition function of the structure *j* = 1, **C-e-g$^-$c$^+$** calculated using SS-HO approximation.

[c] The partition function of the structure *j* = 1, **C-e-g$^-$c$^+$** calculated using SS-T approximation.

[d] The MS-T partition function is calculated using the *MSTor* program with NS : SC = 0 : 2.

Table 4.5 Calculated conformational−rotational−vibrational partition function of *R*-2-ethylcyclohexan-1-yl radical using single-structural and multi-structural methods[a]

T (K)	SS-HO[b]	SS-T[c]	MS-LH	MS-T[d]
200	6.92E−136	7.45E−136	1.16E−135	1.25E−135
250	6.05E−107	6.67E−107	1.08E−106	1.19E−106
298.15	4.58E−88	5.17E−88	8.65E−88	9.75E−88
300	1.86E−87	2.10E−87	3.52E−87	3.97E−87
400	1.19E−62	1.40E−62	2.44E−62	2.89E−62
600	1.26E−36	1.59E−36	2.92E−36	3.74E−36
1000	4.89E−13	6.50E−13	1.35E−12	1.83E−12
1500	2.61E+02	3.36E+02	8.38E+02	1.10E+03
2000	5.42E+11	6.50E+11	1.93E+12	2.35E+12
2400	2.23E+17	2.51E+17	8.46E+17	9.61E+17

[a] All partition functions in this table have their zero of energy at the bottom of the potential well for the *l* = 1 structure of *R*-2-ethylcyclohexan-1-yl.

[b] The partition function of the structure *l* = 1, **C-e-g**$^+$ calculated using SS-HO approximation.

[c] The partition function of the structure *l* = 1, **C-e-g**$^+$ calculated using SS-T approximation.

[d] The MS-T partition function is calculated using the *MSTor* program with NS : SC = 2 : 0.

Table 4.6 Calculated conformational−rotational−vibrational partition function of the transition state using single-structural and multi-structural methods[a]

T (K)	SS-HO[b,c]	MS-LH[d]
200	2.70E−134	5.00E−134
250	6.31E−106	1.20E−105
298.15	1.94E−87	3.74E−87
300	7.63E−87	1.47E−86
400	1.41E−62	2.80E−62
600	3.90E−37	8.16E−37
1000	4.70E−14	1.13E−13
1500	1.29E+01	3.69E+01
2000	1.83E+10	5.96E+10
2400	6.03E+15	2.14E+16

[a] All partition functions in this table have their zero of energy at the bottom of the potential well for the k = 1 structure of the transition state.

[b] The partition function of the **TS-1** calculated using SS-HO approximation.

[c] For the transition state, the partition function of the **TS-1** calculated using SS-T approximation is the same as that by SS-HO approximation, and so it is not included in the table.

[d] For the transition state the MS-T partition function is the same as that by MS-LH approximation, and so only one of these approximations is shown.

Table 4.7 Information used for 2-cyclohexylethyl radical partition function using the MS-T method[a]

Torsion	$\overline{\omega}$	I	W	M
		Structures 1 and 2		
C(1)–C(2)	136.01	1.72	306.77	2.48
C(2)–C(3)	114.00	18.28	2291.71	2.48
		Structures 3 and 4		
C(1)–C(2)	144.55	1.72	349.05	2.47
C(2)–C(3)	100.02	20.23	1968.11	2.47
		Structure 5		
C(1)–C(2)	115.69	1.71	237.70	2.39
C(2)–C(3)	108.66	19.65	2410.02	2.39
		Structure 6		
C(1)–C(2)	190.47	1.71	631.82	2.41
C(2)–C(3)	88.82	19.76	1591.87	2.41
		Structures 7 and 8		
C(1)–C(2)	130.684	1.72	73.186	4.88
C(2)–C(3)	124.278	17.756	683.117	4.88
		Structures 9 and 10		
C(1)–C(2)	134.36	1.72	79.64	4.81
C(2)–C(3)	124.70	18.27	728.28	4.81
		Structures 11 and 12		
C(1)–C(2)	134.12	1.71	156.90	3.41
C(2)–C(3)	132.38	19.77	1767.06	3.41
		Structures 13 and 14		
C(1)–C(2)	106.47	1.72	88.60	3.61
C(2)–C(3)	122.80	18.15	1245.58	3.61
		Structures 15 and 16		
C(1)–C(2)	124.81	1.71	82.48	4.38
C(2)–C(3)	121.76	19.59	898.19	4.38
		Structures 17 and 18		
C(1)–C(2)	93.76	1.72	32.34	5.26
C(2)–C(3)	144.74	19.23	863.52	5.26
		Structures 19 and 20		
C(1)–C(2)	147.02	1.72	179.83	3.50
C(2)–C(3)	120.30	20.64	1446.64	3.50
		Structures 21 and 22		
C(1)–C(2)	142.06	1.72	168.89	3.49
C(2)–C(3)	119.84	19.55	1367.49	3.49

[a] We used NS:SC=0:2 and M06-2X/MG3S for this table. The units are cm^{-1} for torsional barrier heights W and frequencies $\overline{\omega}$. The unit is amu $Å^2$ for internal moments of inertia, I; and the local periodicity M is unitless. See Ref. 97 for details of the method.

Table 4.8 Information used for *R*-2-ethylcyclohexan-1-yl radical partition function using the MS-T method[a]

Torsion	$\overline{\omega}$	*I*	*W*	*M*
		Structure 1		
C(1)–C(2)	204.38	3.07	846.24	3
C(2)–C(3)	115.60	20.21	1780.14	3
		Structure 2		
C(1)–C(2)	227.97	3.07	1052.35	3
C(2)–C(3)	99.95	20.14	1326.05	3
		Structure 3		
C(1)–C(2)	212.94	3.10	925.10	3
C(2)–C(3)	105.96	20.75	1535.79	3
		Structure 4		
C(1)–C(2)	227.31	3.08	1048.25	3
C(2)–C(3)	90.31	22.53	1210.96	3
		Structure 5		
C(1)–C(2)	230.12	3.07	1071.97	3
C(2)–C(3)	87.30	22.38	1124.07	3
		Structure 6		
C(1)–C(2)	277.09	3.10	1567.09	3
C(2)–C(3)	115.27	21.56	1888.53	3
		Structure 7		
C(1)–C(2)	226.07	3.08	1038.02	3
C(2)–C(3)	98.84	21.92	1411.65	3
		Structure 8		
C(1)–C(2)	226.59	3.07	1039.77	3
C(2)–C(3)	99.92	22.83	1502.11	3
		Structure 9		
C(1)–C(2)	249.374	3.09	1268.04	3
C(2)–C(3)	106.41	21.78	1624.98	3

[a] We used NS:SC=2:0 and M06-2X/MG3S for this table. The units are cm^{-1} for torsional barrier heights *W* and frequencies $\overline{\omega}$. The unit is amu $Å^2$ for internal moments of inertia, *I*; and the local periodicity *M* is unitless. See Ref. 97 for details of the method.

Table 4.9 Dynamic ecrossing and transimission coefficients calculated using samll-cruvature tunnling approximation at various temperatures based on reaction paths 1 and 2

T / K	$\Gamma_k(T)$		$\kappa_k(T)$		$\langle\Gamma(T)\kappa(T)\rangle_2$
	Path 1	Path 2	Path 1	Path 2	
200	8.97E−01	9.60E−01	7.78E+08	3.65E+07	1.89E+08
250	9.05E−01	9.69E−01	6.92E+05	5.96E+04	2.15E+05
298.15	9.07E−01	9.73E−01	1.36E+04	1.59E+03	4.86E+03
300	9.06E−01	9.74E−01	1.21E+04	1.43E+03	4.35E+03
400	9.12E−01	9.84E−01	1.88E+02	4.03E+01	8.56E+01
600	9.07E−01	9.84E−01	9.59E+00	4.67E+00	6.22E+00
1000	9.05E−01	9.85E−01	2.23E+00	1.72E+00	1.84E+00
1500	8.98E−01	9.84E−01	1.42E+00	1.27E+00	1.26E+00
2000	8.99E−01	9.82E−01	1.21E+00	1.15E+00	1.11E+00
2400	8.96E−01	9.82E−01	1.14E+00	1.10E+00	1.05E+00

Table 4.10 Forward SS-TST and MP-VTST thermal rate constants (in s^{-1}) for the 1,4-hydrogen shift isomerization reaction of 2-cyclohexylethyl radical to produce *R*-2-ethylcyclohexan-1-yl radical at various temperatures[a]

T (K)	$k^{\mathrm{TST}}_{\mathrm{SS\text{-}HO},1}$	$k^{\mathrm{TST}}_{\mathrm{SS\text{-}T},1}$	$k^{\mathrm{MP\text{-}CVT/SCT}}_{\mathrm{MS\text{-}LH}}$	$k^{\mathrm{MP\text{-}CVT/SCT}}_{\mathrm{MS\text{-}T}}$
200	4.57E−15	3.91E−15	7.26E−07	6.21E−07
250	8.59E−10	7.24E−10	1.52E−04	1.28E−04
298.15	2.16E−06	1.82E−06	8.37E−03	7.08E−03
300	2.78E−06	2.34E−06	9.66E−03	8.12E−03
400	6.67E−02	5.68E−02	4.30E+00	3.69E+00
600	1.62E+03	1.45E+03	6.82E+03	6.20E+03
1000	5.60E+06	5.54E+06	5.57E+06	6.09E+06
1500	3.52E+08	4.00E+08	1.87E+08	2.72E+08
2000	2.86E+09	3.70E+09	1.13E+09	2.10E+08
2400	8.23E+09	1.19E+10	2.81E+09	6.20E+09

[a] Includes variational effects, torsional anharmonicity, and tunneling.

Table 4.11 SS-TST and MP-VTST thermal rate constants (in s^{-1}) for the 1,4-hydrogen shift isomerization reaction of *R*-2-ethylcyclohexan-1-yl radical to produce 2-cyclohexylethyl radical at various temperatures[a]

T (K)	$k^{\mathrm{TST}}_{\mathrm{SS\text{-}HO},1}$	$k^{\mathrm{TST}}_{\mathrm{SS\text{-}T},1}$	$k^{\mathrm{MP\text{-}CVT/SCT}}_{\mathrm{MS\text{-}LH}}$	$k^{\mathrm{MP\text{-}CVT/SCT}}_{\mathrm{MS\text{-}T}}$
200	7.02E−17	6.57E−17	1.46E−08	1.37E−08
250	2.66E−11	2.43E−11	6.09E−06	5.55E−06
298.15	1.05E−07	9.42E−08	5.21E−04	4.68E−04
300	1.37E−07	1.22E−07	6.10E−04	5.47E−04
400	5.88E−03	5.04E−03	4.88E−01	4.18E−01
600	2.57E+02	2.08E+02	1.44E+03	1.16E+03
1000	1.45E+06	1.14E+06	2.31E+06	1.80E+06
1500	1.18E+08	9.77E+07	1.32E+08	1.10E+08
2000	1.09E+09	1.00E+09	1.11E+09	1.03E+09
2400	3.36E+09	3.36E+09	3.31E+09	3.38E+09

[a] Includes variational effects, torsional anharmonicity, and tunneling. Note that the reaction in this table is the reverse of that in Table 4.10.

Table 4.12 Multiple-structure anharmonicity factors $F_{\text{MS-LH}}$ and multi-structural torsional anharmonicity factors $F_{\text{MS-T}}$ with respect to the structures **TS-1** for the transition state, **C-e-g^{+}g^{-}** for the reactant, and **C-e-g^{+}** for the product

T (K)	$F^{\ddagger}_{\text{MS-X}}$		$F^{\text{R}}_{\text{MS-X}}$		$F^{\text{P}}_{\text{MS-X}}$	
	HO	T	HO	T	HO	T
200	1.85	1.85	2.20	2.60	1.68	1.80
250	1.90	1.90	2.31	2.77	1.79	1.97
298.15	1.93	1.93	2.42	2.90	1.89	2.13
300	1.93	1.93	2.42	2.91	1.89	2.13
400	1.99	1.99	2.64	3.13	2.06	2.44
600	2.09	2.09	3.08	3.48	2.32	2.97
1000	2.40	2.40	4.41	4.22	2.76	3.73
1500	2.85	2.85	6.75	5.08	3.21	4.21
2000	3.26	3.26	9.17	5.58	3.56	4.34
2400	3.54	3.54	10.95	5.75	3.79	4.30

Table 4.13 Forward and reverse activation energy (in kcal/mol) calculated by MP-VTST for the 1,4-hydrogen shift isomerization reaction of 2-cyclohexylethyl radical at various temperatures and for the reverse reaction

T (K)	300	400	600	1000
forward (MP-CVT/SCT)[a]	13.2/13.6	15.5/16.5	19.2/19.0	21.9/21.4
reverse (MP-CVT/SCT)[a]	14.4/14.9	16.9/17.7	20.4/20.2	23.6/22.9
T (K)	1500	2000	2300	2400
forward (MP-CVT/SCT)[a]	23.4/24.0	24.0/26.8	26.1/28.6	26.3/29.2
reverse (MP-CVT/SCT)[a]	26.2/26.2	26.4/29.6	28.2/31.8	28.4/32.5

[a] The first number is calculated using eq 15 and the second one is calculated using eq 17 based on the fitting results.

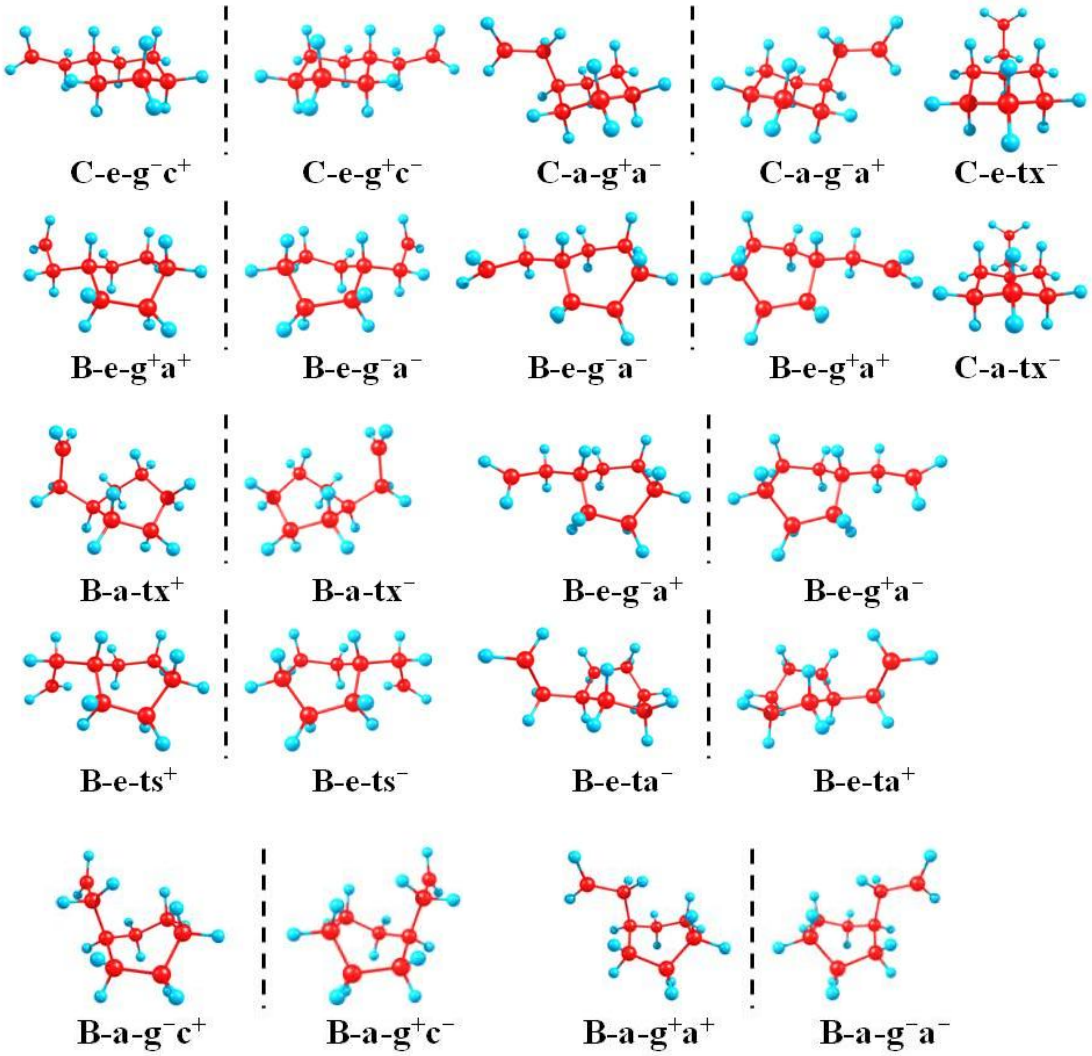

Figure 4.1. 22 structures of 2-cyclohexylethyl radical. Note that another name for this species is 2-cyclohexylethan-1-yl radical.

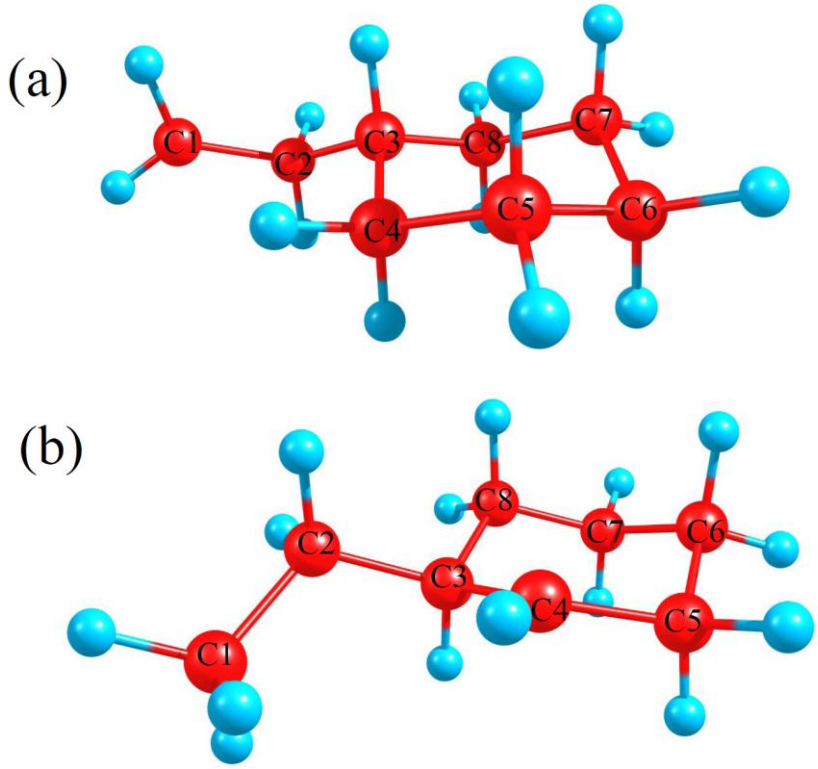

Figure 4.2 Numbering scheme for reactant (a) and product (b).

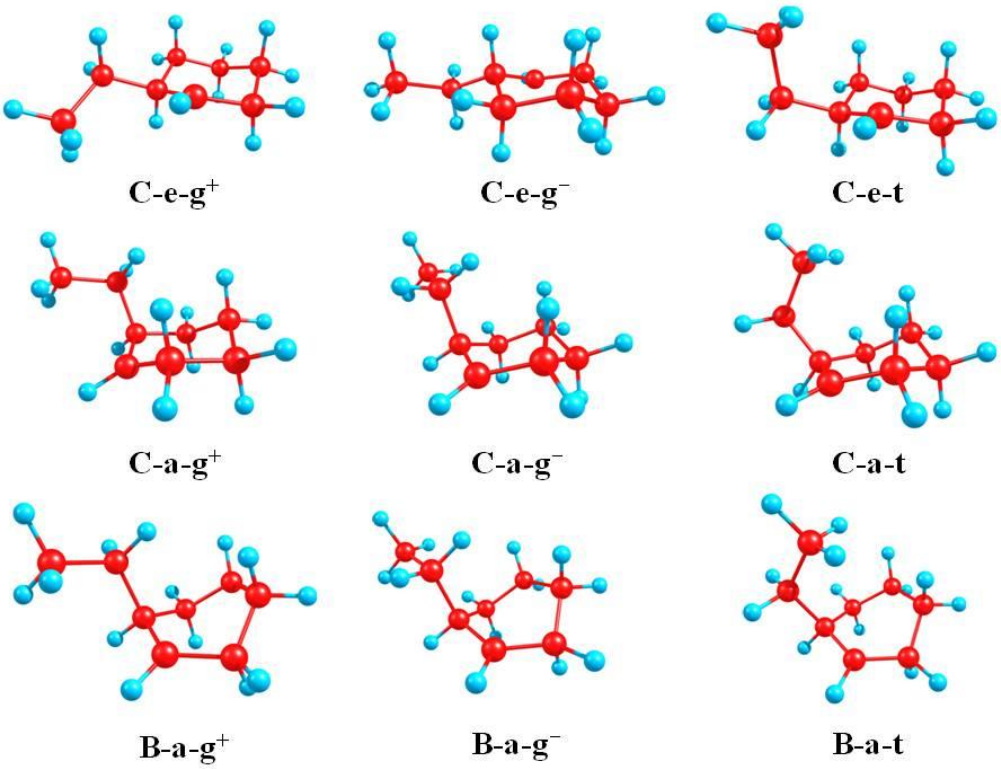

Figure 4.3 Nine structures of *R*-2-ethylcyclohexan-1-yl radical.

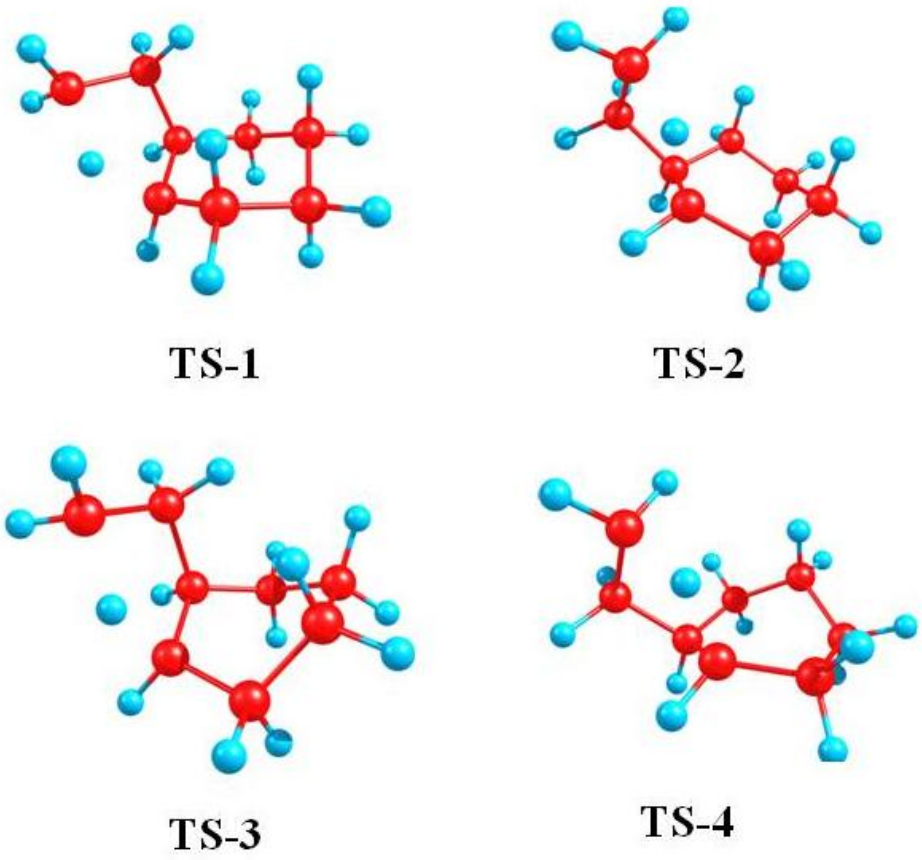

Figure 4.4 Four structures of transition state.

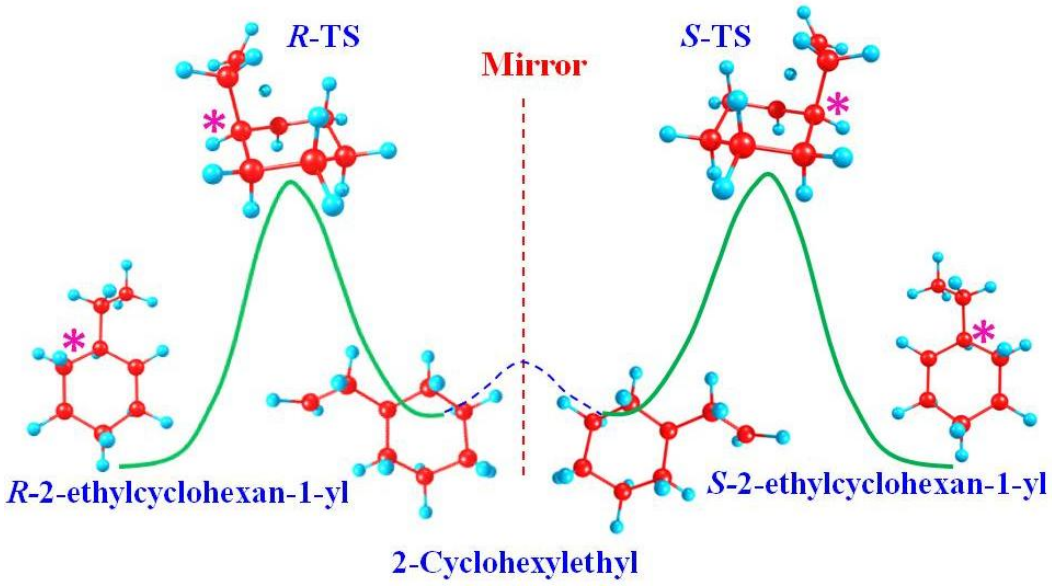

Figure 4.5 Mirror images of transition states and products in the reaction path.

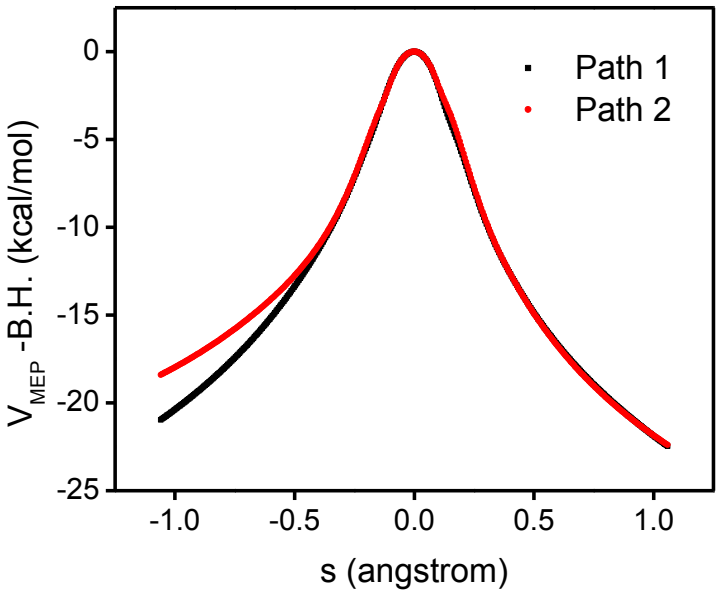

Figure 4.6 Calculated V_{MEP} vs. the reaction coordinate *s* (scaled to a reduced mass of one amu) for the 1,4-hydrogen shift isomerization reaction of 2-cyclohexylethyl radical. This figure is based on M06/6-31+G(d,p). B. H. represents the barrier height.

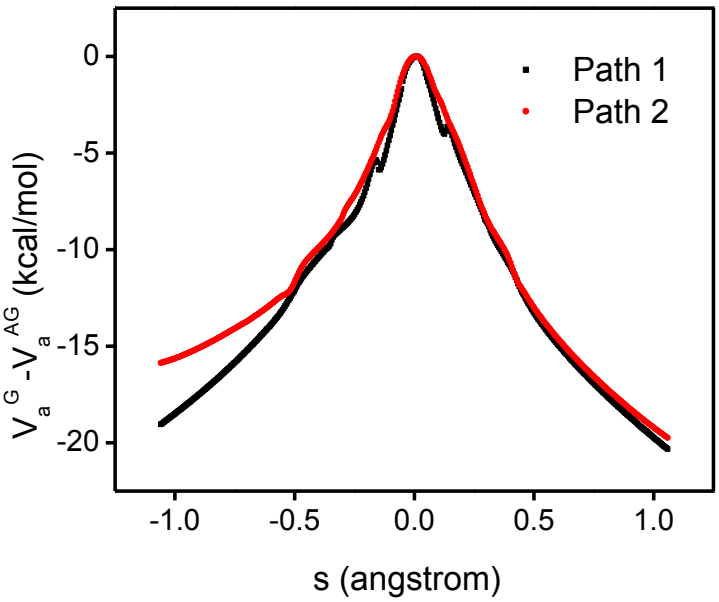

Figure 4.7 Calculated ground-state vibrationally adiabatic potential (V_a^G) vs. the reaction coordinate *s* (scaled to a reduced mass of one amu) for the 1,4-hydrogen shift isomerization reaction of 2-cyclohexylethyl radical. This figure is based on M06/6-31+G(d,p).

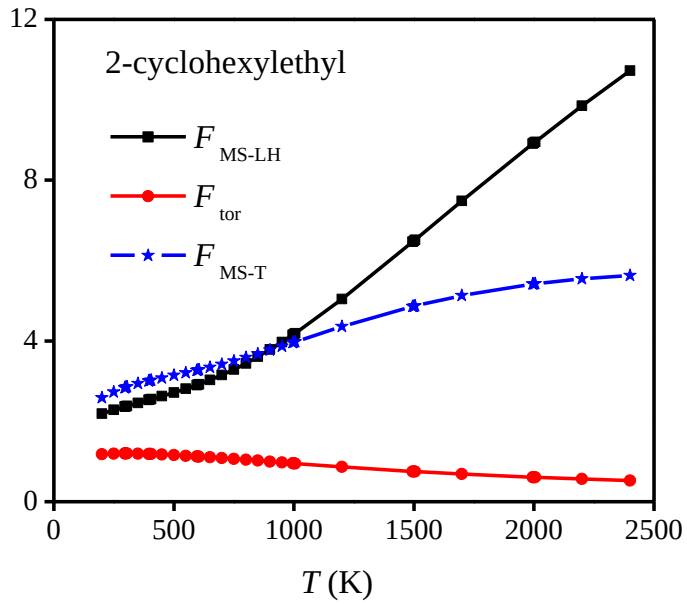

Figure 4.8 Multi-structural anharmonicity factors (blue), multiple-structure factors (black), and torsional factors (red) of 2-cyclohexylethyl at various temperatures.

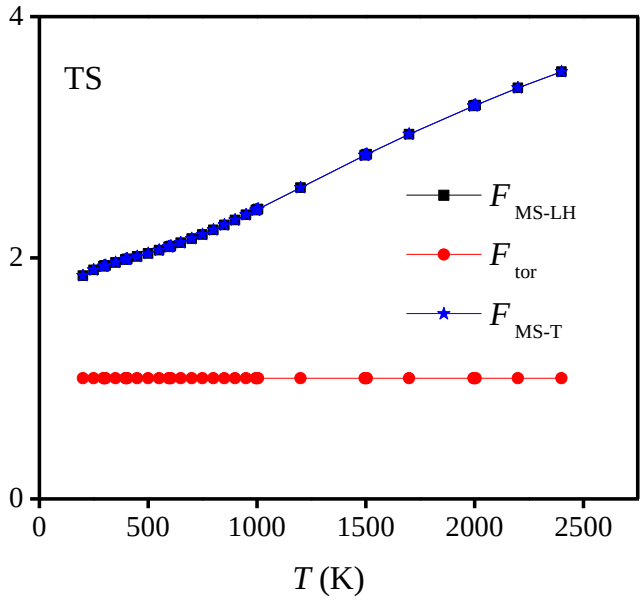

Figure 4.9 Multi-structural anharmonicity factors (blue), multiple-structure factors (black), and torsional factors (red) of the transition state (TS) at various temperatures *T*. Note that multi-structural anharmonicity factors (blue) and multiple-structure factors (black) are identical in this case.

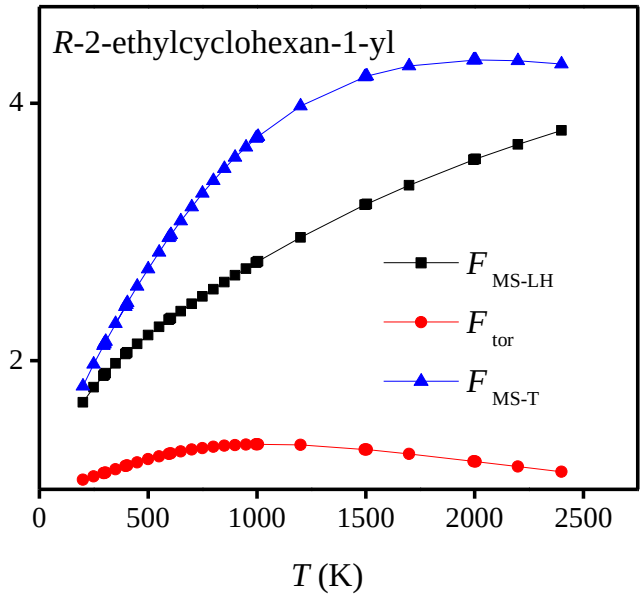

Figure 4.10 Multi-structural anharmonicity factors (blue), multiple-structure factors (black), and torsional factors (red) of *R*-2-ethylcyclohexan-1-yl at various temperatures.

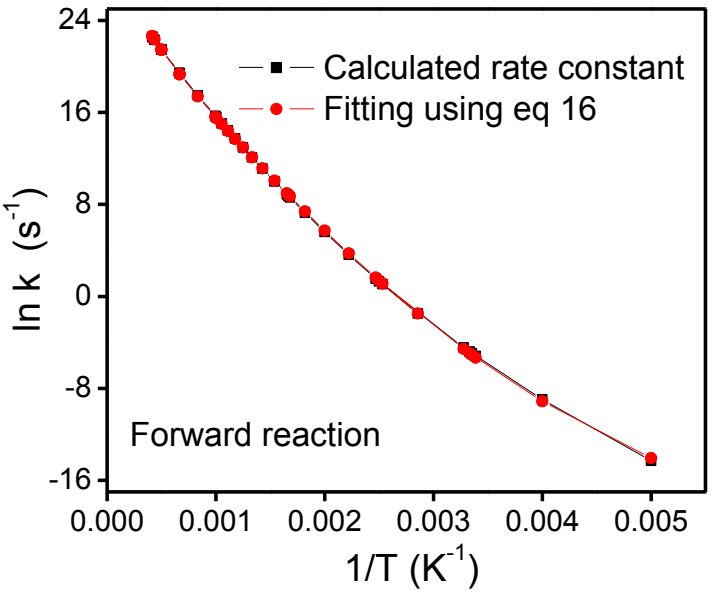

Figure 4.11 Arrhenius plots of calculated forward rate constant $k_{\text{MS-T}}^{\text{MP-CVT/SCT}}$ calculated by MP-VTST (black curve).

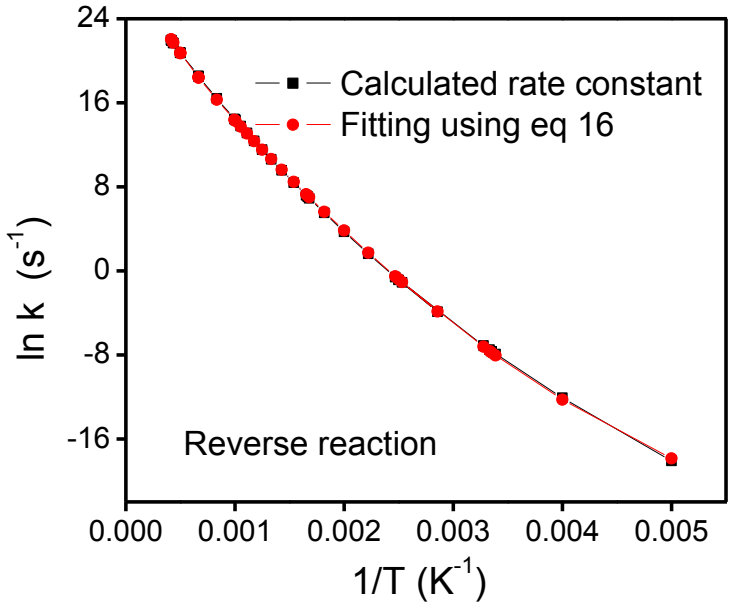

Figure 4.12 Arrhenius plots of calculated reverse rate constant $k_{\text{MS-T}}^{\text{MP-CVT/SCT}}$ calculated by MP-VTST (black curve).

Bibliography

(1) R. P. Feynman and A. R. Hibbs, *Quantum Mechanics and Path Integrals*, Ed.; McGraw-Hill, New York, 1965.
(2) R. P. Feynman, *Statistical Mechanics*, Ed.; Benjamin, Reading, MA, 1972.
(3) V. A. Lynch, S. L. Mielke and D. G. Truhlar, *J. Chem. Phys.*, 2004, **121**, 5148.
(4) V. A. Lynch, S. L. Mielke and D. G. Truhlar, *J. Phys. Chem. A*, 2005, **109**, 10092; 2006, **110**, 5965(E).
(5) S. Chempath, C. Predescu and A. T. Bell, *J. Chem. Phys.*, 2006, **124**, 234101.
(6) D. R. Herschbach, *J. Chem. Phys.*, 1959, **31**, 91.
(7) D. G. Truhlar, *J. Comput. Chem.*, 1991, **12**, 266.
(8) J. Gang, M. J. Pilling and S. H. Robertson, *J. Chem. Soc. Faraday Trans.*, 1996, **92**, 3509.
(9) A. L. L. East and L. Radom, *J. Chem. Phys.*, 1997, **106**, 6655.
(10) R. B. McClurg, R. C. Flagan and W. A. Goddard, III, *J. Chem. Phys.*, 1997, **106**, 6675; 1999, **111**, 7165(E).
(11) W. Witschel and C. Hartwigsen, *Chem. Phys. Lett.*, 1997, **273**, 304.
(12) P. Y. Ayala and H. B. Schlegel, *J. Chem. Phys.*, 1998, **108**, 2314.
(13) Y.-Y. Chuang and D. G. Truhlar, *J. Chem. Phys.*, 2000, **112**, 1221; 2004, **121**, 7036(E); 2006, **124**, 179903(E).
(14) B. A. Ellingson, V. A. Lynch, S. L. Mielke and D. G. Truhlar, *J. Chem. Phys.*, 2006, **125**, 084305.
(15) A. C. P. Bitencourt, M. Ragni, G. S. Maciel, V. Aquilanti and F. V. Prudente, *J. Chem. Phys.*, 2008, **129**, 154316.
(16) S. Sharma, S. Raman and W. H. Green, *J. Phys. Chem. A*, 2010, **114**, 5689.
(17) D. Gruzman, A. Karton and J. M. L. Martin, *J. Phys. Chem. A*, 2009, **113**, 11974.
(18) T. H. Lay, L. N. Krasnoperov, C. A. Venanzi, J. W. Bozzelli and N. V. Shokhirev, *J. Phys. Chem.*, 1996, **100**, 8240.
(19) T. Yamada, T. H. Lay and J. W. Bozzelli, *J. Phys. Chem. A*, 1998, **102**, 7286.
(20) T. Yamada, J. W. Bozzelli and R. J. Berry, *J. Phys. Chem. A*, 1999, **103**, 5602.
(21) K. S. Pitzer and W. D. Gwinn, *J. Chem. Phys.*, 1942, **10**, 428.
(22) B. M. Wong and W. H. Green, *Mol. Phys.*, 2005, **103**, 1027.
(23) T. F. Miller, III and D. C. Clary, *J. Chem. Phys.*, 2002, **116**, 8262.
(24) V. Van Speybroeck, D. V. Neck and M. Waroquier, *J. Phys. Chem. A*, 2002, **106**, 8945.
(25) P. Vansteenkiste, D. Van Neck, V. Van Speybroeck and M. Waroquier, *J. Chem. Phys.*, 2006, **124**, 044314.
(26) D. A. McQuarrie, *Statistical Mechanics* Ed.; Harper & Row, New York, 1973.
(27) T. F. Miller, III and D. C. Clary, *Mol. Phys.*, 2005, **103**, 1573
(28) M. Tafipolsky and R. Schmid, *J. Comput. Chem.*, 2005, **26**, 1579.
(29) Y. K. Sturdy and D. C. Clary, *Phys. Chem. Chem. Phys.*, 2007, **9**, 2397.
(30) S. W. Benson, *Thermochemical Kinetics*, 2nd, Ed.; Wiley-Interscience, New York, 1976.
(31) H. E. O'Neal and S. W. Benson, *Int. J. Chem. Kinet.*, 1969, **1**, 221.

(32) H. E. O'Neal and S. W. Benson, in *Free Radicals*, ed. J. H. Koshi, Wiley, New York, 1973, pp. 275.
(33) N. Cohen, *J. Phys. Chem.*, 1992, **96**, 9052.
(34) T. H. Lay, J. W. Bozzelli, A. M. Dean and E. R. Ritter, *J. Phys. Chem.*, 1995, **99**, 14514.
(35) K. K. Irikura, in *Computational Thermochemistry*, ed. K. K. Irikura and D. J. Frurip, ACS Symposium Series Vol. 677, 1998, pp. 402.
(36) V. Van Speybroeck, R. Ganib and R. J. Meier, *Chem. Soc. Rev.*, 2010, **39**, 1764.
(37) K. S. Pitzer, *J. Chem. Phys.*, 1940, **8**, 711.
(38) W. J. Taylor, *J. Chem. Phys.*, 1948, **16**, 257.
(39) P. J. Flory and R. L. Jernigan, *J. Chem. Phys.*, 1965, **42**, 3509.
(40) R. A. Scott and H. A. Scheraga, *J. Chem. Phys.*, 1966, **44**, 3054.
(41) R. Janoschek and J. Kalcher, *Anorg. Allg. Chem.*, 2002, **628**, 2724.
(42) G. L. Dirichlet, *J. Reine Angew. Math.*, 1850, **40**, 209.
(43) G. Voronoi, *J. Reine Angew. Math.*, 1907, **133**, 97.
(44) F. Aurenhammer, *ACM Computing Surveys*, 1991, **23**, 345.
(45) G. Katzer and A. F. Sax, *J. Comput. Chem.*, 2005, **26**, 1438.
(46) K. S. Pitzer, *J. Chem. Phys.*, 1946, **14**, 239.
(47) J. E. Kilpatrick and K. S. Pitzer, *J. Chem. Phys.*, 1949, **17**, 1064.
(48) T. Miyazawa and K. Fukushima, *J. Mol. Spectrosc.*, 1965, **15**, 308.
(49) H. Bonadeo, E. D'Alessio and E. Silberman, *J. Mol. Spectrosc.*, 1967, **22**, 402.
(50) G. Keresztury, A.-Y. Wang and J. R. Durig, *Spectrochimica Acta A*, 1992, **48**, 199.
(51) G. Tasi, F. Mizukami, I. Palinko, J. Csontos, W. Gyorffy, P. Nair, K. Maeda, M. Toba, S.-i. Niwa, Y. Kiyozumi and I. Kiricsi, *J. Phys. Chem. A*, 1998, **102**, 7698.
(52) D. Bond, *J. Phys. Chem. A*, 2008, **112**, 1656.
(53) P. Pulay, *Mol. Phys.*, 1969, **17**, 197.
(54) G. Fogarasi and P. Pulay, *Molecular Vibrational Spectra and Structure*, Ed.; Elsevier, Amsterdam, 1985.
(55) C. F. Jackels, Z. Gu and D. G. Truhlar, *J. Chem. Phys.*, 1995, **102**, 3188.
(56) K. A. Nguyen, C. F. Jackels and D. G. Truhlar, *J. Chem. Phys.*, 1996, **104**, 6491.
(57) Y.-Y. Chuang and D. G. Truhlar, *J. Chem. Phys.*, 1997, **107**, 83.
(58) E. B. Wilson, Jr., J. C. Decius and P. C. Cross, *Molecular Vibrations*, Ed.; McGraw-Hill, New York, 1955.
(59) C.-L. Huang, C.-L. Liu, C.-K. Ni and J. T. Hougen, *J. Mol. Spectrosc.*, 2005, **233**, 122.
(60) V. Hanninen and L. Halonen, *J. Chem. Phys.*, 2007, **126**, 064309.
(61) G. Katzer and A. F. Sax, *Chem. Phys. Lett.*, 2003, **368**, 473.
(62) K. L. Clarkson, K. Mehlhorn and R. Seidel, *Lect. Notes Comput. Sci.*, 1992, **577**, 463.
(63) A program for convex hulls, http://www.netlib.org/voronoi/hull.html
(64) Y. Zhao and D. G. Truhlar, *Theor. Chem. Acc.* , 2008, **120**, 215.
(65) B. J. Lynch, P. L. Fast, M. Harris and D. G. Truhlar, *J. Phys. Chem. A*, 2000, **104**, 4811.
(66) R. Krishnan, J. S. Binkley, R. Seeger and J. A. Pople, *J. Chem. Phys.*, 1980, **72**, 650.

(67) T. Clark, J. Chandrasekhar, G. W. Spitznagel and P. v. R. Schleyer, *J. Comput. Chem.*, 1983, **4**, 294.
(68) M. J. Frisch, G. W. Trucks, H. B. Schlegel, G. E. Scuseria, M. A. Robb, J. R. Cheeseman, G. Scalmani, V. Barone, B. Mennucci, G. A. Petersson, H. Nakatsuji, M. Caricato, X. Li, H. P. Hratchian, A. F. Izmaylov, J. Bloino, G. Zheng, J. L. Sonnenberg, M. Hada, M. Ehara, K. Toyota, R. Fukuda, J. Hasegawa, M. Ishida, T. Nakajima, Y. Honda, O. Kitao, H. Nakai, T. Vreven, J. A. Montgomery, Jr., J. E. Peralta, F. Ogliaro, M. Bearpark, J. J. Heyd, E. Brothers, K. N. Kudin, V. N. Staroverov, R. Kobayashi, J. Normand, K. Raghavachari, A. Rendell, J. C. Burant, S. S. Iyengar, J. Tomasi, M. Cossi, N. Rega, N. J. Millam, M. Klene, J. E. Knox, J. B. Cross, V. Bakken, C. Adamo, J. Jaramillo, R. E. Gomperts, O. Stratmann, A. J. Yazyev, R. Austin, C. Cammi, J. W. Pomelli, R. Ochterski, R. L. Martin, K. Morokuma, V. G. Zakrzewski, G. A. Voth, P. Salvador, J. J. Dannenberg, S. Dapprich, A. D. Daniels, O. Farkas, J. B. Foresman, J. V. Ortiz, J. Cioslowski and D. J. Fox, *Gaussian 09*, Gaussian Inc., Wallingford CT, Revision A.02, 2009.
(69) I. M. Alecu, J. Zheng, Y. Zhao and D. G. Truhlar, *J. Chem. Theory Comput.*, 2010, **6**, 2872.
(70) S. W. Benson, F. R. Cruickshank, D. M. Golden, G. R. Haugen, H. E. O'Neal, A. S. Rodgers, R. Shaw and R. Walsh, *Chem. Rev.*, 1969, **69**, 279.
(71) J. Koput, S. Carter and N. C. Handy, *J. Phys. Chem. A*, 1998, **102**, 6325.
(72) K. Ohno, H. Yoshida, H. Watanabe, T. Fujita and H. Matsuura, *J. Phys. Chem.*, 1994, **98**, 6924.
(73) J. Moc, J. M. Simmie and H. J. Curran, *J. Mol. Struct.*, 2009, **928**, 149.
(74) L. V. Gurvich, I. V. Veyts and C. B. Alcock, *Thermodynamic Properties of Individual Substances*, 4th, Ed.; Hemisphere Pub. Co., New York, 1989.
(75) J. F. Counsell, J. L. Hales and J. F. Martin, *Trans. Faraday Soc.*, 1965, **61**, 1869.
(76) E. Hirota, *J. Chem. Phys.*, 1958, **28**, 839.
(77) R. M. Lees, *J. Chem. Phys.*, 1973, **59**, 2690.
(78) R. Meyer, *J. Mol. Spectrosc.*, 1979, **76**, 266.
(79) G. A. Guirgis, J. B. A. Barton and J. R. Durig, *J. Chem. Phys.*, 1983, **79**, 5918.
(80) J. A. Kunc, *Mol. Phys.*, 2003, **101**, 413.
(81) C. Y. Lin, E. I. Izgorodina and M. L. Coote, *J. Phys. Chem. A*, 2008, **112**, 1956.
(82) K. S. Pitzer, *Chem. Rev.*, 1940, **27**, 39.
(83) K. S. Pitzer and J. E. Kilpatrick, *Chem. Rev.*, 1946, **39**, 435.
(84) J. F. Messerly, G.B. Guthrie, S.S. Todd and H.L. Finke *J. Chem. Eng. Data*, 1967, **12,** 338.
(85) J. F. Messerly, S.S. Todd and H.L. Finke, *J. Phys. Chem.*, 1965, **69**, 353.
(86) H. L. Finke, J.F. Messerly and S.S. Todd, *J. Phys. Chem.*, 1965, **69**, 2094.
(87) J. F. Messerly, S.S. Todd and H.L. Finke, *J. Phys. Chem.*, 1965, **69**, 4304.
(88) D. W. Scott, In *Chemical Thermodynamic Properties of Hydrocarbons and Related Substances. Properties of the Alkane Hydrocarbons, C1 through C10 in the Ideal Gas State from 0 to 1500 K*, U.S. Bureau of Mines, Bulletin 666, 1974.
(89) J. B. Greenshields and F. D. Rossini, *J. Phys. Chem.*, 1958, **62**, 271.
(90) G. B. Guthrie Jr. and H.M. Huffman, *J. Am. Chem. Soc.*, 1943, **65**, 1139.

(91) D. R. Douslin and H. M. Huffman, *J. Am. Chem. Soc.*, 1946, **68**, 1704.

(92) H. M. Huffman, M.E. Gross, D.W. Scott and J. P. McCullough, *J. Phys. Chem.*, 1961, **65**, 495.

(93) D. W. Scott, G. Waddington, J. C. Smith and H. M. Huffman, *J. Chem. Phys.*, 1947, **15**, 565.

(94) S. W. Benson, In *Thermochemical Kinetics*, Wiley-Interscience, New York, 2nd, Ed.; 1976.

(95) N. Cohen and S. W. Benson, *Chem. Rev.*, 1993**, 93**, 2419.

(96) S. W. Benson and J. H. Buss, *J. Chem. Phys.*, 1958**, 29**, 546.

(97) J. Zheng, T. Yu, E. Papajak, I. M. Alecu, S. L. Mielke and D. G. Truhlar, *Phys. Chem. Chem. Phys.*, 2011, **13**, 10885.

(98) T. Yu, J. Zheng and D. G. Truhlar, *Chem. Sci.*, 2011, **14**, 482.

(99) J. Zheng, T. Yu, and D. G. Truhlar, *Phys. Chem. Chem. Phys*, 2011, **13**, 19318.

(100) B. M. Wong and S. Raman, *J. Comp. Chem.*, 2006, **28**, 759.

(101) B. M. Wong M. M. Fadri and S. Raman, *J. Comp. Chem.*, 2007, **29**, 481.

(102) D. P. Tew, N. C. Handy, S. Carter, S. Irle and J. M. Bowman, *Mol. Phys*. 2003, **101**, 3513.

(103) API Tables: *Selected Values of Properties of Hydrocarbons and Related Compounds, American Petroleum Institute Research Project 44*, Carnegie Press (Carnegie Institute of Technology), Pittsburgh, PA, 1953.

(104) TRC Data Series: M. Frenkel, G. J. Kabo, K. N. Marsh, G. N. Roganov and R. C. Wilhoit, *Thermodynamics of Organic Compounds in the Gas State*, Vol. II, CRC Press, Boca Raton, FL, 1994.

(105) D. G. Truhlar and A. D. Isaacson, *J. Chem. Phys*., 1991, **94**, 357.

(106) B. C. Garrett and D. G. Truhlar, *J. Phys. Chem*., 1979, **83**, 1915.

(107) A. D. Isaacson, D. G. Truhlar, K. Scanlon and J. Overend, *J. Chem. Phys*., 1981, **75**, 3017.

(108) M. J. Frisch, J. A. Pople and J. S. Binkley, *J. Chem. Phys.*, 1984, **80**, 3265.

(109) B. J. Lynch, Y. Zhao and D. G. Truhlar, *J. Phys. Chem*. A, 2003, **107**, 1384.

(110) B. J. Lynch, Y. Zhao and D. G. Truhlar, *J. Phys. Chem. A*, 2005, **109**, 1643.

(111) T. B. Adler, G. Knizia and H.-J. Werner, *J. Chem. Phys*., 2007, **127**, 221106.

(112) G. Knizia, T. B. Adler and H.-J. Werner, *J. Chem. Phys*., 2009, **130**, 054104.

(113) (a) E. Papajak and D. G. Truhlar, *J. Chem. Theor. Comput.*, 2011, *7*, 10; (b) E. Papajak and D. G. Truhlar, *J. Chem. Theor. Comput.*, 2010, **6**, 597.

(114) Y. Zhao, and D. G. Truhlar, *MLGAUSS* computer program, version 2.0, University of Minnesota, Minneapolis, 2007.

(115) H.-J. Werner, P. J. Knowles, F. R. Manby, M. Schütz, P. Celani, G. Knizia, T. Korona, R. Lindh, A. Mitrushenkov, G. Rauhut, T. B. Adler, R. D. Amos, A. Bernhardsson, A. Berning, D. L. Cooper, M. J. O. Deegan, A. J. Dobbyn, F. Eckert, E. Goll, C. Hampel, A. Hesselmann, G. Hetzer, T. Hrenar, G. Jansen, C.

Köppl, Y. Liu, A. W. Lloyd, R. A. Mata, A. J. May, S. J. McNicholas, W. Meyer, M. E. Mura, A. Nicklaß, P. Palmieri, K. Pflüger, R. Pitzer, M. Reiher, T. Shiozaki, H. Stoll, A. J. Stone, R. Tarroni, T. Thorsteinsson, M. Wang, A. Wolf. . *Molpro*, University of Birmingham, Birmingham, 2010.1, 2010.

(116) J. Zheng, S. L. Mielke, K. L. Clarkson and D. G. Truhlar, *MSTor* computer program, version 2011, University of Minnesota, Minneapolis, 2011.

(117) C. J. Hoeve, *J. Chem. Phys*., 1961, **35**, 1266.

(118) K. Naqai and T. Ishikawa, *J. Chem. Phys*., 1962, **37**, 496.

(119) R. D. Burkhart and J. C. Merrill, *J. Chem. Phys*., 1967, **46**, 4985.

(120) K. Nagai, *J. Chem. Phys*., 1968, **48**, 5646.

(121) T. Yasukawa and C. Chachaty, *Chem. Phys. Lett*., 1976, **43**, 565.

(122) B. Tevlin, S, Laffleur and L. E. H. Trainon, *Chem. Phys. Lett*., 1985, **122**, 581.

(123) S. Tsuzuki, L. Schlifer, H. Goto, E. D. Jemmis, H. Hosoya, K. Siam, K. Tanabe, and E. Osawa, *J. Am. Chem. Soc.*, 1991, **113**, 4665.

(124) H. Goto, E. Osawa and M. Yamato, *Tetrahedron*, 1993, **49**, 387.

(125) R. L. Dunbrack, Jr. and M. Karplus, *Nature Struct. Biol*., **1994**, 1, 334.

(126) R. Y. Dong, *Phys. Rev. E*, 1999, **60**, 5631.

(127) T. M. Madkoun and A. Soldera, *Eur. Polymer J*., 2001, **37**, 1105.

(128) J. B. Klauda, B. R. Brooks, A. D. Mackerell, Jr., R. M. Venable and R. W. Pastor, *J. Phys. Chem. B*, 2005, **109**, 5300.

(129) J. B. Klauda, R. W. Pastor and B. R. Brooks, *J. Phys. Chem. B*, 2005, **109**, 15684.

(130) W. L. Mattice, N. Waheed and F. Erguney, *Macromolecular Theory and Simulations*, 2006, **15**, 529.

(131) K. S. Pitzer, *J. Am. Chem. Soc.*, 1940, **62**, 1224.

(132) G. Waddington, S. S. Todd and H. M. Huffman, *J. Am. Chem. Soc*., 1947, **69**, 22.

(133) W. B. Person and G. C. Pimentel, *J. Am. Chem. Soc.*, 1953, **75**, 532.

(134) G. S. Parks, H. M. Huffman, and S. B. Thomas, *J. Am. Chem. Soc.*, 1930, **52**, 1032.

(135) N. Yamauchi, A. Miyoshi, K. Kosaka, M. Koshi and H. Matsui, *J. Phys. Chem. A*, 1999, **103**, 2723.

(136) A. Miyoshi, J. Widjaja, N. Yamauchi, M. Koshi and H. Matsui, *Proc. Combust. Inst.*, 2002, **29**, 1285.

(137) W. Tsang, J. A. Walker and J. A. Manion, *Proc. Combust. Inst*., 2007, **31**, 141.

(138) J. Zheng and D. G. Truhlar, *J. Phys. Chem. A*, 2009, **113**, 11919.

(139) D. G. Truhlar and A. Kuppermann, *J. Am. Chem. Soc*., 1971, **93**, 1840.

(140) (a) H. Eyring, *Chem. Rev.*, 1935, **17**, 65; (b)D. G. Truhlar, B. C. Garrett and S. J. Klippenstein, *J. Phys. Chem.*, 1996, **100**, (31), 12771.

(141) D. G. Truhlar and B. C. Garrett, *Annu. Rev. Phys. Chem*., 1984, **85**, 159.

(142) K. K. Baldridge, M. S. Gordon, R. Steckler and D. G. Truhlar, *J. Phys. Chem.* 1989, **93**, 5107.

(143) D. G. Truhlar, In *The Reaction Path in Chemistry: Current Approaches and Perspectives*,ed. D. Heidrich, Kluwer, Dordrecht, 1995, pp. 229.
(144) Y. Kim, J. C. Corchado, J. Villa, J. Xing and D. G. Truhlar, *J. Chem. Phys.*, 2000, **112**, 2718.
(145) O. Tishchenko and D. G. Truhlar, *J. Chem. Theor. Comput.*, 2009, **5**, 1454.
(146) Y. Zhao and D. G. Truhlar, *Theor. Chem. Acc*., 2008, **119**, 525.
(147) Y.-P. Liu, G. C Lynch, T. N. Truong, D.-h. Lu, D. G. Truhlar and B. C. Garrett, *J. Am. Chem. Soc*., 1993, **115**, 2408.
(148) A. Fernandez-Ramos, B. A. Ellingson, B. C. Garrett and D. G. Truhlar, *Rev. Comput. Chem.*, 2007, **23**, 125.
(149) J. Zheng, S. Zhang, B. J. Lynch, J. C. Corchado, Y. -Y. Chuang, P. L. Fast, W. -P. Hu, Y. -P. Liu, G. C. Lynch, K. A. Nguyen, C. F. Jackels, A. F. Ramos, B. A. Ellingson, V. S. Melissas, J. Villà, I. Rossi, E. L. Coitiño, J. Pu, T. V. Albu and D. G. Truhlar, POLYRATE-version 2010-A, University of Minnesota, Minneapolis, 2010.
(150) D. G. Truhlar and B. C. Garrett, *Acc. Chem. Res*., 1980, **13**, 440.
(151) D. G. Truhlar, A. D. Isaacson, R. T. Skodje and B. C. Garrett, *J. Phys. Chem*., 1982, **86**, 2252.
(152) S. N. Rai and D. G. Truhlar, *J. Chem. Phys*., 1983, **79**, 6046.
(153) Y. Georgievskii and S. J. Klippenstein, *J. Phys. Chem. A*, 2003, **107**, 9776.
(154) J. Zheng, S. Zhang and D. G. Truhlar, *J. Phys. Chem. A*, 2008, **112**, 11509.
(155) J. G. Lauderdale and D. G. Truhlar, *Surf. Sci*., 1985, **164**, 558.
(156) S. E. Wonchoba and D. G. Truhlar, *Phys. Rev. B*, 1996, **53**, 11222.
(157) Y.-Y. Chuang, C. J. Cramer and D. G. Truhlar, *Int. J. Quant. Chem*., 1998, **70**, 887.
(158) Y. Kim, J. R. Mohrig and D. G. Truhlar, *J. Am. Chem. Soc*., 2010, **131**, 11071.
(159) C. Alhambra, J. Corchado, M. L. Sánchez, M. Garcia-Viloca, J. Gao and D. G. Truhlar, *J. Phys. Chem. B*, 2001, **105**, 11326.
(160) D. G. Truhlar, J. Gao, M. Garcia-Viloca, C. Alhambra, J. M. Corchado, L. Sanchez and T. D. Poulsen, *Int. J. Quan. Chem*., 2004, **100**, 1136.
(161) D. G. Truhlar, In *Isotope Effects in Chemistry and Biology*, ed. A. Kohen and H. H. Limbach, Marcel Dekker Inc., New York, 2006; pp. 579-620.
(162) D. G. Truhlar and B. C. Garrett, In *Hydrogen Transfer Reactions*. ed. J. T. Hynes, J. P. Klinman, H. H. Limbac, and R. L. Schowen, Wiley-VCH, Weinheim, Germany, 2007, Vol. 2, pp 833-874.
(163) B. C. Garrett and D. G. Truhlar, *J. Phys. Chem.*, 1979, **83**, 1079; Errata: 1980, **84**, 682; 1983, **87**, 4553.
(164) A. D. Isaacson and D. G. Truhlar, *J. Chem. Phys.*, 1982, **76**, 1380.
(165) B. C. Garrett, D. G. Truhlar, R. S. Grev and A. W. Magnuson, *J. Phys. Chem*., 1980, **84**, 1730; Erratum: 1983, **87**, 4554.
(166) D. G. Truhlar, A. D. Isaacson and B. C. Garrett, In *Theory of Chemical Reaction Dynamics*, ed. M. Baer, CRC Press, Boca Raton, FL, 1985, Vol. 4, pp. 65-137.
(167) D. C. Chatfield, R. S. Friedman, D. G. Truhlar, B. C. Garrett and D. W. Schwenke, *J. Am. Chem. Soc*., 1991, **113**, 486.

(168) D. C. Chatfield, R. S. Friedman, D. G. Truhlar, B. C. Garrett and D. W. Schwenke, *Faraday. Dis. Chem. Soc*., 1991, **91**, 289.
(169) A. Fernández-Ramos, B. A. Ellingson, R. Meana-Pañeda, J. M. C. Marques and D. G. Truhlar, *Theor. Chem. Acc*., 2007, **118**, 813.
(170) D. G. Truhlar, *J. Mol. Spec*., 1971, **38**, 415.
(171) B. C. Garrett and D. G. Truhlar, *J. Phys. Chem.*, 1979, **83**, 1915.
(172) Y. Zhao and D. G. Truhlar, *J. Chem. Theor. Comput*., 2008, **4,** 1849.
(173) Y. Zhao, B. J. Lynch and D. G. Truhlar, *Phys. Chem. Chem. Phys.*, 2005, **7**, 43.
(174) E. Papajak, H. R. Leverentz, J. Zheng and D. G. Truhlar, *J. Chem. Theor. Comput.*, 2009, **5**, 1197.
(175) (a) T. H. Dunning, *J. Chem. Phys*. 1989, *90*, 1007; (b) R. A. Kendall, T.H. Dunning and R. J. Harrison, *J. Chem. Phys*., 1992, **96**, 6796.
(176) F. Weigend and R. Ahlrichs, *Phys. Chem. Chem*. *Phys*., 2005, **7**, 3297.
(177) (a) Gaussian 03, Revision E.01, J. Frisch, G. W. Trucks, H. B. Schlegel, G. E. Scuseria, M. A. Robb, J. R. Cheeseman, G. Scalmani, V. Barone, B. Mennucci, G. A. Petersson, H. Nakatsuji, M. Caricato, X. Li, H. P. Hratchian, A. F. Izmaylov, J. Bloino, G. Zheng, J. L. Sonnenberg, M. Hada, M. Ehara, K. Toyota, R. Fukuda, J. Hasegawa, M. Ishida, T. Nakajima, Y. Honda, O. Kitao, H. Nakai, T. Vreven, Jr., J. A. Montgomery, J. E. Peralta, F. Ogliaro, M. Bearpark, J. J. Heyd, E. Brothers, K. N. Kudin, V. N. Staroverov, R. Kobayashi, J. Normand, K. Raghavachari, A. Rendell, J. C. Burant, S. S. Iyengar, J. Tomasi, M. Cossi, N. Rega, N. J. Millam, M. Klene, J. E. Knox, J. B. Cross, V. Bakken, C. Adamo, J. Jaramillo, R. Gomperts, R. E. Stratmann, O. Yazyev, A. J. Austin, R. Cammi, C. Pomelli, J. W. Ochterski, R. L. Martin, K. Morokuma, V. G. Zakrzewski, G. A. Voth, P. Salvador, J. J. Dannenberg, S. Dapprich, A. D. Daniels, Ö. Farkas, J. B. Foresman, J. V. Ortiz, J. Cioslowski and D. J. Fox, Gaussian, Inc., Wallingford CT, 2003.(b) Y. Zhao and D. G. Truhlar, *MN-GFM: Minnesota Gaussian Functional Module*, version 4.1; University of Minnesota, Minneapolis, MN, 2008.
(178) T. V. Albu, J. C. Corchado and D. G. Truhlar, *J. Phys. Chem. A*, 2001, **105**, 8465.
(179) H. Lin, J. Z. Pu, T. V. Albu and D. G. Truhlar, *J. Phys. Chem. A*, 2004, **108**, 4112.
(180) K. H. Kim and Y. Kim, *J. Chem. Phys*., 2004, **120**, 623.
(181) H. Lin, Y. Zhao, O. Tishchenko and D. G. Truhlar, *J. Chem. Theory Comput*., 2006, **2**, 1237.
(182) O. Tishchenko and D. G. Truhlar, *J. Phys. Chem. A*, 2006, **110**, 13530.
(183) O. Tishchenko, M. Higashi, T. V. Albu, J. C. Corchado, Y. Kim, J. Villà, J. Xing, H. Lin and D. G. Truhlar, MCSI computer program, version 2010, University of Minnesota, Minneapolis, 2010.
(184) T. V. Albu, O. Tishchenko, J. C. Corchado, Y. Kim, Villà, J. Xing, H. Lin, M. Higashi and D. G. Truhlar, MC-TINKERATE computer program, version 2010, University of Minnesota, Minneapolis, 2010.
(185) R. Valero, L. Song, J. Gao and D. G. Truhlar, *J. Chem. Theor. Comp*., 2009, **5**, 1.
(186) N. L. Allinger, Y. H. Yuh and J. H. Lii, *J. Am. Chem. Soc*., 1989, **111**, 8551.
(187) J. H. Lii and N. L. Allinger, *J. Am. Chem. Soc*., 1989, **111**, 8566.
(188) J. H. Lii and N. L. Allinger, *J. Am. Chem. Soc*., 1989, **111**, 8576.

(189) J. M. Hornback, In *Organic Chemistry*, ed., Brooks/Cole, Pacific Grove, CA, 2nd edn., 2005, p. 91.
(190) D.-h. Lu, T. N. Truong, V. S. Melissas, G. C. Lynch, Y.-P. Liu, B. C. Garrett, R. Steckler, A. D. Isaacson, S. N. Rai, G. C. Hancock, J. G. Lauderdale, T. Joseph and D. G. Truhlar, *Comp. Phys. Comm.*, 1992, **71**, 235.
(191) S. Sharma, S. Raman and W. H. Green, *J. Phys. Chem. A*, 2010, **114**, 5689.
(192) J. C. Corchado, E. L. Coitino, Y. Y. Chuang, P. L. Fast and D. G. Truhlar, *J. Phys. Chem. A*, 1998, **102**, 2424.
(193) J. Zheng and D. G. Truhlar, *Phys. Chem. Chem. Phys*., 2010, **12**, 7782.
(194) M. Garcia-Viloca, J. Gao, M. Karplus and D. G. Truhlar, *Science* 2004, **303**, 186.
(195) D. G. Truhlar and M. S. Gordon, *Science* 1990, **249**, 491.
(196) D. G. Truhlar, F. B. Brown, R. Steckler and A. D. Isaacson, In *The Theory of Chemical Reaction Dynamics*, Clary, D. C. Ed.; Reidel, D. Dordrecht: Holland, 1986; pp. 285-329.